



**UNIVERSITÀ DEGLI STUDI DI NAPOLI
“FEDERICO II”**

SCUOLA POLITECNICA E DELLE SCIENZE DI BASE
DIPARTIMENTO DI INGEGNERIA INDUSTRIALE

PHD THESIS IN
INDUSTRIAL ENGINEERING

**EFFECTS OF THE SECONDARY ITERATIONS OF
SQUARE FRACTAL GRIDS
ON CONTINUOUS AND SYNTHETIC JETS**

CANDIDATE:
GIUSY CASTRILLO

COORDINATOR:
Prof. Michele Grassi

TUTORS:
**Prof. Tommaso Astarita
Dr. Gioacchino Cafiero**

December 2017

*Don't give up...
... but, please,
don't forget to be happy!*

CONTENTS

SUMMARY	1
1. INTRODUCTION	3
1.1. FRACTAL-GENERATED TURBULENCE	4
1.2. FRACTAL-GENERATED TURBULENCE APPLICATIONS	14
1.3. OBJECTIVES	20
1.4. OUTLINE	21
2. MEASUREMENT TECHNIQUES	23
2.1. FUNDAMENTALS OF PARTICLE IMAGE VELOCIMETRY	23
2.1.1. EXPERIMENTAL DETAILS	25
2.2. INFRARED THERMOGRAPHY	27
2.2.1. THEORETICAL BACKGROUND	27
2.2.2. IR SCANNING RADIOMETERS	31
2.2.3. IR SCANNER RADIOMETRIC CALIBRATION	33
2.2.4. THE HEATED THIN FOIL HEAT FLUX SENSOR	35
3. EXPERIMENTAL SETUP DETAILS	39
3.1. GRIDS DESCRIPTION	39
3.2. THE CONTINUOUS JET EXPERIMENTS	40
3.2.1. TURBULENT CONTINUOUS JETS	40
3.2.2. THE CONTINUOUS JET EXPERIMENTAL RIGS	43
3.3. THE SYNTHETIC JET EXPERIMENTS	49
3.3.1. SYNTHETIC JETS	49
3.3.2. THE SYNTHETIC JET EXPERIMENTAL APPARATUS	53

4. THE EFFECTS OF THE SECONDARY ITERATIONS BARS ON CONTINUOUS TURBULENT JETS	57
4.1. MAIN FLOW FEATURES	57
4.2. ANALYSES OF THE BARS' WAKES BY MEANS OF THE SNAPSHOT POD	68
4.3. MAIN CONCLUSIONS	70
5. THE EFFECTS OF THE SECONDARY ITERATIONS BARS ON SYNTHETIC TURBULENT JETS	73
5.1. INTRODUCTION	73
5.2. TIME-AVERAGED FLOW FIELDS	74
5.3. PHASE-AVERAGED FLOW FIELDS	82
5.4. MAIN CONCLUSIONS	95
6. EFFECT OF THE GRID GEOMETRY ON THE CONVECTIVE HEAT TRANSFER OF IMPINGING JETS	97
6.1. INTRODUCTION	97
6.2. HEAT TRANSFER SPATIAL DISTRIBUTION: MAIN FEATURES	98
6.3. AREA AVERAGED NUSSELT NUMBER PROFILES AND UNIFORMITY OF THE CONVECTIVE HEAT TRANSFER RATE	99
6.4. MAIN CONCLUSIONS	104
7. EFFECT OF THE GRID GEOMETRY ON THE CONTINUOUS JET FLOW FIELD	105
7.1. MEAN FLOW FEATURES	105
7.2. LARGE SCALE ISOTROPY	110
7.3. VELOCITY SPECTRA	114
7.4. MAIN CONCLUSIONS	121

CONCLUSIONS AND FUTURE PERSPECTIVES	123
NOMENCLATURE	127
REFERENCES	135
LIST OF PUBLICATIONS	145
ACKNOWLEDGEMENTS	147

SUMMARY

The Nile river, the Italian coastline, the snowflakes, the tree branches, mountains, clouds, seashells all belong to a class of objects known as *fractals*. Fractals are never-ending patterns, widely diffused in nature, which repeat themselves over and over, at different length scales. Abstract fractals can be also generated by a computer calculating a simple equation over and over. Fractals have more and more applications in science modelling, as they very often describe the real world better than traditional mathematics and physics. Moreover, fractal-shaped elements have been successfully applied to many industrial fields such as the mixing, aeronautical, automotive, power generation and wind energy industries. Among the other, Cafiero et al. [1, 2, 3, 4] proposed the use of fractal grids to increase the mixing and heat transfer features of turbulent jets, typically used for cooling of turbine blades and of electronic components, for paper and film drying, for glass annealing and tempering, etc. Their results showed that fractal turbulators significantly increase the heat transfer properties of round turbulent jets or jet equipped with regular grids having the same blockage ratio of the fractal ones [1]. Subsequent 2D and 3D flow fields measurements [2, 3] showed that the main factors which are responsible for this increase are the higher turbulence intensity levels due to the fractal pattern and the ability of the fractal turbulator in producing streamwise vorticity.

Following these works, this thesis focuses on the effects of the secondary iterations bars on turbulent jets equipped with square-fractal inserts. The obtained results are organised in four different chapters.

In Chapter 4, the effects due to the introduction of the secondary iterations on continuous turbulent jets equipped with square-fractal inserts are analysed by introducing either a single square grid or a 3-iterations square-fractal grid at the exit section of short pipe nozzle. Measurements are carried out at fixed Reynolds number, $Re \approx 6,700$, by means of planar Particle Image Velocimetry. A double-camera configuration is used to simultaneously analyse the effects of the grids' bars and the interaction between the grid-generated turbulence and the jet shear layer. The flow fields are investigated both in terms of first and second order statistics. In order to assess the effects of the smallest bars of the fractal insert on the wake generated by the largest bars, the Proper Orthogonal Decomposition snapshot method is applied to a small measurement volume past the 1st iteration bars.

In Chapter 5, the same single square grid and fractal square grid analysed in Chapter 4 are inserted at the exit section of a synthetic jet device. Measurements are carried out, for three different device actuation frequencies, at a fixed Reynolds

number $Re \approx 6,700$. The results are investigated both in terms of time-averaged and phase-averaged flow fields. The generation and the evolution of the coherent vortical structures are analysed by means of the Q-criterion.

The effects of the secondary iterations introduction and of their thickness in turbulent continuous jets equipped with fractal-square grids are discussed both in terms of heat transfer properties (Chapter 6) and flow field measurements (Chapter 7). In particular, in Chapter 6, IR Thermography measurements, combined with the heated-thin-foil heat flux sensor, are performed to compare, under the same power input, several fractal and single square grids in terms of both spatial averaged and local convective heat transfer. Moreover, the effect of the grid geometry onto the convective heat transfer uniformity is investigated.

Finally, the jet flow developed downstream of each grid analysed in Chapter 6 is investigated, at a fixed Reynolds number $Re \approx 16,000$. The jet flow due to the introduction of a regular grid characterised by the same blockage ratio of the fractal one is also investigated. Finally, the axisymmetric turbulent jet evaluated at the same Reynolds number is reported as reference. Results are analysed both in terms of first and second order statistics. Moreover, the effects of the grid geometry on the large-scale isotropy and on the spatial-averaged velocity power spectra are discussed.

1. INTRODUCTION

Fractals are *never-ending* patterns that iteratively repeat themselves at different scales: which contain themselves in themselves. The word *fractal*, coming from the Latin verb *frangere*, means “to break”, to create irregular fragments. They can be simply created by repeating a geometric pattern, as, for example, the *Sierpinski’s Triangle* pattern (Fig. 1.1-a), described by the Polish mathematician Waclaw Sierpinsky in 1916 [5] but already appeared in Italian art from the 13th century, or by calculating a simple equation over and over (as the *Mandelbrot Set* [6] depicted in Fig. 1.1-b). However, they are not just complex and pretty pictures generated by computers: fractal objects and patterns are found all over nature, spanning a huge range of scales, from the tiny branching of our blood vessels to the branching of trees and river networks (Fig. 1.1-c-e).

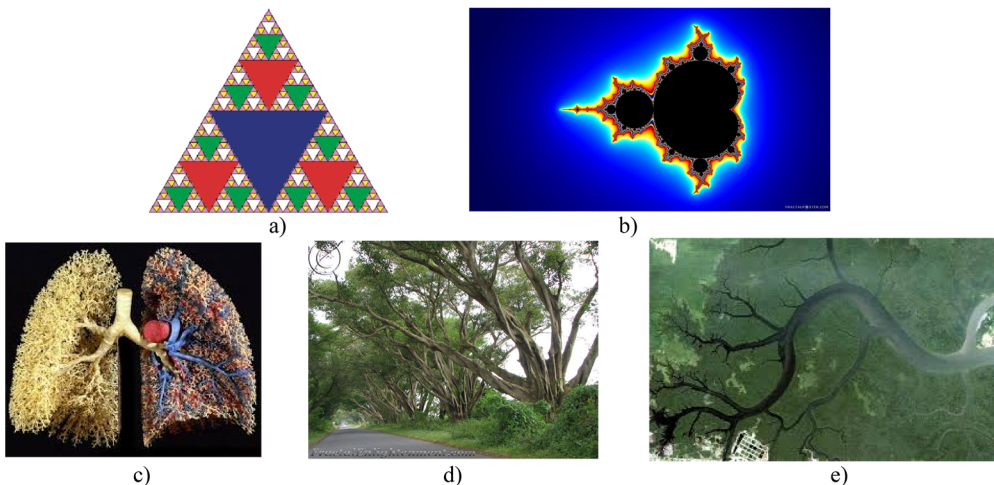


Fig. 1.1 - a) Sketch of a Sierpinski triangle; b) representation of a Mandelbrot fractal; c) branching of human blood vessels; d) tree branches; e) fractal shape of a river network.

Referring to one of the fathers of the fractal geometry, the mathematician Benoit Mandelbrot, Professor Freeman Dyson wrote [7]:

“Now, as Mandelbrot points out [...] Nature has played a joke on the mathematicians. The 19th-century mathematicians may have been lacking in imagination, but Nature was not. The same pathological structures that the mathematicians invented to break loose from 19th-century naturalism turn out to be inherent in familiar objects all around us. We do not have to look far to find them.”

1.1. FRACTAL-GENERATED TURBULENCE

Fractals have more and more applications in science, as they very often describe the real world better than traditional mathematics and physics. They are used to model soil erosion [8, 9] or to analyse seismic patterns [10] or to describe the roughness of surfaces [11]. Moreover, fractal image compression techniques [12] are typically adopted in computer science or fractal-shaped antennas [13], that greatly reduce the size and weight of common ones, are used. Finally, fractal based theories have been developed to better describe and understand several complex fluid mechanics problems, such as flows in porous media [14], flames [15, 16, 17] and turbulent flows [18, 19, 20]. Dates to the 1920s the model proposed by Richardson [18] (later consistently and mathematically described by Kolmogorov in 1941 [19, 20]) of a fractal nature of turbulence, characterised by cascades of eddies of different sizes, with energy transferred from larger to smaller scales and finally, at the smallest scales converted to internal energy (heat) by viscous dissipation.

1.1. FRACTAL-GENERATED TURBULENCE

Research activities on fractal-generated turbulence, i.e. turbulence produced by fractal objects, started about twenty years ago and they were first focused on 3D-fractal objects: Queiros-Conde and Vassilicos [21] and Staicu et al. [22] measured the turbulence statistics in the wake of fractal tree-like generators, pointing out how turbulence with much higher intensity and distributed over a wider range of length-scales can be generated by using fractal stirrers. In 2007, Hurst and Vassilicos [23] carried out a series of grid-turbulence experiments using as turbulence promoters a multi class of 21 planar-fractal grids; these grids were grouped in *cross*-, *I*- and *square*-fractal grids, depending on the geometry of the repeating pattern (see Fig. 1.2). Their main purposes were to understand how the turbulence decays when it is created by eddies of different sizes and how it scales when it is generated by fractal grids having its own intrinsic scaling; its final aim was the generation of homogeneous isotropic turbulence at high local Reynolds number. Their measurements, obtained by means of hot wire anemometry, showed unusual results related to the square-fractal grids.

Indeed, they found that this type of passive grids generates an elongated turbulence production region, in which the turbulence builds up reaching a peak at a streamwise location, x_{peak} , mainly dependent on the grid geometry. Beyond this point, the turbulence intensity rapidly decays, following an exponential law. Moreover, they demonstrated that square-fractal grids can generate significantly higher Re_{λ_u} of the streamwise velocity fluctuations ($Re_{\lambda_u} = u' \lambda_u / \nu$, where u' is the root mean square

(*r.m.s.*) of the streamwise velocity fluctuations evaluated along the centreline, λ_u is the longitudinal Taylor microscale and ν is the kinematic viscosity) than “classical” regular grids with equivalent blockage ratio and under similar conditions [24]. Perhaps even more interesting, they are capable to replicate comparable Re_{λ_u} with respect to active grids [25], whilst also retaining a good level of homogeneity and isotropy.

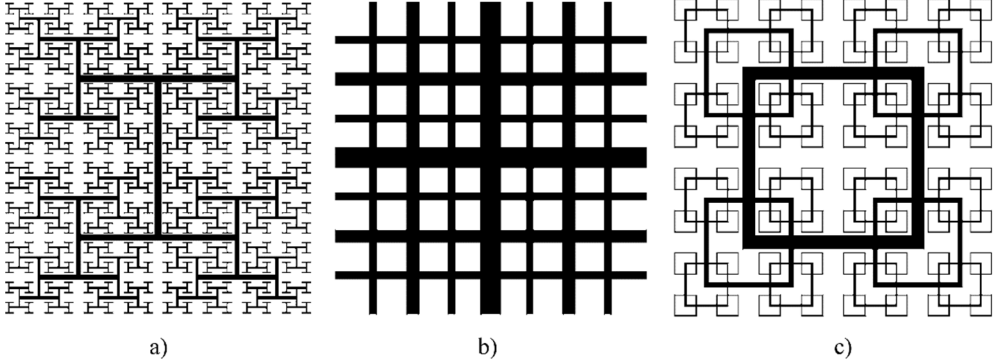


Fig. 1.2 - Example of a: a) I-fractal grid; b) cross-fractal grid; c) square-fractal grid (adapted from [23]).

The possibility to tune the turbulence peak by changing the grid geometry (i.e. the bar thickness and length, the number of iterations, etc ...) and to create high local Reynolds numbers and high-homogeneous turbulence, makes square-fractal grids very appealing for both industrial applications and research focused on turbulence modelling. For these reasons, most of the studies on fractal-generated turbulence, during the last decade, have been related to square-fractal grids.

A square-fractal grid (see Fig. 1.3) is completely defined by:

- the square pattern;
- the number of the fractal iterations N ;
- the length L_0 and the thickness t_0 of the 1st iteration bars (i.e. the biggest ones);
- the ratios $R_L = L_j/L_{j-1}$ and $R_t = t_j/t_{j-1}$ between the length and the thickness of subsequent bars.

Therefore, at each iteration, the grid’s bar length and thickness can be evaluated as:

$$L_j = R_L^j L_0 \quad (1.1)$$

$$t_j = R_t^j t_0 \quad (1.2)$$

1.1. FRACTAL-GENERATED TURBULENCE

with $j=0, \dots, N-1$.

In [23], the authors also calculated the grid's blockage ratio σ and introduced the effective meshlength M_{eff} as:

$$\sigma = \frac{A}{T_t} = \frac{L_0 t_0 \sum_{j=0}^{N-1} 4^{j+1} R_L^j R_t^j - t_0^2 \sum_{j=1}^{N-1} 2^{2j+1} R_t^{2j-1}}{T_t} \quad (1.3)$$

$$M_{eff} = \frac{4T_t}{P} \sqrt{1 - \sigma} \quad (1.4)$$

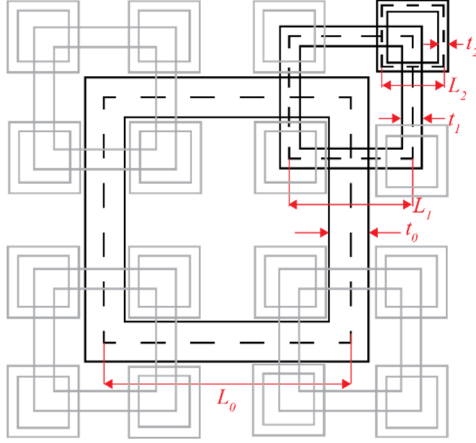


Fig. 1.3 - Square-fractal geometry.

where A represents the area covered by the grid, T_t is the tunnel's square cross section, and P is the fractal perimeter length of the grid.

Results reported in [23] have shown that while the turbulence exponentially decays, the longitudinal Taylor microscale λ_u and the longitudinal and lateral integral length-scales, L_u and L_v , remain approximately constant with the longitudinal distance x . As reported in literature [26]: “A turbulence with kinetic energy that decays exponentially whilst its integral length scales remain constant is either nonisotropic and/or nonhomogeneous or, if it is homogeneous and isotropic, is such that the kinetic energy dissipation rate per unit mass, ε , is not equal to:

$$\varepsilon = \varepsilon_{iso} = \frac{C_{\varepsilon_{iso}} u'^3}{L_u} \quad (1.5)$$

where $C_{\varepsilon_{iso}}$ is a universal constant.” Therefore, Seoud and Vassilicos [26] focused their attention on the turbulence decay region and experimentally demonstrated the small-scales isotropy and homogeneity, at least in the region surrounding the centreline and for $x \geq 2x_{peak}$.

This unusual behaviour confirms that the Richardson-Kolmogorov cascade, assumed as a cornerstone in turbulence theories and models, is not universally valid for all the boundary-free turbulent shear flows [23]. This means $\varepsilon_{iso} \sim C_{\varepsilon_{iso}} u'^3 / L_u$ is also not universally valid, not even in homogeneous and isotropic turbulence as for the fractal-generated turbulence far downstream where it is decaying.

Mazellier and Vassilicos [27] confirmed that a protracted production region exists in the lee of space-filling square fractal grids, which extends over a distance dependent on the bars' thickness ratio t_r (i.e. the ratio between the thicknesses of the largest and smallest bars) and is followed by a region where the turbulence decays. They demonstrated that the x_{peak} location decreases as t_r increases while the axial fluctuations increase (see Fig. 1.4).

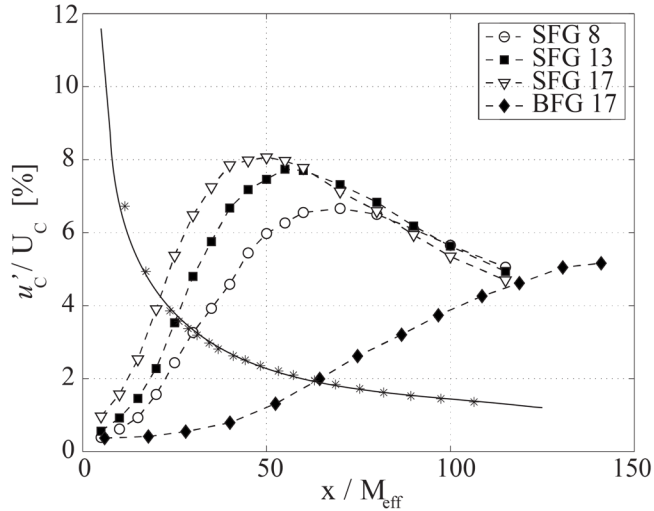


Fig. 1.4 - Streamwise velocity fluctuations of a regular grid (*) compared to three different 3-iterations square fractal grids (SFG 8/ $t_r=8$, SFG 13/ $t_r=13$ and SFG 17/ $t_r=17$) and a 4-iteration square fractal grid (BFG 17/ $t_r=17$). All the grids have about the same M_{eff} . (adapted from [27]).

Following Hurst and Vassilicos [23], who suggested that x_{peak} can be expressed as a function of only the geometrical parameters of the grid, they applied the Prandtl mixing theory to describe the grid's wake, expressing the half-width of the wake generated by the bar of thickness t_j , at a streamwise distance x , as $l \sim \sqrt{t_j x}$ (see Fig. 1.5-a)) and, assuming that this theory could also be used in first approximation when the bars are surrounded by other bars of different sizes, they defined the *wake-interaction length scale* $x_* = L_0^2 / t_0$.

1.1. FRACTAL-GENERATED TURBULENCE

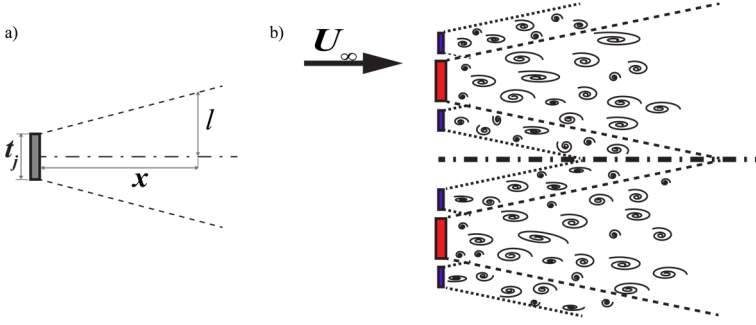


Fig. 1.5 - a) Schematic of the wake developed behind a single bar; b) wake interaction mechanism behind a fractal grid.

A schematic of the wake interaction mechanism behind fractal grids is reported in Fig. 1.5-b): x_* represents the furthestmost interaction between the wakes generated by the largest bars. The *wake-interaction length scale* x_* appeared to be an appropriate scaling for characterizing some features of the turbulent flows generated by space-filling square fractal grids: their experimental results showed that the longitudinal mean velocity gradient $\frac{\partial \bar{u}}{\partial x}$ becomes negligible for $x \geq 0.6x_*$ and the streamwise turbulence intensity peak x_{peak} is located at about $0.45x_*$. Moreover, in their experimental measurements, no correlation was found between x_{peak} and the mean flow velocity U_∞ . A more general expression for x_* , which takes into account the influence of eventual inlet free-stream velocity, has been proposed by Gomes-Fernandes et al. [28]. They obtained a new scaling capable of collapsing data from different initial conditions, different working fluids, various regular and square-fractal grids. Moreover, a comparison between square-fractal grids characterised by different iteration numbers and regular grids reported in [29] shows that the x_{peak} location depends on both N and σ such as an increase in N or σ may cause an increase or a decrease in x_{peak} , respectively:

$$x_{peak} = C(N, \sigma) \frac{L_0^2}{t_0} \quad (1.6)$$

Mazellier and Vassilicos [27] also showed a very irregular mean velocity profile close to the grid, especially downstream of the bars, where velocity deficits are clearly visible. In particular, they documented the interaction of jet-like and wake-like behaviours which, in turn, may be present depending on the location across the tunnel. In the regions surrounding these velocity defects, high mean flow gradients are present, with the turbulence intensity levels reaching local maxima. The authors showed that the turbulence peak location can vary widely across the grid plane and that a very elongated turbulence production region does not exist everywhere, due to

the inhomogeneous grid's blockage. Further downstream, both the mean velocity and the turbulence intensity profiles become smoother, supporting the view that the turbulence tends towards large-scale homogeneity.

Differently to what previously reported [23, 26], Mazellier and Vassilicos [27] showed that, in the decaying region, while Re_{λ_u} decreases, both the longitudinal integral scale and Taylor length scales slightly increase with the streamwise location x so that their ratio remains almost constant. The decoupling between L_u/λ_u and Re_{λ_u} has been explained in terms of a self-preserving single-length scale type of decaying homogeneous turbulence [30], with, however, L_u/λ_u slightly depending on the global Reynolds number $Re_{t_0} = U_\infty t_0/\nu$ (here defined with respect to t_0). Their results also showed that a decaying power-law could fit better the turbulence decay than the exponential law supposed in [23]. Later measurements by Valente and Vassilicos [31] showed that the exponent of the fitting power-law for fractal generated turbulence is almost twice the one for regular grids.

Valente and Vassilicos [32], summarising the previous results, suggested that, in the decay region of turbulence generated by square fractal grids, at high global Reynolds number Re_0 , the ratio between the integral length scale L_u and the Taylor microscale and the local Reynolds number Re_{λ_u} could be respectively expressed as:

$$\frac{L_u}{\lambda_u} \approx Re_0^\alpha A\left(\frac{x-x_0}{x_*}\right) \quad (1.7)$$

and

$$Re_{\lambda_u} \approx Re_0^\beta B\left(\frac{x-x_0}{x_*}\right) \quad (1.8)$$

being $A(x)$ an approximately constant function, $B(x)$ a steep power law and α and β positive real numbers.

Due to the sufficient level of global and local isotropy of the flow field [23, 28, 33], Valente and Vassilicos [32] assumed $\varepsilon = \varepsilon_{iso} = 15\nu u'^2/\lambda_u^2$ that, together with Eq. (1.5), leads to:

$$\frac{L_u}{\lambda_u} = \frac{C_{\varepsilon_{iso}}}{15} Re_{\lambda_u} \quad (1.9)$$

Equation (1.9) clearly points out that, in the turbulence decay region, as Re_{λ_u} is a decreasing function of x while L_u/λ_u remains almost constant, $C_{\varepsilon_{iso}}$ cannot be constant. The functional dependence of $C_{\varepsilon_{iso}}$ with the longitudinal coordinate x is, therefore, given by:

1.1. FRACTAL-GENERATED TURBULENCE

$$C_{\varepsilon_{iso}} = 15Re_0^{(\alpha-\beta)} A\left(\frac{x-x_0}{x_*}\right) / B\left(\frac{x-x_0}{x_*}\right) \quad (1.10)$$

which shows that $C_{\varepsilon_{iso}}$ increases as x and the global Reynolds number Re_0 increase. It is noteworthy to mention that the $C_{\varepsilon_{iso}}$ dependence on the two Reynolds number, Re_0 and Re_{λ_u} , expressed by (1.7) and (1.9) does not come from the Richardson-Kolmogorov phenomenology, which holds for $A = B = 1/2$. The results reported in [32] show that, at high enough values of Re_0 , $\alpha = \beta$ and $C_{\varepsilon_{iso}}(Re_0)$ for fractal-generated turbulence is comparable to that found for regular or active grids and, more generally, with other boundary-free turbulent flows. However, in fractal-generated turbulence, at high Re_0 , $C_{\varepsilon_{iso}}$ asymptote differs for different downstream locations, showing therefore a non-Richardson-Kolmogorov behaviour. This departure from ‘‘classical’’ turbulence development is due to the difference between $A\left(\frac{x-x_0}{x_*}\right)$ and $B\left(\frac{x-x_0}{x_*}\right)$. For fixed Re_0 and for $x > x_{peak}$, Re_{λ_u} rapidly decreases as moving downstream while L_u/λ_u remains approximately constant so that, as shown in Fig. 1.6, $C_{\varepsilon_{iso}} \sim Re_{\lambda_u}^{-1}$ appears to be a good approximation.

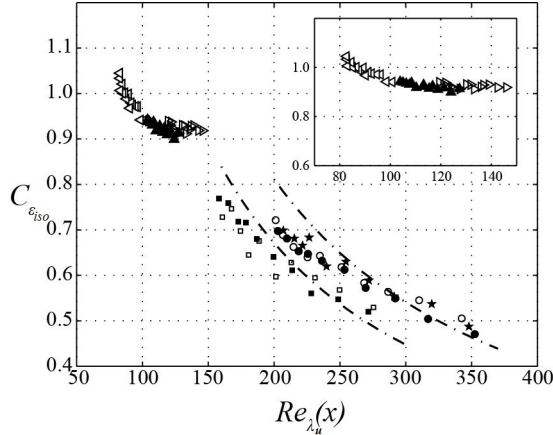


Fig. 1.6 - Normalised energy dissipation coefficient $C_{\varepsilon_{iso}}$ versus the local Reynolds number $Re_{\lambda_u}(x)$ for both regular and fractal grids, at different inlet velocity. (■)FSG, $U_{\infty} = 10\text{m/s}$, $l_w = 1\text{mm}$; (□)FSG, $U_{\infty} = 10\text{m/s}$, $l_w = 0.45\text{mm}$; (●)FSG, $U_{\infty} = 15\text{m/s}$, $l_w = 1\text{mm}$; (○)FSG, $U_{\infty} = 15\text{m/s}$, $l_w = 0.45\text{mm}$; (★)FSG, $U_{\infty} = 15\text{m/s}$, $l_w = 0.2\text{mm}$; (◁)RG, $U_{\infty} = 10\text{m/s}$, $l_w = 0.45\text{mm}$, (▲)RG, $U_{\infty} = 15\text{m/s}$, $l_w = 0.45\text{mm}$, (▶)RG, $U_{\infty} = 20\text{m/s}$, $l_w = 0.45\text{mm}$. The dashed-dot lines follow the form $\propto Re_{\lambda_u}^{-1}$ [32].

In subsequent studies [31, 34], Valente and Vassilicos showed the non-classical behaviour pointed out in studying fractal-generated turbulence was also manifested

in decaying turbulence originating from various regular grids, for sufficiently high global Reynolds numbers $Re_M = \frac{U_\infty M}{\nu}$ (where M is the side-length of the largest square of the grid). For fixed Re_M , the region of turbulence decay generated by classical regular grids could be divided in two sub-regions characterized by $C_{\varepsilon_{iso}} \sim Re_{L_u}^{-1}$ (where $Re_{L_u} = u' L_u / \nu$) and $C_{\varepsilon_{iso}} \approx const$, respectively. The separation point x_e between the two regions is determined by x_* (defined, in this case, as $x_* = M^2 / t_0$), i.e. by the grid's geometry.

Therefore, irrespective of the turbulence-generating grid and for high enough Re_M , as reported in Fig. 1.7, they found:

$$\varepsilon_{iso} \approx C_1 \frac{U_\infty u'^2 M}{L} \frac{M}{L} \quad (1.11)$$

and, equivalently:

$$\frac{L_u}{\lambda_u} \approx \sqrt{C_1 \frac{Re_M}{15}} \quad (1.12)$$

as acceptable approximations in the non-equilibrium decay region ($x_{peak} < x < x_e$), while, for $x > x_e$ the classical equilibrium dissipation scaling is recovered:

$$\varepsilon_{iso} \approx C_2 \frac{u'^3}{L_u} \approx C_{\varepsilon_{iso}} \frac{u'^3}{L_u} \quad (1.13)$$

with C_1 and C_2 being dimensionless constants only dependent on inlet or boundary conditions (type of fractal or regular grid, blockage ratio, etc.).

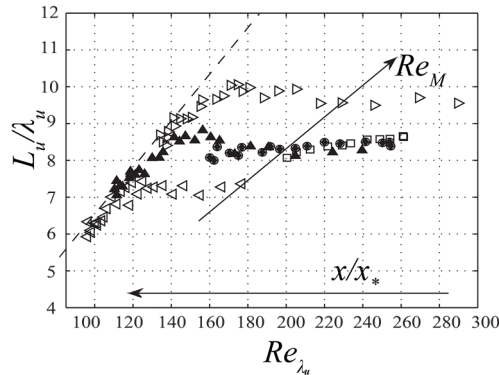


Fig. 1.7 - L_u/λ_u versus Re_{λ_u} of turbulent generated by several regular grids for fixed Re_M value (adapted from [34]).

Recently, numerical [35, 36, 37, 38] and experimental [39] works have been realised to assess the effects of the secondary iterations of square fractal grids.

1.1. FRACTAL-GENERATED TURBULENCE

Zhou et al. [36] showed that the turbulent flow generated past a single square grid presents similar characteristics with respect to the flow past a fractal square grid obtained by adding secondary iterations bars to the same central square frame (see Fig. 1.8).

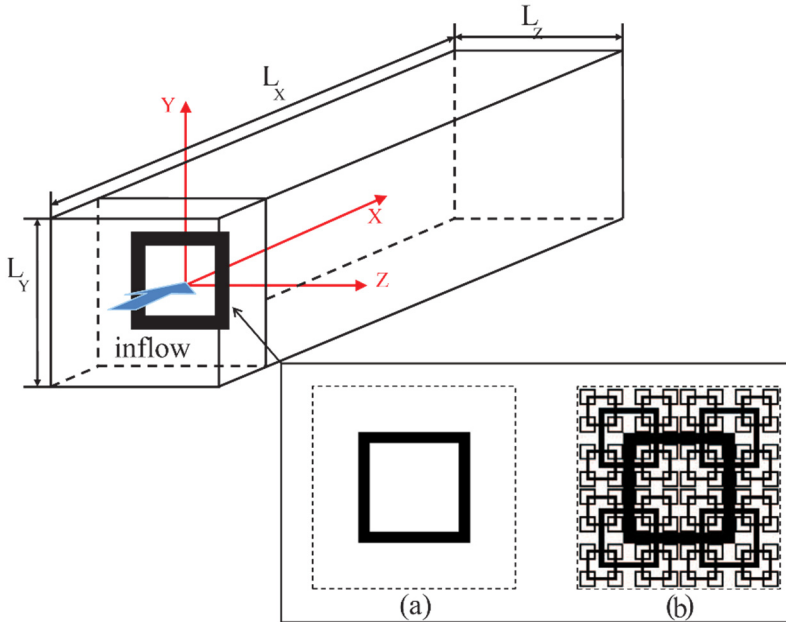


Fig. 1.8 - Schematic view of the computational domain and of the: (a) single square grid and (b) fractal square grid used in [36, 37, 38] (adapted from [37]).

As for the multiscale turbulators, they found, along the centreline, an extended turbulence production region (that is, however, not so surprising if we consider the assumption over which x_* is defined) with the axial velocity fluctuations reaching a maximum at $0.45x_*$, as documented by Mazellier and Vassilicos [27]. Moreover, in the decay region, close to the grid, they showed a similar behaviour between the single square turbulator and previous experimental results with regular grids, in agreement with the idea that a single square grid is a magnified regular grid. Concerning the spatial turbulent scales, their results showed that, along the grid centreline λ_u monotonically increases with the longitudinal distance, for $x/x_* \geq 0.2$; moreover Re_{λ_u} slightly decreases in the decay region, as for regular grids, but differently from fractal grids. Zhou et al. [37] also showed that a fractal grid can be decomposed into two parts, a main part (i.e. the largest bars) and a supplementary part, whose influence on the generated flow field only persists for a short distance from the grid itself. The turbulence due to the smallest bars can be regarded as an additional turbulence source that, in the near field, increases the decay rate of the

largest wake velocity deficit and is, therefore, responsible for a fast recovery from the initial inhomogeneity. The authors showed comparable features (e. g a faster wake decay rate, a small value of x_{peak} , high energy decay rate) in the near field of a 4-iteration square fractal grid with respect to a single square grid with the addition of homogeneous and isotropic turbulence. These similarities confirm that fractal grids are efficient additional turbulence generators.

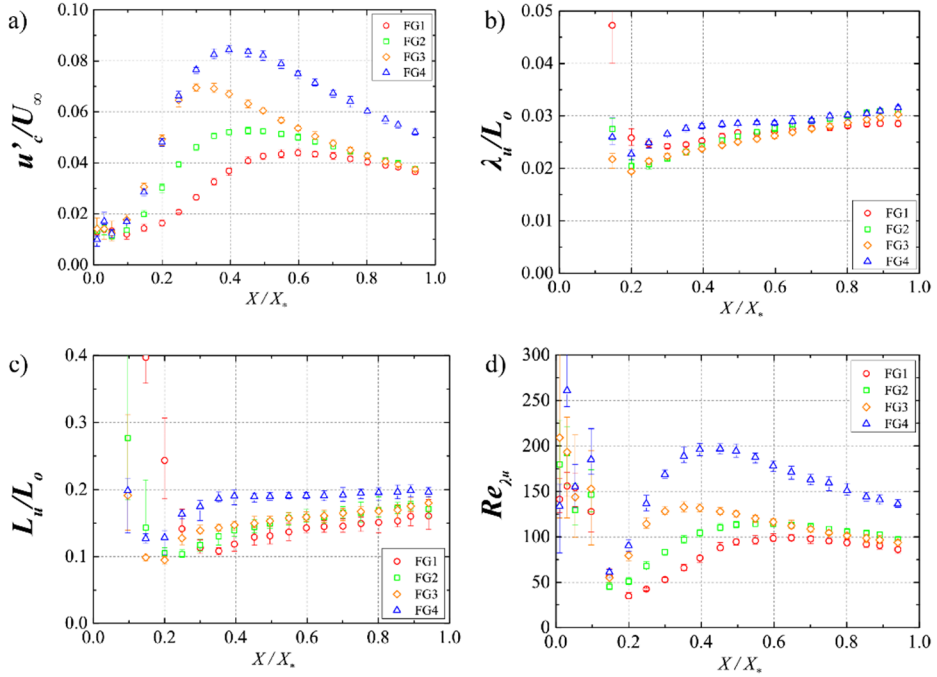


Fig. 1.9 - Downstream profiles, along the centrelines of the a) rms of the axial velocity fluctuations, b) dimensionless Taylor scale λ_u / L_0 , c) dimensionless integral length-scale L_u / L_0 , d) Re_{λ_u} , for the fractal grids (adapted from [39]).

Nagata et al. [39] performed hot-wire anemometry measurements on the flow field generated past eleven single- and multi-scale grids, grouped in square-fractal, regular, combined-regular and quasi-fractal grids, located at the entrance of a wind tunnel test section. Focusing on the square-fractal grid family, four grids, having $1 \leq N \leq 4$, were tested. Their results, as reported in Fig. 1.9, showed that, along the centreline, u' increases with N while the change in x_{peak} is not straightforward: it decreases with an increasing number of iterations up to $N=3$ and increases with $N=4$. The authors suggested this could be due to vortices shed by the grids' secondary iteration bars, which can suppress or strengthen the vortex shedding originated by the largest grid bar. In agreement with [23, 26, 27] both the Taylor and the integral length-scales, λ_u

1.2. FRACTAL-GENERATED TURBULENCE APPLICATIONS

and L_u , increase in the region $0.3 \leq x/x_* \leq 0.8$ for $N \leq 3$, whereas they are almost constant for $N = 4$, showing that the smallest iterations have a strong effect on the flow field development. Moreover, the centreline turbulent Reynolds number Re_{λ_u} varies with N according to u' since there are no significant effects of the number of iterations on λ_u . Finally, L_u/λ_u evaluated with respect to Re_{λ_u} for all the four square-fractal grids, shows that the increase in N causes a larger turbulence non-equilibrium region.

The effects of the secondary iterations bars have also been analysed in [40]. Their experimental results, obtained via hot-wire anemometry measurements, on the flow past a regular, a single square and a fractal square grid, showed that the increase of the bars' thickness of the single square grid can recover the defect in turbulence production (evaluated along the centreline) with respect to the fractal turbulator. They pointed out that the higher turbulence level is mainly due to a stronger vortex shedding generated by the grid's bars. Their results also showed that the secondary iterations of fractal grids can decrease the vortex shedding, with this reduction being responsible for a slower increase of the longitudinal integral length L_u in the decay region and a more non-Gaussian distribution of the u -velocity component in the production region.

1.2. FRACTAL-GENERATED TURBULENCE APPLICATIONS

Fractal-shaped elements have been successfully applied to many industrial fields such as the mixing [41, 42, 43, 44, 45, 46], aeronautical [47, 48, 49], automotive, power generation and wind energy [50] industries.

In 2010, Mazellier et al. [41] first proposed multi-scale injectors, formed by multiple perforated plates having blockage ratios varying between 50% and 70%, for premixed combustion, pointing out their capability of producing larger turbulent kinetic energy intensities, distributed over a wider range of scales, with respect to the mono-scale injectors. Moreover, they cause an extremely rapid transition to the isotropic and homogeneous turbulence regime. The multi-scale-generated turbulence also interacts with the flame at both large and small scales, affecting its global shape, causing a much larger wrinkling of the front flame edges which promotes the penetration of unburnt gas pockets deep inside the burnt gases.

Geipel et al. [42], and then Goh et al. [43], proposed cross-fractal grids (see Fig. 1.10) in the context of opposed jet geometries, extensively used to study combusting laminar and turbulent flows, showing that the fractal grids increase the turbulent

Reynolds number range as compared to the conventional perforated plates, without any significant negative consequences for other flow field parameters.

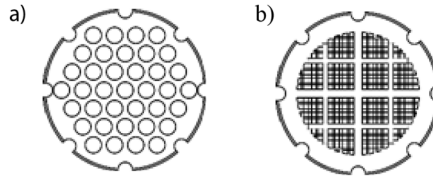


Fig. 1.10 - Schematic of the perforated and cross-fractal plates used in [43].

In [44, 46] square-fractal grids have again been tested as turbulence generators in premixed combustion applications and compared to classical regular grids. Even in this case they found that fractal geometries produce more wrinkled flames, higher effective flame surface area (due to their ability to produce larger turbulence intensities over a well-defined downstream region) and higher turbulent burning velocities (with this increase being beneficial, e.g. for extending the lean stability limit for a given heat release rate). All these promising results demonstrate that the square-fractal grids could be applied as innovative solutions in order to achieve a more stable combustion process.

In [48], Nedić et al. proposed fractal geometries to reduce the noise generated by the aircraft spoilers, that, during the landing operations, accounts for about the 26% of the total aircraft noise. Indeed, the spoilers, deployed to reduce the lift on the aircraft, generate low frequency noise due to the large-scale structure that develops in their lee: the re-circulation bubble. This low frequency noise is less susceptible to atmospheric attenuation and can travel much further than the high frequency one, affecting the acoustic comfort near the airport. Considering that porous fences had already been identified as efficient solutions for moving downstream this re-circulation bubbles, they suggested that large-scale fractal porosity, due to their promoted multiple length-scales turbulence, could reduce the impact of the re-circulation regions and with them the low frequency noise they generate introducing high frequency noise which is more sensitive to atmospheric attenuation and less offensive to human ear. Testing nine different spoilers, seven of which designed with three fractal iterations, one designed using a regular grid (see Fig. 1.11) and a solid one, they showed that the central frame size and thickness ratio play a key-role on the spoiler aerodynamics and acoustic performances. In particular, the analysed square fractal spoilers were able to reduce the low frequency noise up to $4dB$, whilst slightly affecting the lift and the drag characteristic of the wing section.

1.2. FRACTAL-GENERATED TURBULENCE APPLICATIONS

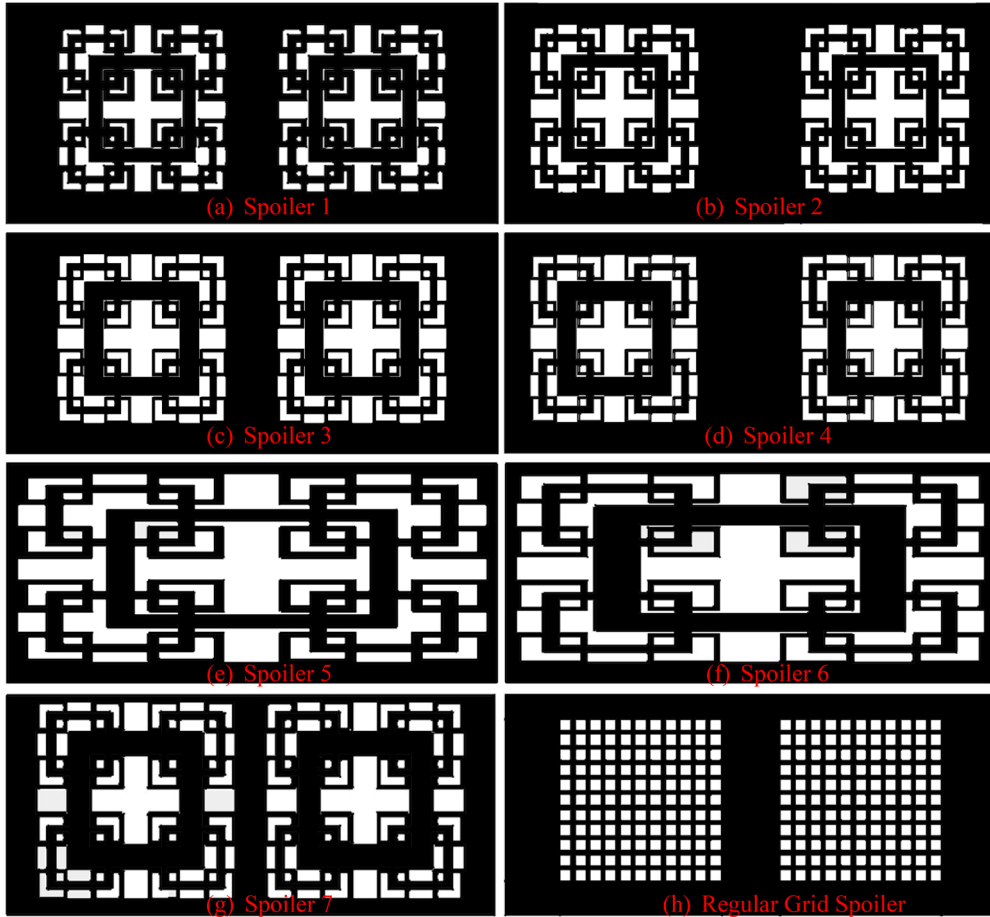


Fig. 1.11 - Sketch of eight spoilers used in [48].

Fractal geometries have also proved to be an effective solution for modifying (eventually suppressing) the vortex shedding [40, 49, 50]. Experimental measurements on the turbulent wakes produced by fractal plates (see Fig. 1.12) with respect to the case of circular and square ones, all characterised by the same frontal area, have shown that the fractal shape is able to reduce the vortex shedding energy by up to 60% compared to the circular and square plates, without affecting the vortex shedding frequency (purely dependent on the “global” length scale and, therefore, on the frontal area). However, despite a lower intensity, (that decreases more and more as the number of iterations and the fractal dimension increase), it takes longer for this energy to decay (contrary to what found in [40]). The fractal multi-scale nature redistributes the energy on a broader [37] range of scales in the flow, affecting the wake size, the drag coefficient C_D , (showed to increase up to 7% for the tested plates) and the physical extent of the wake non-equilibrium region. Particularly, the decrease in

the vortex shedding energy causes the decrease in size of the wake while the drag coefficient, C_D , depends on both the wake volume coefficient C_V (relative to the large-scale structures) and the average rate of turbulent kinetic energy dissipation in the entire wake C_ε (related to the small-scale structures), as $C_D = C_\varepsilon C_V$. The increase of the fractal iteration number causes the drag coefficient to increase up until a threshold value, after which there is a noticeable drop. Indeed, as the fractal geometry is introduced, C_D increases since the increase in C_ε is larger than the decrease in C_V . However, at a certain point, the decrease in C_V can become insurmountable and C_D decreases for higher fractal iteration numbers.

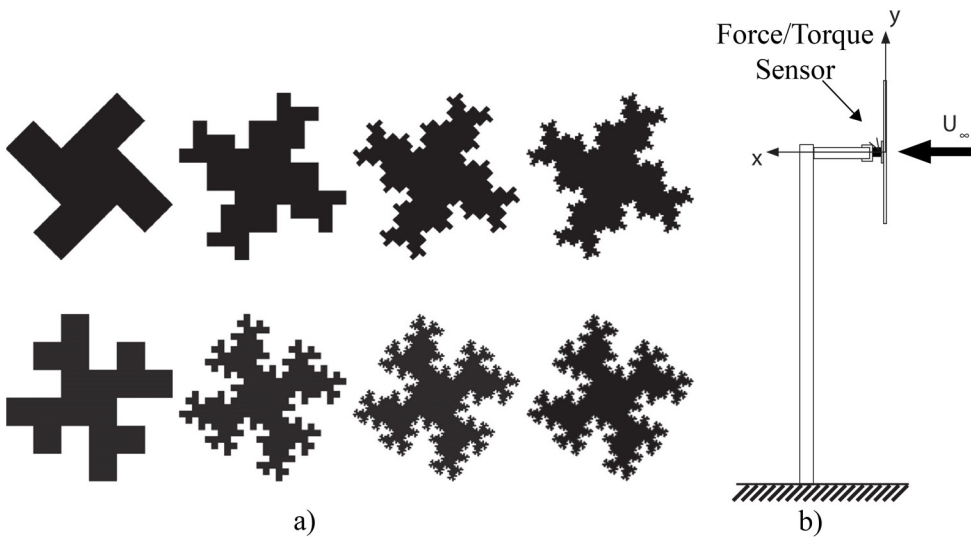


Fig. 1.12 Schematic of: a) some of the fractal plates analysed in [50]; b) the plates' support (adapted from [50])

Strong variations of the vortex shedding properties are also visible in applying fractal/multi-scale modifications to a non-flat serrated trailing edge of a wing section [47]. Sketches representing the fractal iterations and the trailing edge modifications are reported in Fig. 1.13. The increase in the number of the fractal iterations causes a reduction of the vortex shedding energy, but only if the fractal dimension D_f is large enough, i.e. if the chevron angle φ (see Fig. 1.13) is smaller than 45° . In this case, a low frequency noise reduction can be obtained because of the mixing/vortex breakdown due to the multi-scale geometry without affecting the chevron-wing aerodynamic performances.

Fractal-shaped blades for increasing the mixing quality of unbaffled stirring tanks have been experimentally [45] and numerically [51, 52] analysed. By measuring the power consumption of turbines with one or two fractal iteration blades with respect

1.2. FRACTAL-GENERATED TURBULENCE APPLICATIONS

to rectangular ones, over a certain range of $Re_m = \mathfrak{m}d^2/\nu$ (where \mathfrak{m} is the rotational frequency and d is the distance between the shaft centre to the mean tip), Steiros et al. [45] found that the multi-scale pattern causes a sensitive reduction of the power number with respect to the regular impeller, which also increases as the number of iteration increases (namely 11 – 12% for $N = 1$ and 17 – 20% for $N = 2$). They showed that the reduction of the required shaft torque is due, on one side, to the interaction between the wakes generated by the blades and the tank wall and, on the other side, to a reduction of the blades drag coefficient (which does not agree with the results reported in [47, 48, 49, 50] for wind-tunnel measurements) and an increase of the centre of pressure radii due to the fractal geometry.

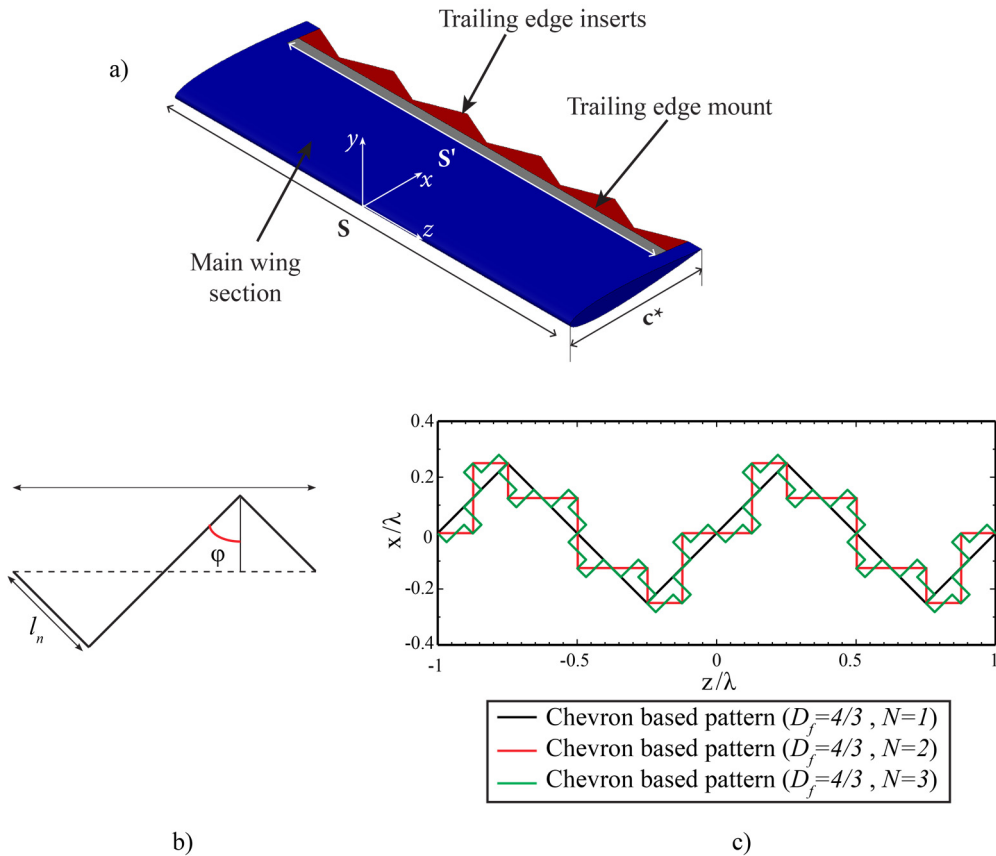


Fig. 1.13 - a) Drawing of the main wing and trailing edges tested in [47] (adapted from [47]); b) illustration of a fractal iteration; c) drawing of the tested trailing edges reported in [47] (adapted from [47]).

Further results reported in [52] have also shown that the drag coefficient reduction obtained by means of fractal-shaped blades is due to a smaller flow separation region

and to lower values of the azimuthal velocity component in the blades' wake with respect to the regular impeller. These differences emerge because of the concave edges of fractal blades, which allow the upcoming fluid to penetrate within the separation region, and because of the smaller and multiple trailing vortices that directly affect the recirculation region on the suction side of the impeller period.

Their high performances in terms of scalar mixing and transport also encouraged Cafiero et al. [1, 2, 3, 4] to apply square fractal grids to impinging round jets (see Fig. 1.14), widely used for electronic device cooling, glass shaping, anti- and de-icing devices, etc. In [1], the authors demonstrated that, under the same power input conditions, the introduction of a 3-iterations fractal promoter, located within 1 diameter from the nozzle exit section, could significantly enhance the heat transfer properties of round impinging jets, above all at small nozzle-to-plate distances (Fig. 1.15). A consistent enhancement was also found with respect to the introduction of a regular grid having the same solidity (in particular, they showed, in the stagnation region, an improvement in terms of Nusselt number Nu_0 up 63% and 45% with respect to a round jet and a regular grid under the same power input).

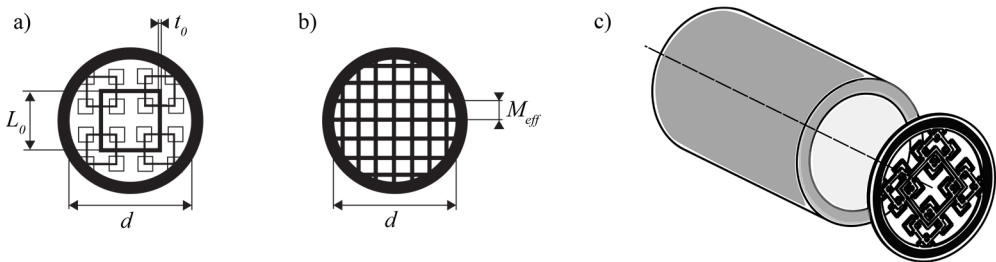


Fig. 1.14 - a) Sketch of the fractal grid used in [1]; b) sketch of the regular grid used in [1]; detail of the device exit section [1].

Subsequent 2D and 3D measurements, performed by means of planar and tomographic Particle Image Velocimetry (PIV), on both the free [2] and the impinging [3] round turbulent jet equipped with the same 3-iterations square fractal grid showed the main factors that are responsible for this enhancement, namely:

- the higher turbulence intensity levels due to fractal pattern;
- the ability of the fractal turbulator to produce streamwise vorticity, which causes an increment of the entrainment rate.

1.3. OBJECTIVES

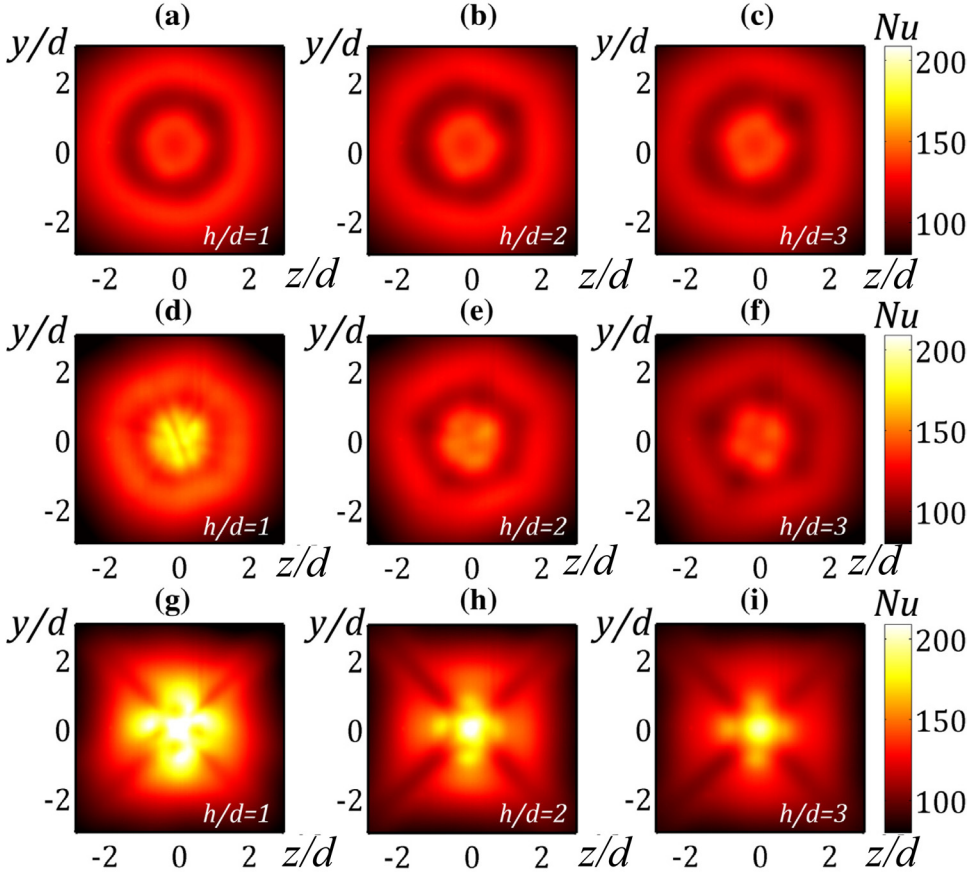


Fig. 1.15 - Nusselt number maps for the round jet -a- c) without turbulators; d-f) with the regular grid; g-i) with the fractal grid (insert located at the nozzle exit section) at three different dimensionless nozzle-to-plate distances, h/d (adapted from [1]; here d is the nozzle diameter).

1.3. OBJECTIVES

In their works, Cafiero et al. [2, 3] only focused on the effects of a 3-iterations square-fractal grid on the flow field of a round turbulent jet, pointing out its efficiency in terms of turbulence production, above all at short distances from the nozzle.

As in previous works on fractal-generated turbulence [23, 26, 27, 28, 29, 32, 33, 37, 39], they found that the velocity fluctuations rapidly increase along the jet centreline, reaching a local maximum at about $x = 0.4x_*$, (i.e. $0.4L_0^2/t_0$). The practical relevance of this result is easily said, as it suggests that it possible to optimise the scalar transfer of turbulent jets by simply tampering with the grid

geometrical parameters. However, some open questions remain on the interaction between fractal-generated turbulence and turbulent jets. Among the others:

- Are these peculiar features related to the multiscale turbulence generation or can they also be achieved by means of a single square grid having same L_0 and t_0 ?
- What happens if square-fractal grids are inserted at the exit section of a synthetic jet device and how does the vorticity produced by the grids interact with the vortex ring generated at the nozzle edges?
- What happens if we change t_0 while keeping σ fixed both in terms of velocity flow field and heat transfer rate?

The results reported in the following aim to answer these questions, focusing both on flow field developed suddenly past the grid and at large distances from the nozzle, where the interaction with the jet shear layer can be observed. Comparisons with the jet without turbulators and the jet equipped with the more conventional regular grids are also reported.

1.4. OUTLINE

The remainder of this thesis is structured as follows.

In Chapter 2 a brief description of the used experimental techniques is given. The experimental rigs are introduced in Chapter 3 together with a concise description of both the continuous and the synthetic jets flow fields.

The effects of the secondary iterations on continuous axisymmetric turbulent jets are assessed in Chapter 4. Experiments are performed, by means of planar PIV, at a fixed global Reynolds number, on a continuous jet device equipped with either a single square fractal grid or a 3-iterations square-fractal grid (having same L_0 and t_0). Similar measurements are also performed on a synthetic jet device: the obtained results are discussed in Chapter 5 for three different device actuation frequencies and for the same Reynolds number used in Chapter 4 in order to make reliable comparisons. In both the chapters, particular attention is given to the impact of the grid geometry on the coherent vortical structures generation and development.

In Chapter 6, the effects of the introduction of secondary iterations as also of their different thickness ratio t_r in terms of heat transfer properties is analysed by means of IR Thermography combined with the heated-thin-foil heat flux sensor. Measurements are performed under the same power input to properly assess grids' efficiency.

1.4. OUTLINE

In Chapter 7, the effects of the bars thickness ratio on the turbulent continuous jet velocity field are investigated by means of 2D-2C PIV. The contribution of the secondary iterations of square fractal grids on the jet large-scale isotropy and on the redistribution of the turbulent kinetic energy on the different spatial scales are also assessed.

Finally, conclusions and future perspectives are drawn.

2. MEASUREMENT TECHNIQUES

In this chapter, a brief description of the measurement techniques used to carry out the experimental work discussed in this thesis is reported. In §2.1 the working principles of Particle Image Velocimetry (PIV) are briefly drawn (a more detailed description can be found in [53, 54]). Infrared (IR) Thermography and its application in convective heat transfer measurements are presented in § 2.2. In particular, a brief description of the *heated thin foil heat flux* is given in § 2.2.4 (more details can be found in [55]).

2.1. FUNDAMENTALS OF PARTICLE IMAGE VELOCIMETRY

PIV is a non-intrusive anemometric technique that allows to measure velocity fields within an investigated region if opportunely illuminated, imaged and seeded. Standard PIV measures two velocity components in a plane (2D-2C PIV) using only a single camera, while more than one camera is needed to measure all the three velocity components, in a plane (Stereoscopic PIV [56]) or in a volume (Tomographic PIV [57, 58]).

The experimental setup needed to perform PIV measurements typically consists of several subsystems: a light source that provides a uniform illumination of the investigated region, one or more cameras allowing to capture two or more frames at short temporal distance, a device to produce opportune tracer particles and a system to manage and analyse the amount of acquired data.

A sketch of a typical planar PIV setup is reported in Fig. 2.1. Tracer particles are introduced into the flow. A plane within the flow is illuminated by means of a laser, with a time distance between the consecutive pulses chosen depending on the mean flow velocity and the camera magnification. It is assumed that, between the two laser pulses, the tracer particles move with the (instantaneous) flow. The light scattered by the tracer particles is recorded via cameras, normally using two separate frames per each laser pulse, and analysed by means of a computer.

For evaluating the PIV recordings, the images are divided in smaller areas, usually referred to as “interrogation windows”. It is assumed that all the particles within an interrogation window move homogeneously between the two laser pulses. For each interrogation area, the local displacement vector of the tracer particles, between two time instants, is determined, using a cross-correlation based algorithm [59].

2.1. FUNDAMENTALS OF PARTICLE IMAGE VELOCIMETRY

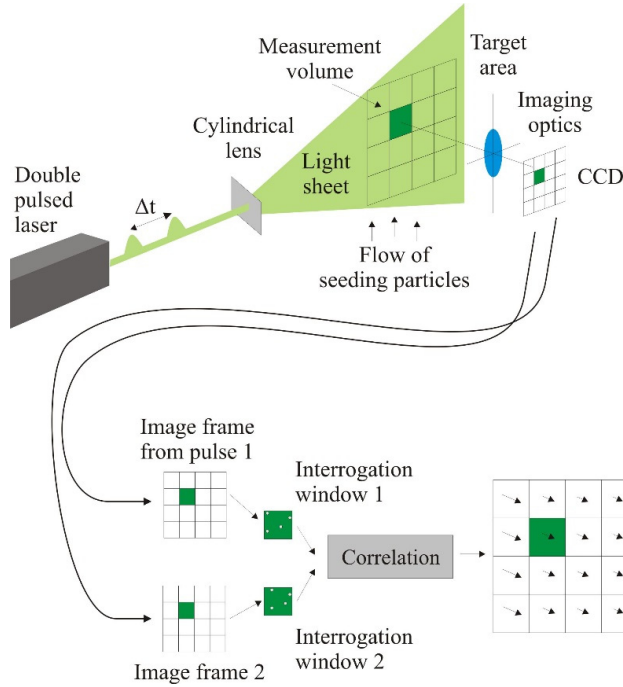


Fig. 2.1 – Schematic representation of a common PIV setup ([60]).

A more accurate measurement of the displacement is achieved by means of iterative image deformation methods [61, 62]. The proper choice of the interrogation window size is of paramount importance as it directly affects the spatial resolution. The interrogation areas must be small enough to assume that all the particles in the window have almost the same displacement. On the other hand, the interrogation window size determines the number of independent velocity vectors that can be obtained. However, it is also limited by the number of independent tracer particles that can be used for the correlation: a general rule-of-thumb is that for planar PIV at least 9 – 11 particles per interrogation window are needed to obtain a well-defined correlation peak. This number can be decreased down to 5 – 7 in the case of tomographic techniques because the particles do not leave the investigated illuminated region. Once the planar displacements Δx and Δy are measured, the planar velocity components u and v , into the laser sheet plane, can be evaluated taking into account the time delay and the images' magnification:

$$\begin{Bmatrix} u \\ v \end{Bmatrix} = \frac{M_0}{\Delta t} \begin{Bmatrix} \Delta x \\ \Delta y \end{Bmatrix} \quad (2.1)$$

where Δt is the temporal separation between the two successive frames. This value must be accurately fixed in order to obtain displacements of the particles, onto the image plane, of about 8 – 12 *pixels*. In Eq. (2.1) M_0 is representative of the

magnification factor, calculated as the ratio between z_0 , which is the distance between the lens and the image plane, and Z_0 , which is the distance between the lens and the target plane.

2.1.1. EXPERIMENTAL DETAILS

- SEEDING PARTICLES

Seeding the flow with light reflecting particles is usually required to image the flow field. Generally, natural seeding is insufficient and tracer particles must be added to the flow. Sometimes, it can be done quite easily, as for example in most liquid flows where solid particles are normally mixed to the fluid. In other cases, devices such as atomizers, condensation generators, smoke generators or Laskin nozzles are needed to produce small enough tracer particles [53].

A number of different materials can be used for flow insemination: the choice of the proper seeding particles is strongly dependent on the working fluid, since the tracers must be capable to accurately follow the fluid without perturbing it.

For tracer particles operating in the Stokes regime (i.e. for particle dynamics dominated by the viscous drag), and if the density of the tracer particles ρ_p is much greater than the fluid density ρ , a good estimator is represented by the particle relaxation time τ_s , given by:

$$\tau_s = \left(\frac{\rho_p}{18\mu} \right) d_p^2 \quad (2.2)$$

being d_p the dimension of the tracer particles and μ the working fluid dynamic viscosity. A reduction of the relaxation time causes a better tendency of the particles in following the fluid flow. However, the particles must be large enough to scatter a sufficient amount of light.

- ILLUMINATION AND CAMERA SYSTEM

Since collimated intense pulses of light at short temporal distance are often needed, pulsed lasers are usually used for PIV applications. Depending on the working acquisition frequency, lasers are usually divided in Nd:YAG or Nd:YLF lasers. The formers are generally used for low-frequency PIV applications (up to 15 Hz) and are characterised by a high energy content per pulse (from 100 up to 800 mJ/pulse) and by a working wavelength λ_l of 532 nm. The latters are characterised by a lower energy content (up to 30 mJ/pulse) but by high acquisition

2.1. FUNDAMENTALS OF PARTICLE IMAGE VELOCIMETRY

frequencies (up to dozens of *KHz*) and by a working wavelength λ_l of *526 nm*.

When setting the illumination pulse duration, it is important to be considered that it must be short enough to “freeze” the motion of the particles during the pulse exposure in order to avoid blurring of the images. Moreover, the time delay between the illumination pulses must be long enough to determine the particles displacement between the images with a sufficient resolution. On the other hand, it must be short enough to avoid particles with an out-of-plane velocity component to leave the light sheet between the two subsequent illuminations and to avoid an excessive error associated with the linearization of the particle path.

The particles distributions are recorded by means of cameras equipped with CCD (Charge Coupled Device) or CMOS (Complementary Metal-Oxide Semiconductor) sensors, of which the latter type of devices is less expensive and capable to work at higher frequencies, but is characterised by lower signal-to-noise and lower resolution with respect to the former one. Recent cameras equipped with sCMOS (scientific Complementary Metal-Oxide Semiconductor) sensors simultaneously offer rapid frame rates, high resolution and low-noise acquisition.

The sensors size, at this stage of technology, ranges from 1 to 29 *Mpixels* while the acquisition frequency must be aligned to that of the light source.

- **PARTICLE IMAGING**

Particles are formed on the camera sensor via a high-quality lens. Their diameter depends both on the particles size and the lens properties. Given the ratio between the focal length and the aperture diameter, $f_{\#}$, the diameter of the in-focus particle, neglecting lens aberrations, is:

$$d_{\tau} \approx \sqrt{d_{geom}^2 + d_{diff}^2} = \sqrt{(M_0 d_p)^2 + (2.44 f_{\#} (1 + M_0) \lambda_l)^2} \quad (2.3)$$

where d_p is the particle physical diameter, d_{geom} is the geometric image diameter due to the magnification and d_{diff} is the diffraction-limited diameter, which expression is evaluated by approximating the Airy disk with a Gaussian function [53].

The particle image diameter should be minimized to reduce the uncertainty in the displacement measurement and to ensure strong light intensity (as the collecting light scales with the inverse of the particle area). However, if the particle diameter is smaller than 2 *pixels*, *peak-*

locking (i.e. a bias effect towards integer pixel values) can occur [63]. A common rule is to set the imaging system in order to have d_τ larger than 2 and smaller than 5 *pixels*.

Moreover, considering that the light sheet has a finite thickness Δz_0 , the particle images will be focused only if Δz_0 is smaller than the depth of field δ_z , evaluated as [64]:

$$\delta_z \approx 4.88 \left(1 + \frac{1}{M_0}\right)^2 f_\#^2 \lambda_l \quad (2.4)$$

- SEEDING DENSITY

The choice of a correct seeding is also crucial to perform a proper PIV experiment. Depending on the desired spatial resolution, the image density may vary a lot! The parameters that is usually looked at, to properly set the seeding density, is the particle per pixel (*ppp*) (rigorously, the seeding density is influenced by the source density $N_s = ppp \frac{\pi}{4} (d_\tau / \Delta pix)^2$ where Δpix indicates the pixel size, that is, however, not easy to evaluate). Nowadays, in planar PIV applications, *ppp* commonly ranges between 0.05 and 0.2.

2.2. INFRARED THERMOGRAPHY

Infrared (IR) Thermography is a measurement technique that enables to obtain non-intrusive measurements of surface temperatures by detecting the energy emitted in the IR band from the objects. It is used in numerous industrial applications, such as non-destructive inspection of composite materials, detection of possible leakages, missing isolation or moisture damage in buildings, detection of faulty connections in electrical and mechanical systems, to cite some.

2.2.1. THEORETICAL BACKGROUND

Heat transfer by radiation is an energy transport mechanism that occurs by means of electromagnetic waves. Contrary to the case of heat conduction and convection, energy transmitted by thermal radiation is the only mechanism enabling the energy transmission between two bodies placed in vacuum. If a medium is present between the two bodies, the transmitted radiation may be partially or completely absorbed and/or reflected by the medium. Finally, the medium is referred to as *fully transparent* if the transferred energy passes through it without downgrading and this practically

2.2. INFRARED THERMOGRAPHY

enables an IR transducer to view the temperature of the body without touching it. A medium is referred as *partially transparent* if it allows only a fraction of the transmitted energy to pass through.

All the materials above the absolute zero ($0K$) emit energy by means of electromagnetic waves because of the movement of their atoms and molecules. The amount of thermal radiation absorbed or emitted by a body, as well its propagation, depends on the nature of the material and on the surface finish, as also on its thermodynamic state and on the specific wavelength of the considered electromagnetic wave.

The wavelength λ_c is related to the wave frequency ν by the speed of light (or speed of propagation) c in the medium:

$$\lambda_c = \frac{c}{\nu} = \frac{c_0}{n\nu} \quad (2.5)$$

where c_0 is the speed of propagation in vacuum and n is the dimensionless *index of refraction* of the medium, which, in general, depends also on the wavelength.

The electromagnetic spectrum is divided into wavelengths intervals, called *spectral bands*, as shown in Fig. 2.2. It extends from very small wavelengths ($\lambda_c \rightarrow 0$) to extremely large ones ($\lambda_c \rightarrow \infty$).

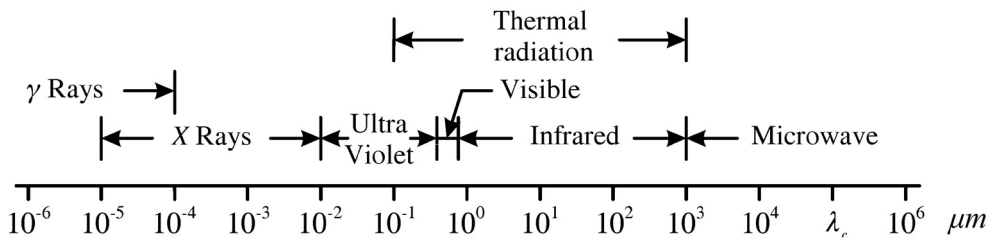


Fig. 2.2 - Electromagnetic spectrum (adapted from [55]).

Fig. 2.2 shows that the *thermal radiation* band is conventionally positioned between $0.1 \mu m$ and $1000 \mu m$, including part of the ultraviolet and all the visible and the IR bands. At ambient temperature, most of the energy emitted by a body is in the IR spectral band. This band is usually subdivided in: *near infrared* ($3 \div 6 \mu m$), *far* or *long infrared* ($6 \div 15 \mu m$) and *extreme infrared* ($15 \div 1000 \mu m$). IR camera temperature detectors used for standard thermo/fluid-dynamics applications are usually sensitive in either the middle (MWIR) or long wavelength (LWIR) spectral bands, with the band between $\sim 5 \mu m$ and $\sim 7.5 \mu m$ rarely used because of its rather high atmospheric absorption.

When the temperature of a body is above $0 K$, their molecules and atoms are moving, thus radiation is constantly emitted, absorbed or transmitted. However, some

materials are opaque (i.e. completely non-transparent) and, in this case, the incident radiation can be absorbed within few micrometres of the body skin. For these reasons, radiation can be considered as a surface phenomenon. Therefore, by coating the surface of a body with a very thin layer of opaque material, its surface radiation properties can be significantly changed and this effect may be very useful when using IR instruments to measure the surface temperature. In this context, it is useful to introduce a conceptual body, usually referred to as *black body*, which has the property of being a perfect absorber (i.e. it absorbs all the incident radiation, regardless of its wavelength and direction) and emitter (i.e. it emits the maximum possible amount of energy) of radiation. It is also a *diffuse emitter* as it emits radiation uniformly in all the directions.

The energy flux (i.e. the energy rate per body unit surface area) per wavelength, called *spectral hemispherical emissive power* $E_{b\lambda_c}$, emitted by a black body in vacuum, is given by the *Planck's law of radiation*:

$$E_{b\lambda_c}(\lambda_c, T) = \frac{C_1}{\lambda_c^5 (e^{\frac{C_2}{\lambda_c T}} - 1)} \quad (2.6)$$

where T is the absolute body temperature (in K) and $C_1 = 3.742 \cdot 10^{-6} Wm^2$ and $C_2 = 1.439 \cdot 10^{-6} Km$ are the first and the second radiation constants.

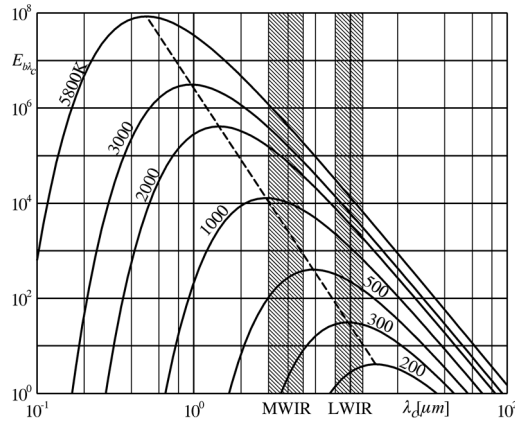


Fig. 2.3 - Spectral hemispherical black body emissive power ($W/m^2\mu m$) in vacuum for several absolute temperature values (K) as a function of the wavelength (adapted from [55]).

Eq. (2.6) is plotted in Fig. 2.3 as a function of λ_c : the maximum of $E_{b\lambda_c}$ increases and shifts towards lower values of λ_c as the absolute temperature increases. The equation of the dashed line, representative of the locus of maxima in Planck's equation and referred in literature as *Wien's law*, is given by:

2.2. INFRARED THERMOGRAPHY

$$\lambda_{c,max}T = 2898 (\mu m \cdot K) \quad (2.7)$$

Eq. (2.7) allows determining, for a given temperature, the wavelength at which a black body emits its maximum spectral emissive power.

By integrating Eq. (2.6) over the whole spectrum the *Stefan-Boltzmann law* is obtained:

$$E_b = \int_0^{\infty} E_{b\lambda_c}(\lambda_c, T) d\lambda_c = \bar{\sigma}T^4 \quad (2.8)$$

where $\bar{\sigma} = 5.670 \cdot 10^{-8} W/m^2K^4$ is known as Stefan-Boltzmann constant.

The radiation characteristics of real bodies are different from those of a black body, as real bodies only absorb a fraction of the incident radiation. The remaining part may be partially reflected by and/or partially transmitted across the bodies themselves (see Fig. 2.4). By denoting with α_r the fraction of irradiation absorbed by the real body, with ρ_r the fraction of irradiation reflected and with τ_r the fraction of irradiation transmitted through it, the energy conservation requires:

$$\alpha_r + \rho_r + \tau_r = 1 \quad (2.9)$$

where α_r , ρ_r and τ_r are respectively referred to as *absorptivity*, *reflectivity* and *transmissivity* coefficients of the body under consideration. They are positive and smaller than, or at most equal to 1, and, generally, depend on the body material, on its surface finish, on its thermodynamic state as well as on the wavelength and direction of the incident radiation.

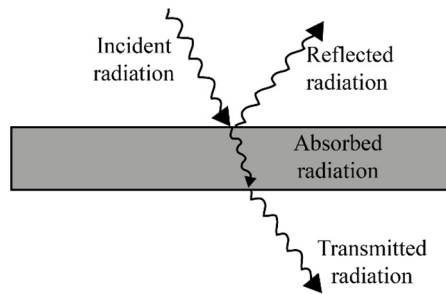


Fig. 2.4 - Reflection, absorption and transmission of the incident radiation in a slab (adapted from [55]).

In addition, the emission from real opaque bodies is different from that of a black body and does not exactly follow Planck's law: the radiation emitted from a black body is an upper limit that can be only reached in certain spectral bands and under

certain conditions. Therefore E_{λ_c} , defined as the *spectral hemispherical emissive power* of a real body, is lower or at most equal to $E_{b\lambda_c}$:

$$\varepsilon_{\lambda_c}(\lambda_c, T) = \frac{E_{\lambda_c}}{E_{b\lambda_c}} \leq 1 \quad (2.10)$$

where ε_{λ_c} is the *spectral hemispherical emissivity coefficient*.

Similarly, by defining E as the *total hemispherical emissive power* of a real body, it is possible to introduce the *total hemispherical emissivity coefficient* ε_t :

$$\varepsilon_t(T) = \frac{E(T)}{E_b(T)} \leq 1 \quad (2.11)$$

In general, the spectral emissivity of a real body may strongly depend on the wavelength and the direction of the emitted radiation, as also on the emitting body material and composition and on the surface conditions. Bodies whose emissivity is not dependent on λ_c are referred to as *grey bodies*. Even if no real surface is truly grey in this sense, it often happens that real surfaces have an almost constant emissivity in the used IR detector band so that, from a practical point of view, the grey body hypothesis can be considered valid.

For diffuse emission, *Kirchhoff's law* states that, in thermal equilibrium, the spectral emissivity coefficient is equal to the spectral absorptivity one, $\alpha_{r\lambda_c}$. This means that, for opaque bodies (i.e. with $\tau_r = 0$), such as those generally used for measurements with IR thermography, Eq. (2.9) becomes:

$$\varepsilon_{\lambda_c} + \rho_{r\lambda_c} = 1 \quad (2.12)$$

As a consequence, materials with low emissivity also reflect a large amount of the radiation coming from the ambient and impinging on them. Therefore, whenever possible, they should not be employed in infrared applications, or if they must be used and transient heat transfer is not involved, they must be covered by a thin layer of thermally-black paint.

2.2.2. IR SCANNING RADIOMETERS

A schematic representation of an infrared scanning radiometer is shown in Fig. 2.5: the thermal radiation, captured by the scanner, is collected by an optical system and sent into a temperature detector, sensitive to the chosen IR band. The electrical signal generated by the detector is acquired and processed by a dedicated electronic board to obtain the temperature map of the scanned region.

2.2. INFRARED THERMOGRAPHY

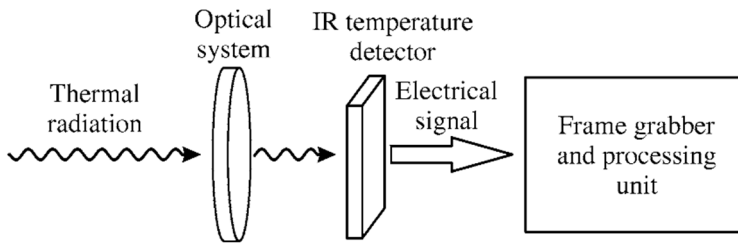


Fig. 2.5 - Schematic representation of an IR scanning radiometer (from [55]).

The main parameters defining the performances of an *IR scanner* (also called *IR camera*) are herein summarised.

- THERMAL SENSITIVITY

The thermal sensitivity is usually expressed in terms of mean *noise equivalent temperature difference* (NETD), defined as the time standard deviation of random background noise averaged over all pixels of a black body scene [65]. The NETD is a function of the used black body temperature and is provided, at ambient temperature, by the IR camera manufacturer. At 20 °C, modern uncooled IR scanners have a typical NETD value of about 100 mK, while cooled devices may also reach values ranging around 10 mK.

- SPATIAL RESOLUTION

The *spatial resolution* determines the capability of the IR scanner to measure the surface temperature of small objects or to resolve the temperature differences between two points at relatively short distances. The *instantaneous field of view* (IFOV), which is the ratio of the detector size width over the lens focal length, gives a simplistic definition of the spatial resolution and is usually measured in *rad*. A rigorous definition of the spatial resolution is given in terms of the scanner *Modulation Transfer Function* (MTF). From a physical point of view, it represents the ratio between the measured amplitude, A_m , and the real amplitude, A_r , of a sinusoidal thermal signal detected by the camera, as shown in Fig. 2.6.

- ACQUISITION FREQUENCY

The *acquisition frequency* is an important parameter in transient phenomena measurements. IR cameras producers typically report the rate of acquisition of a complete thermal image in terms of the number of full frames acquired per second (*Hz*). The acquisition frequency can be increased by reducing the number of acquired pixels, however it is limited

by the minimum integration time needed by a detector pixel to measure correctly the temperature of the target object so that, for low object temperatures, the maximum acquisition frequency could be smaller than that for higher ones.

- TEMPERATURE AND DYNAMIC RANGE

The *temperature range* measured with an IR scanner usually spans from -20 to $1500\text{ }^{\circ}\text{C}$, but it can be further extended to higher values by adequately filtering the incoming radiation.

The *intensity resolution*, or *dynamic range*, is evaluated in terms of the number of digital intensity levels corresponding to each individual pixel.

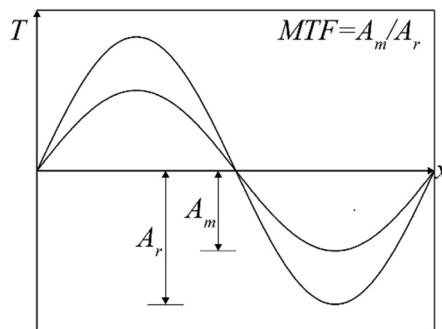


Fig. 2.6 - Illustration of the modulation effect (adapted from [55]).

2.2.3. IR SCANNER RADIOMETRIC CALIBRATION

A calibration function is needed to convert the output electrical signal produced by an IR scanner into the target temperature. Most of the modern cameras are already calibrated so that an embedded software directly delivers a 2D temperature map. Nevertheless, often a more accurate calibration or a recalibration (for example to extend the camera temperature range) is required, especially in those cases in which the camera is not compensated for the external temperature.

As schematically shown in Fig. 2.7, the thermal radiation acquired by the IR camera is not only the one emitted by the imaged target. The scanner also detects an amount of radiation emitted by the external ambient and reflected from the target towards the camera and an amount of radiation emitted by the atmosphere. Moreover, the attenuation due to the atmosphere on the radiation emitted by the target must be considered. Usually these problems, as also the ones due the radiation emitted by the camera itself and by the lens, are handled by the camera software, however many other contributions may arise and, if they could significantly affect the measurements,

2.2. INFRARED THERMOGRAPHY

the operator must identify the problems and correct them. Besides, it is recommended to realise around the camera an isothermal environment, at a known temperature.

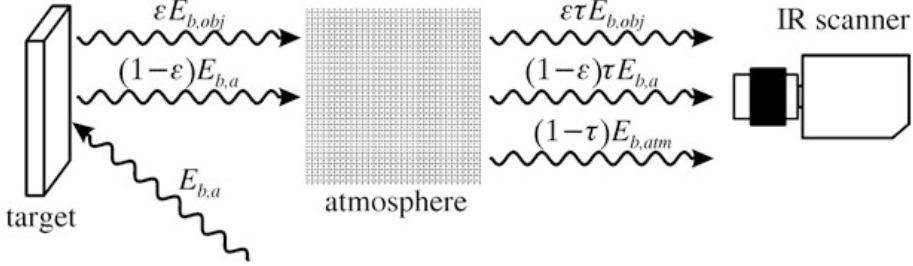


Fig. 2.7 - Schematic description of the radiation detected by the IR camera (from [55]).

As previously said, the radiation flux emitted by the viewed opaque target is a function of the radiation flux emitted by a black body $E_{b,obj}$ at the same temperature. Therefore, by defining τ_r as the transmissivity coefficient of the atmosphere, the radiation collected by the target is $\varepsilon_t \tau_r E_{b,obj}$.

If the surrounded environment is at constant temperature T_a and its extension is large with respect to the viewed target, it can be considered as a black body and thus the radiation emitted is $E_{b,a}$. Since the target is an opaque body, its reflectivity coefficient can be evaluated as $(1 - \varepsilon_t)$, so that radiation related to the ambient and detected by the camera is $(1 - \varepsilon_t)\tau_r E_{b,a}$.

Similarly, by supposing that the atmosphere temperature T_{atm} is constant and the atmosphere emissivity is $(1 - \tau_r)$, the radiation flux related to the atmosphere that reaches the camera is $(1 - \tau_r)E_{b,atm}$.

Therefore, the total radiation flux $E_{IR,c}$ collected by the IR camera is:

$$E_{IR,c} = \varepsilon_t \tau_r E_{b,obj} + (1 - \varepsilon_t)\tau_r E_{b,a} + (1 - \tau_r)E_{b,atm} \quad (2.13)$$

An internal linearization is required to compensate for possible nonlinear behaviour of the temperature detector, so that the output signal O is:

$$O_{IR,c} = \varepsilon_t \tau_r O_{b,obj} + (1 - \varepsilon_t)\tau_r O_{b,a} + (1 - \tau_r)O_{b,atm} \quad (2.14)$$

If the output signal can be described by *Planck's law*-like function, it is found:

$$O_{IR,c} = \varepsilon_t \tau_r \frac{R}{e^{B/T_{obj}} - F} + (1 - \varepsilon_t)\tau_r \frac{R}{e^{B/T_a} - F} + (1 - \tau_r) \frac{R}{e^{B/T_{atm}} - F} \quad (2.15)$$

The three calibration constants, B , R and F mainly depend on both the nature of the detector and the mean wavelength of the detected band.

The object temperature can be easily evaluated as:

$$T_{obj} = \frac{B}{\ln\left(\frac{\varepsilon_t \tau_r R}{O_{IR,c} - (1 - \varepsilon_t) \tau_r O_{b,a} - (1 - \tau_r) O_{b,atm}} + F\right)} \quad (2.16)$$

Therefore, in order to calculate the object temperature, the ambient environment temperature and the atmospheric temperature (which often coincide) must be measured with external thermometers as also the emissivity coefficient of target, the transmissivity coefficient of the atmosphere and the three constants above described.

When performing measurements at relatively short distances, the terms associated with the atmospheric absorption and emission may be neglected being $\tau_r \approx 1$. Moreover, if a black body is investigated, $\varepsilon_t \approx 1$ and its temperature is given by:

$$T_{obj} = \frac{B}{\ln\left(\frac{R}{O_{IR,c}} + F\right)} \quad (2.17)$$

By changing the black body temperature in the range of interest, it is possible to record the output signal from the IR scanner and then the calibration constants can be evaluated by making a nonlinear best fit of the n_p independent measurement points. In particular, if \widetilde{T}_b is the temperature of the black body measured by means of an accurate thermometer, the calibration constants are calculated by minimizing the functional:

$$\sum_{i=1}^{n_p} (\widetilde{T}_b^i - T_{obj}^i)^2 \quad (2.18)$$

It is advisable to have a temperature calibration range slightly larger than the one of interest for the experiments.

2.2.4. THE HEATED THIN FOIL HEAT FLUX SENSOR

IR Thermography can be applied in thermo-fluid dynamics to measure the *convective heat flux* q_c and/or the *convective heat transfer coefficient* h between a solid surface and a fluid flowing on it. It must be pointed out that herein the heat flux is treated as a scalar quantity as only the component normal to the surface is considered.

The relation between q_c and h is given by:

$$q_c = h(T_w - T_r) \quad (2.19)$$

2.2. INFRARED THERMOGRAPHY

where T_w is the *surface (wall) temperature* and T_r is a *reference temperature* depending on the actual conditions of the fluid flow, in the present experiments the adiabatic wall temperature T_{aw} is employed.

Theoretical and experimental data for convective heat transfer are usually reported in terms of dimensionless numbers. In this thesis, the results will be discussed in terms of the *Nusselt number*, Nu , typically adopted for internal flows:

$$Nu = \frac{hl}{k_f} \quad (2.20)$$

where l is a flow characteristic length and k_f is the fluid thermal conductivity.

To measure q_c or h a *heat transfer sensor* is required. Among the possible solutions, the *heated thin foil heat flux sensor* represents the easiest way to measure them if an IR scanner is used.

As shown in Fig. 2.8, it usually consists of a thin metallic sheet (foil), or a printed circuit board, steadily and uniformly heated by Joule effect. The foil is often thermally isolated at its back surface while its front side is exposed to the fluid stream. In the experiment reported in this thesis, one side is exposed to the flow while the other is imaged by the camera. This is possible if the thermally thin condition is satisfied, i.e. the *Biot number* Bi , ($Bi = hs/k_{foil}$, where s is the foil thickness and k_{foil} is the foil thermal conductivity) is much lower than unity. The emissivity of the side facing the camera is normally significantly increased by coating it with black opaque paint.

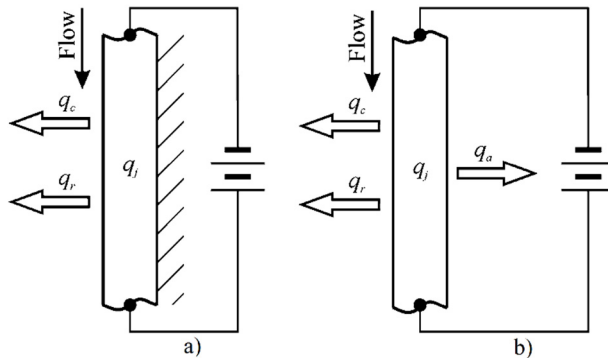


Fig. 2.8 - Sketch of the heated thin foil heat flux sensor: a) adiabatic back surface; b) diabatic back surface (from [55]).

In the case of a thermally thin foil, in steady state condition, an energy balance can be evaluated (see Fig. 2.9) as:

$$q_j = q_c + q_r + q_{nc} + q_{tc} \quad (2.21)$$

where:

- q_j is the flux provided via Joule effect with a stabilised power supply;
- q_c is the convective heat flux expressed by the Eq. (2.19);
- q_r is the radiative flux, made of the radiation towards the impinging flow, which is, however, in the present measurements, negligible since the small plate emissivity in that direction, and of the radiation towards the ambient, which is regulated by the Stefan-Boltzmann's law $q_r = \varepsilon_t \sigma (T_w^4 - T_a^4)$;
- q_{nc} is the natural convection heat flux;
- q_{tc} is the tangential conduction heat flux, that can be estimated as $q_{tc} = -sk_{foil} \nabla^2 T_w$. This term is, in the present measurements, very small with respect to the heat flux provided by Joule effect.

The convective heat transfer coefficient can be easily calculated by combining Eqs. (2.19) and (2.21):

$$h = \frac{q_j - q_r - q_{nc} - q_{tc}}{T_w - T_r} \quad (2.22)$$

Both the heat losses and q_r are correction terms and, in order to obtain accurate data, they must be a small fraction of q_j and accurately measured. T_w is representative of the wall temperature when the heat flux by Joule effect is provided to the plate and the jet is impinging onto it. The reference temperature T_r is the plate adiabatic temperature T_{aw} , i.e. the plate temperature distribution when no electric heating is provided and only the jet is impinging onto it. It represents the temperature distribution for which there is no convective heat transfer between the impinged plate and the surrounding environment.

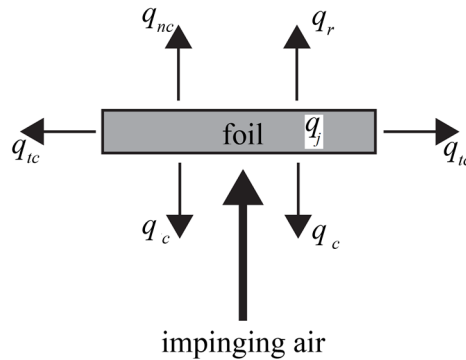


Fig. 2.9 - Schematic of the energy balance through the heated thin foil.

3. EXPERIMENTAL SETUP DETAILS

In this chapter, the experimental rigs used to perform the experiments are described. In §3.1 the grids tested in this thesis are introduced; a brief description of the turbulent continuous jet development is given in §3.2.1. The continuous jet experimental setups, both for flow field and convective heat transfer measurements, are described in §3.2.2. The main aspects of the synthetic jet flow field are drawn in §3.3.1; the characterization of the synthetic jet device and the whole experimental setup used to analyse the effects of the fractal iterations on the synthetic jet flow field are reported in §3.3.2.

3.1. GRIDS DESCRIPTION

Fig. 3.1 shows a sketch of all the single square (SGs) and the fractal-square grids (FGs) which have been tested in this thesis.

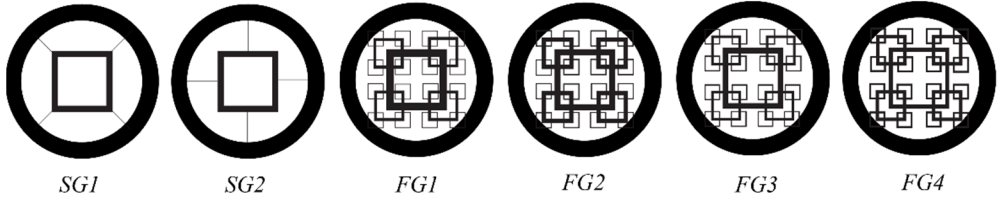


Fig. 3.1 - Sketch of the single square and fractal square grids tested.

#	σ	L_0	t_0	L_r	t_r	x^*/D
<i>SG1</i>	0.11	9.00	1.00	-	-	4.05
<i>SG2</i>	0.11	9.00	1.00	-	-	4.05
<i>FG1</i>	0.32	9.00	1.23	4.00	6.25	3.29
<i>FG2</i>	0.32	9.00	1.00	4.00	4.00	4.05
<i>FG3</i>	0.32	9.00	0.82	4.00	2.77	4.93
<i>FG4</i>	0.32	9.00	0.69	4.00	2.04	5.86

Table 3.1 - Grids' geometrical parameters.

The inserts, made of a 0.5 mm thick stainless-steel foil, are shaped by means of electrical discharge machining. The grid parameters are summarised in Table 3.1 (refer to Fig. 1.3 and Fig. 3.1 for clarity). The FGs are all characterised by the same σ and L_0 and different t_0 . The SGs' blockage ratio is almost one third of the FGs'

3.2. THE CONTINUOUS JET EXPERIMENTS

one, as they have been realised by keeping only the 1st iteration bars and removing the secondary iterations ones. The effects of the holding bars on the flow field developed downstream the *SGs* have also been analysed, since *SG1* and *SG2* only differ for their position.

As a reference, the axisymmetric jet (from now on referred as jet without turbulators, *JWT*) flow field and/or the flow field developing past a regular grid (*RG*, sketched in Fig. 3.2) are analysed.

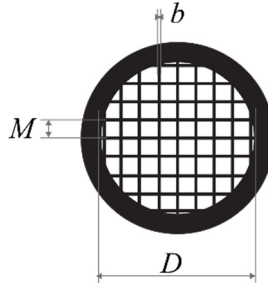


Fig. 3.2 - Sketch of the regular grid.

The *RG*, differently from the others, is shaped by laser cutting a 0.5 mm thick aluminium foil. The grid has been designed following the scaling relations Eqs. (1.3) and (1.4), conveniently modified by substituting T_t with the nozzle section area A_n . The *RG* is realised in order to have the same σ and M_{eff} of the *FG2*:

$$\sigma = \frac{b}{M} \left(2 - \frac{b}{M} \right) \quad (3.1)$$

$$M_{eff} = \frac{4A_n^2}{P} \sqrt{1 - \sigma} \quad (3.2)$$

The resulting bars' thickness b and meshlength M are 0.4 mm and 2.4 mm, respectively.

3.2. THE CONTINUOUS JET EXPERIMENTS

3.2.1. TURBULENT CONTINUOUS JETS

A jet is a flow whose main source of kinetic energy and momentum flux is a pressure-drop across an orifice [66]. In case the jet spreads through a medium at rest is it referred to as *submerged* jet. Moreover, if a constant pressure-drop is provided and no other accelerating or decelerating forces act on the jet, the momentum flux in

the jet's cross-section remains constant as it moves downstream. In this case, the jet is defined continuous¹ and its main turbulent statistics are not time-dependent.

In the following, a brief description of a submerged axisymmetric continuous jet, having a constant momentum flux, is given. A full discussion of the flow field characteristics and of the convective heat transfer generated by impinging jets is reported in the review articles [67, 68, 69].

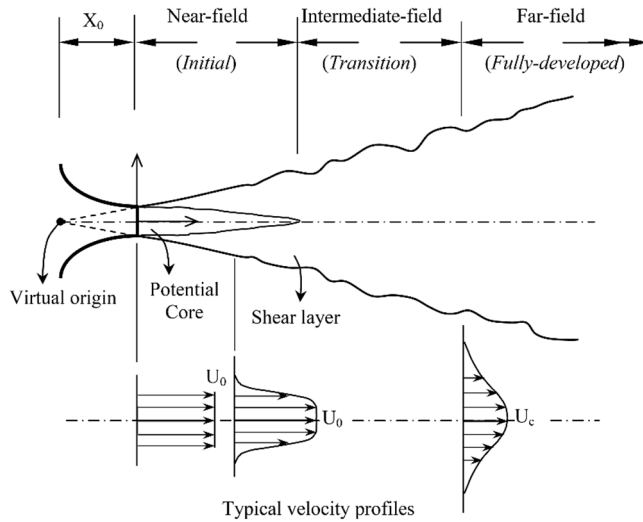


Fig. 3.3 - Sketch of turbulent continuous jet.

The jet flow field can be mainly subdivided in three different regions (Fig. 3.3):

- the near-field region, usually found within $0 \leq x/D \leq 6$ (depending on the initial conditions), is a region of flow establishment in which the jet flow features meet those of the surrounding mixing zone, causing the development of turbulence. The mean velocity profile at the exit is determined by the device geometry, i.e. streamlined nozzle, pipe, sharp-edged orifice, etc. In this region, the presence of a potential-core (that is defined as the region in which the centreline velocity remains essentially constant and equal to the centreline velocity at the nozzle exit [70]) can be detected.
- the transition region, where the highly anisotropic turbulent structures due to Kelvin-Helmholtz instabilities generated at the jet boundaries within the first few diameters from the nozzle, evolve and interact and the velocity profile approaches a gaussian shape.

¹ Here, the term continuous does not refer to the *continuum* hypothesis which is intrinsically considered valid.

3.2. THE CONTINUOUS JET EXPERIMENTS

- the far-field region, is a fully-developed or self-similar region where the description of the flow statistics can be given by only knowing a velocity and a length scale.

Due to the momentum flux constancy, “*the velocity profile becomes “lower” and “wider” with increasing distance from the beginning of the jet [71]*”. In particular, in the self-similar region and according to the classical turbulence scaling [72], the centreline axial velocity and the jet width respectively decreases and increases linearly (with a spreading rate between 0.07 and 0.1 [73]). However, it must be pointed out that, depending on the inlet conditions, the jet spreading may occur few diameters apart from the jet source, as for example for short-pipe nozzle where the jet width remains constant up to 2 diameters and then starts to spread.

While the momentum flux is constant, the mass flow rate increases as the longitudinal distance increases. Indeed, as the fluid issues through the nozzle, the surrounding air is entrained into the jet itself because of the velocity imbalance between the jet core and the quiescent fluid, triggering shear layer instabilities, also known as Kelvin-Helmholtz instabilities. The downstream evolution of these instabilities plays a key-role in the jet transition from the laminar to the turbulent regime and, therefore, in the jet entrainment. Their amplification can cause the generation of vortex rings embracing the jet core that keep their axial symmetry for few diameters before pairing and breaking down because of the insurgence of secondary circumferential instabilities [74]. Moreover, in some cases, also helical waves can appear and grow up, generating helical vortices [75, 76]. Fig. 3.4 shows the three preferred modes describing the axisymmetric jet flow instabilities. Moreover, a sketch of the jet transition is reported in Fig. 3.5.

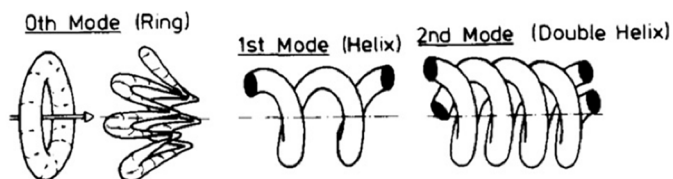


Fig. 3.4 - Dominant vertical and helical modes in axisymmetric jet flow (from [76]).

Liepmann and Gharib [77] showed that the entrainment is primarily due to the streamwise vortical structures instead of the toroidal ones since the latter ones lose strength and coherence beyond the potential-core region. Considering that the entrainment rate is directly related to the jet scalar transfer and mixing, several

3. EXPERIMENTAL SETUP DETAILS

attempts have been made to increase the streamwise vorticity production, as for example by means of non-circular pipes or grids located at the nozzle-exit.

By applying the *Buckingham Π theorem*, it results that only one dimensionless parameter, the Reynolds number Re , is needed to establish if the flow is laminar or turbulent. It measures the ratio between the viscous and the inertial forces and is given by:

$$Re = \frac{U_b D}{\nu} \quad (3.3)$$

where U_b is the bulk velocity evaluated over the jet cross-section, ν is the fluid kinematic viscosity and D is the nozzle/orifice diameter.

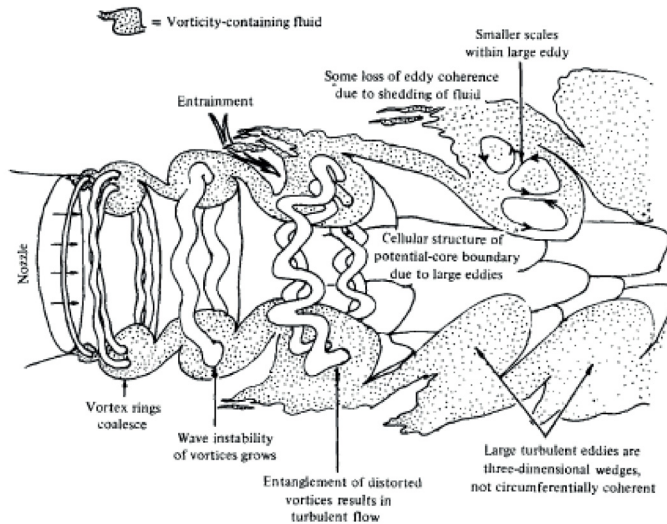


Fig. 3.5 - Representation of a transitional jet near the nozzle exit section (from [74]).

3.2.2. THE CONTINUOUS JET EXPERIMENTAL RIGS

A sketch of the feeding system is reported in Fig. 3.6. Air is collected from the environment with a centrifugal blower. An inverter is used to regulate the input shaft power. The fluid is, then, seeded with olive oil particles (used as tracers) generated by means of a Laskin nozzle [53]. The flow rate is measured through a rotameter while a radiator is used to control the fluid temperature. Finally, the fluid is conveyed within a plenum chamber (whose internal diameter and length are, respectively, equal to $3D$ and $20D$, being $D = 20\text{ mm}$ the nozzle diameter) located upstream of a short-pipe nozzle which is $6.2D$ long. Inside the chamber two honeycombs are

3.2. THE CONTINUOUS JET EXPERIMENTS

located to reduce the turbulence intensity due to the large flow structures that may generate within the feeding circuit. Finally, a contoured entrance is used to carry the flow through the short-pipe nozzle and a terminating cap is eventually used to locate the grid at the nozzle exit section.

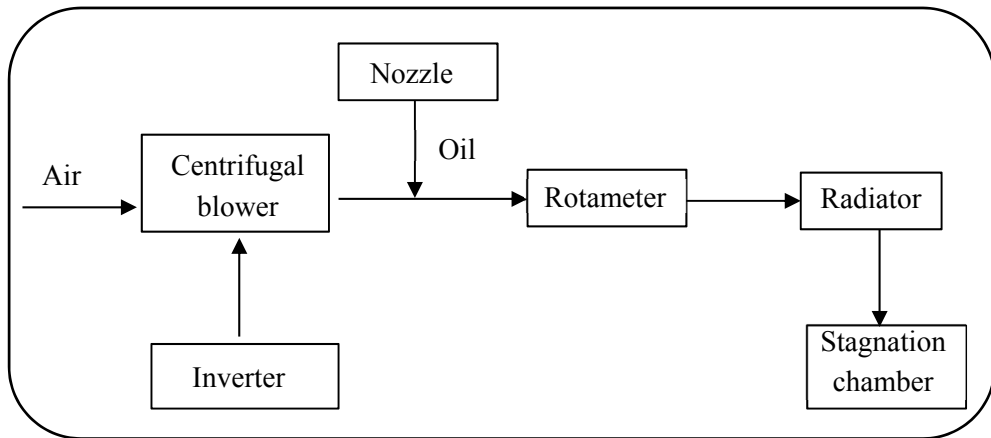


Fig. 3.6 - Schematic of the feeding circuit of the continuous jet experimental apparatus.

Two different experiments aiming to analyse the effects of the secondary iterations of fractal turbulators on the flow field of continuous turbulent jets have been carried out. In particular, the former, from now on referred to as the CJ/A experiment, has been carried out at fixed Re equal to 6,700. In this case, only the *SG1* and the *FG2* have been compared to the *JWT*, with the purpose to assess the effects of the introduction of the secondary iterations bars. In the latter, that will be referred to as CJ/B experiment, all the grids reported in Table 3.1 are compared both to the *JWT* and the *RG*, for a fixed Re equal to 16,000, to analyse the effects of different secondary iterations bars thickness.

Moreover, the effects of the fractal geometry on the convective heat transfer properties of impinging axisymmetric continuous jets have been experimentally analysed by means of the steady-state heated-thin foil technique introduced in §2.2.4.

A schematic representation of the imaging system and of the measurement domain used in the CJ/A experiment (which results are reported in Chapter 4) is reported in Fig. 3.7. 6,000 PIV instantaneous velocity fields have been evaluated, to ensure the convergence of the turbulence statistics. The acquisition system is formed by two Andor Zyla sCMOS 5.5 *Mpixels* cameras, of which one has a large field of view (LFV) while the other camera has a small field of view (SFV), contained within the largest. The SFV camera, equipped with a 100 *mm* Vivitar macro-objective ($f_{\#}16$),

3. EXPERIMENTAL SETUP DETAILS

images a $2.5D \times 2D$ wide region, with the starting point located at $0.15D$ from the nozzle exit section and a resolution of 48 pixels/mm . The LFV camera, equipped with a 50 mm Nikon macro-objective ($f_{\#}11$), images a $12.5D \times 5D$ wide area, with the starting point located at $0.2D$ from the nozzle exit section and a resolution of 10 pixels/mm . A Quantel Evergreen laser for PIV applications (532 nm wavelength, 200 mJ/pulse , $< 10 \text{ ns}$ pulse duration), with an exit beam diameter of about 5 mm , is used to illuminate the measurement domain. The laser beam is then enlarged by a bi-concave lens (with -75 mm focal length) and adjusted in thickness by a second bi-convex lens (with 200 mm positive focal length). Finally, a cylindrical lens (with 75 mm focal length) is used to enlarge the laser along the plane containing the jet axis and orthogonal to the optical axis of the camera. The laser repetition frequency f_l is equal to 15 Hz .

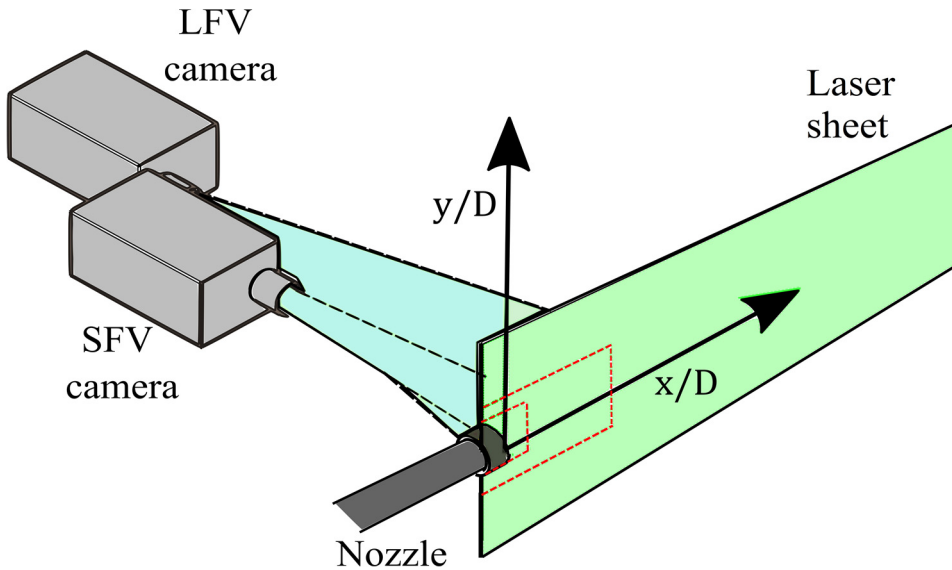


Fig. 3.7 - Schematic representation of the imaging system and of the measurement domain (CJ/A and synthetic jets' experiments).

A temporal minimum image subtraction is applied to the raw images in order to limit the effect of laser reflections within the flow field. A home-made software, based on the works by Astarita [78, 61, 62, 79], is used to perform the images cross-correlation operation. Different processing parameters have been used for each camera because of the different resolutions and illumination levels: a final interrogation window size of $48 \times 48 \text{ pixels}$, with 87.5% of overlap, is used to process the images acquired by using the SFV camera while for the LFV camera the

3.2. THE CONTINUOUS JET EXPERIMENTS

final interrogation window size is 16×16 pixels, with 75% of overlap. The resulting vector pitches are about 0.125 mm and 0.4 mm, respectively.

A sketch of the CJ/B experiments setup is shown in Fig. 3.8. The same laser source described above has been used also for the CJ/B experiment. The laser beam is initially enlarged by means of a bi-convex spherical lens (with -25 mm focal length) and then adjusted by a bi-concave spherical lens (with 75 mm focal length). A 90-degree rotation of the beam is, then, provided by a mirror. Finally, a second bi-convex spherical lens (with 300 mm focal length) and a cylindrical lens (with -50 mm focal length) are used to obtain the laser sheet. f_l is equal to 15 Hz. Four Andor Zyla sCMOS 5.5 Mpixels cameras, equipped with 100 mm Tokina macro-objectives ($f_{\#}16$), are used to image an overall area of $8D \times 1.5D$ wide area, with the starting point located at the nozzle exit section. In order to maximize the spatial resolution, obtaining about 60 pixels/mm, the four cameras have been set alternatively on both side of the laser sheet, with a sufficient number of overlapping pixels to perform a reliable stitching of the images. A temporal minimum image subtraction is applied to them. The instantaneous flow fields are evaluated by means of the home-made software introduced above. Final interrogation windows of 24×24 pixels are cross-correlated, resulting in a vector pitch of about 0.1 mm.

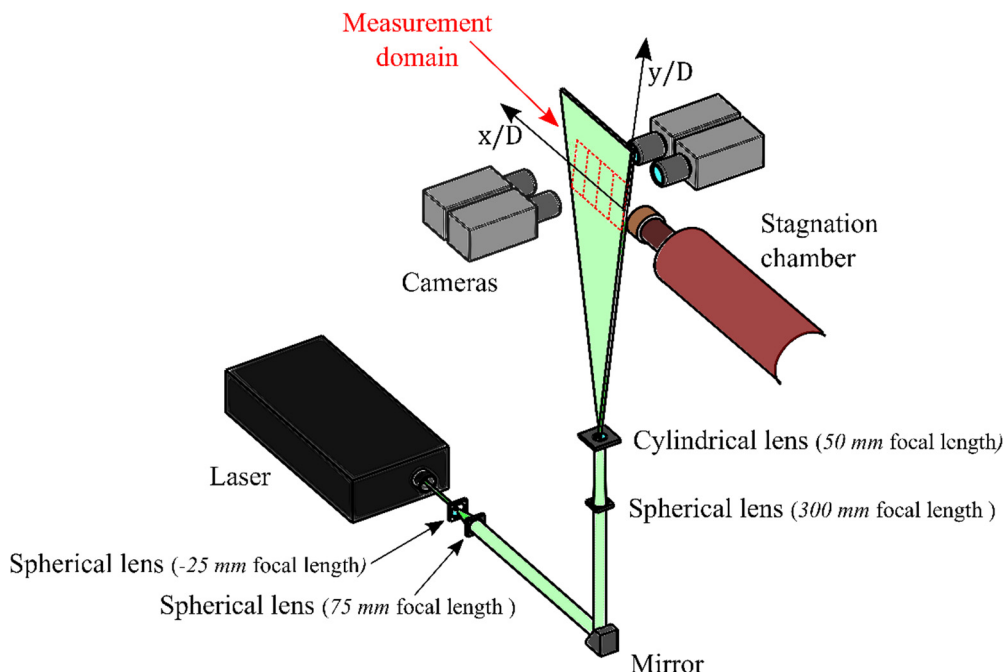


Fig. 3.8 - Sketch of the CJ/B experimental setup.

3. EXPERIMENTAL SETUP DETAILS

For both the CJ/A and CJ/B experiments, the origin of the reference system corresponds to the centre of the round nozzle exit section. The x -axis is aligned with the jet centreline while y is perpendicular to x , in the vertical direction. Concerning the FGs and the SGs , all the grids are analysed both along the xy plane (whose results will be denoted by -0) and the plane rotated of 45° with respect to it (whose results will be denoted by -45).

The experimental apparatus used to perform the convective heat transfer measurements is sketched in Fig. 3.9. The feeding circuit (centrifugal blower, inverter, rotameter, radiator, plenum chamber and nozzle) corresponds to the CJ/A and CJ/B one except for the Laskin nozzle as no tracer particles are required in this case. The plenum chamber together with the nozzle are arranged on a linear slide, which ensures the movement of the nozzle along its own axis with accuracy of 0.1 mm . The air impinges normally onto a thin constantan foil (450 mm long, 200 mm wide, $50\text{ }\mu\text{m}$ thick), whose flatness is ensured using a stiffening frame. Both sides of the foil are connected to an external stabilized power supply.

The sensitive area of the thin foil is imaged using a CEDIP Jade III MW-IR camera with a digital resolution of about 1.5 pixels/mm . The camera is located on the opposite side with respect to the impinging air, as the constantan foil is characterised by $Bi \ll 1$. This also allows to neglect the temperature gradients across it. The back side of the foil (i.e. the one facing the IR camera) is painted in black with a high emissivity material ($\varepsilon_t = 0.95$), such that the infrared emission of the plate is maximized obtaining a higher signal to noise ratio.

All the grids described in Table 3.1 have been tested. Each measurement has been performed under the same power input (following [1], where the RG and the FG2 have been compared), i.e. the same product of the volumetric flow rate \dot{m}/A_n times the pressure-drop Δp_0 (measured by means of the manometer sketched in Fig. 3.9). The evaluated effective Re values, for each grid, are reported in Table 3.2.

Also in this case, the origin of the reference system corresponds to the centre of the round nozzle exit section; the x -axis is aligned with the jet centreline.

As already said, Eq.(2.22) is used to evaluate h . For each grid, the wall temperature T_w is obtained by measuring the temperature distribution of the foil heated by Joule effect impinged by the incoming fluid at 13 different nozzle-to-plate distances equally spaced between $x/D = 1$ and $x/D = 7$. The adiabatic wall temperature T_{aw} is instead obtained without considering any other heating source than the one associated with the incoming flow. The T_{aw} is, on account of the very small Mach number, almost coincident with the ambient temperature (and jet static temperature) and, therefore, reasonably independent of the nozzle to plate distance. Thus, for simplicity, it is measured only at the beginning and at the end of each test

3.2. THE CONTINUOUS JET EXPERIMENTS

(namely $x/D = 1, 7$). For all the other x/D values, the measured adiabatic wall temperature is corrected with the difference between the ambient temperature at the current stage and the one measured along with the adiabatic wall temperature.

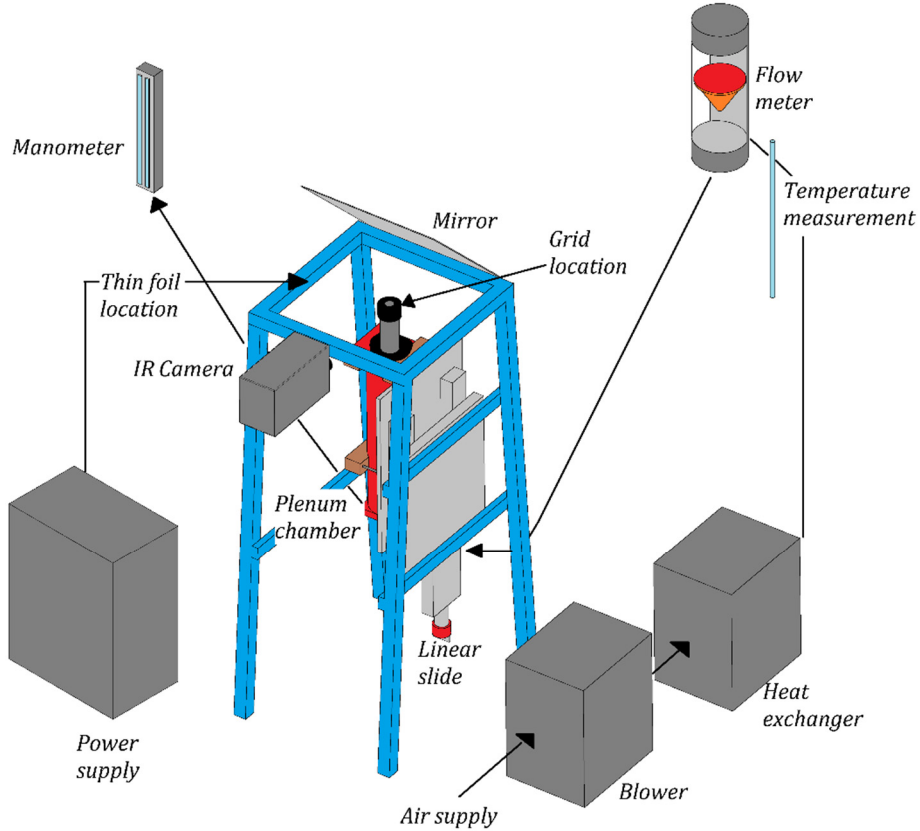


Fig. 3.9 - Schematic of the heat transfer measurements setup (only the position of the constantan foil is reported).

#	Re	$\dot{m}(g/s)$	$\Delta p_0 (Pa)$
FG1 ÷ FG4	15,000	5.1	320
SG1 ÷ SG2	18,800	6.2	260

Table 3.2 - Heat transfer measurements experimental conditions.

For each nozzle-to-plate distance 1,000 images are collected at a frame rate of 100 Hz. The temporal separation between subsequent frames (10 ms) is sufficiently large to consider the samples as statistically independent. In fact, performing a conservative estimate of the integral timescale considering as reference speed $U_b =$

14 m/s and length to nozzle diameter D , one would get a timescale of about 1.4 ms, thus reasonably below the observation time.

The convective heat transfer coefficient values are presented in non-dimensional form in terms of the Nusselt number spatial distribution, Nu .

An uncertainty analysis of the values calculated using Eq. (2.22) is carried out as suggested by Moffat [80]. Each one of the terms involved in the equation are perturbed and its effect on the convective heat transfer coefficient values is reported in Table 3.3. The resulting measurement uncertainty is $\pm 5.2\%$ (with 95% confidence level) and it is taken as the cut-off value to consider reliable an experiment when repeating it.

	<i>Typical value</i>	<i>Uncertainty</i>	$\left(\frac{\partial R_i}{\partial X_i} \frac{\partial X_i}{\partial Nu}\right) \cdot 100$
T_w	310 K	0.2 K	2.8
T_{aw}	293 K	0.2 K	2.7
T_a	293 K	0.1 K	1.05
J	90 A	1 % of reading	1.1
\mathcal{V}	1.9 V	1% of reading	1.1
ε_t	0.95	0.01	0.03
D	0.02 m	1 %	0.02
s	50 μm	1 %	10^{-5}
q_{nc}	210 W/m ²	20 %	2.8
<i>Total uncertainty</i>			$\pm 5.2\%$

Table 3.3 - Uncertainty analysis.

3.3. THE SYNTHETIC JET EXPERIMENTS

3.3.1. SYNTHETIC JETS

Synthetic jets are zero-net mass flux (ZNMF) jets consisting of train of vortices produced by the periodic ingestions and ejections of fluid across an orifice or a nozzle. The flow is driven by the periodic pressure variations generated inside a cavity by means of a movable diaphragm, usually represented by a piezoelectric, an electromagnetic, an acoustic or a mechanical driver.

A schematic of a typical synthetic jet actuator is shown in Fig. 3.10: as the fluid comes out from the cavity, separations can occur at the sharp edges of the orifice generating a vortex sheet that can roll into an isolated vortex ring. If the impulse

3.3. THE SYNTHETIC JET EXPERIMENTS

given to it is large enough to overcome the forces associated with the (reversed) suction flow, the vortex ring can be conveyed away from the actuator under its own self-induced velocity, establishing the flow.

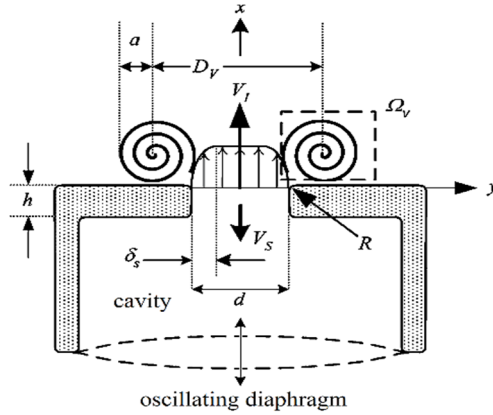


Fig. 3.10 - Schematic of a typical synthetic jet actuator ([81]).

Although they conserve the mass, because of the inherent asymmetry of the flow conditions across the jet orifice (actuator cavity on one side and ambient fluid on the other), synthetic jets are capable to transfer positive net momentum to the external fluid without *ab extra* piping. This unique feature of synthetic jets makes them very useful for many practical applications, above all if size, weight, and power are constrained.

The evolution of a synthetic jet can be divided in two distinct domains:

- a near field, in which the flow is mainly dominated by the formation and development of the vortex ring that, ultimately, undergoes transition to turbulence and slows down, losing its coherence;
- a far field, in which a fully-developed turbulent jet, similar in some respects to a conventional continuous jet, is established [82].

For a given geometry, two dimensionless parameters have been identified to characterise the synthetic jet flow field: the Reynolds number, Re_{sj} , and the Strouhal number, St , respectively equal to:

$$Re_{sj} = \frac{U_0 D}{\nu} \quad (3.4)$$

$$St = \frac{f D}{U_0} = D / \mathcal{L}_0 \quad (3.5)$$

3. EXPERIMENTAL SETUP DETAILS

where f is the actuation frequency, \mathcal{L}_0 is the stroke length (which, according to the slug model proposed in [82], represents the length of the fluid column expelled during the ejection part of the period) and U_0 is a characteristic velocity, here evaluated following Smith and Glezer [82] as the mean velocity over the ejection half of the actuation period τ divided by the whole period :

$$U_0 = \frac{1}{\tau} \int_0^{\tau/2} U_A(t) dt \quad (3.6)$$

where U_A is the centreline velocity at the orifice exit plane (see Fig. 3.11).

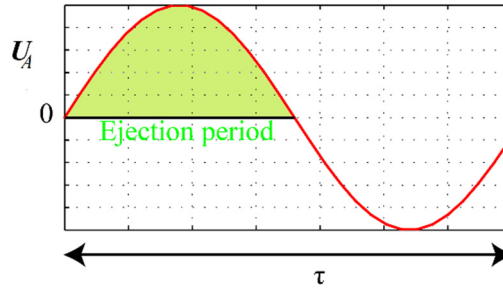


Fig. 3.11 - Schematic of U_0 , as reported in Eq. (3.6).

Shuster and Smith [83] have shown that the Reynolds number affects the coherence and the stability of the vortex once formed, but there is no available evidence to suggest that it has a dominant role in the formation and the advection of the vortex ring. In contrast, it has been established that the Strouhal number, and therefore the stroke length, plays a key role in the jet formation and significantly affects the flow field characteristics [81, 84].

Holman et al. [81] proposed a synthetic jet formation criterion which slightly takes into account the orifice geometry:

$$\frac{1}{St} > \frac{32c^2(1+e)^p}{\mathbb{k}\pi^2} \quad (3.7)$$

where $c = U_b/U_A$, e is the dimensionless exit radius of curvature, the exponent $p < 1$ accounts grossly for flow separation caused by the exit curvature and \mathbb{k} is a constant depending on the ratio of the vortex core radius to the vortex diameter (Fig. 3.10).

Experimental measurements carried out by means of both high-speed PIV and hot-wire anemometry on an axisymmetric impinging synthetic jet, at $Re_{sj} = 1500$, $3 \leq \mathcal{L}_0/D \leq 32$ and for orifice-to-plate distances $2 \leq x/D \leq 12$, are described in [85]. No effects due to the plate presence were observed for $x/D \geq 4$ and the authors

3.3. THE SYNTHETIC JET EXPERIMENTS

identified four different flow field regimes (summarised and sketched in Table 3.4 and Fig. 3.12, respectively): for $3 \leq \mathcal{L}_0/D < 4$ a vortex ring immediately in front of the orifice is formed during the ejection phase, whose strength increases as \mathcal{L}_0/D increases up to reach its maximum at $\mathcal{L}_0/D \cong 4$ (according to the results reported in [86] for impulsively started jets). For $4 \leq \mathcal{L}_0/D \leq 8$ a trailing jet is formed after the vortex is detached from the orifice with the peak velocity located at the interface between them: the faster fluid widens the vortex core eventually leaving a weakened lower velocity trailing jet. For $8 \leq \mathcal{L}_0/D \leq 16$ the vortex formation occupies only a small fraction of the ejection phase compared with the entire quantity of fluid that forms the trailing jet; the peak velocity occurs after the vortex is detached, so that the faster trailing jet catches up on the vortex, causing, on one side, an increase of the vortex circulation which results in a wider vortex ring diameter and, on the other side, a destabilization of the vortex itself. For $\mathcal{L}_0/D \geq 16$ this effect is even more pronounced, resulting in the complete vortex disintegration by a highly turbulent trailing jet.

<i>Regime</i>	<i>Stroke length threshold</i>	<i>Description</i>
	$\mathcal{L}_0 \leq \mathcal{L}_0^{(f)} = 2D$	<i>No jet formed below the formation threshold stroke length.</i>
<i>(a)</i>	$\mathcal{L}_0^{(f)}/D \leq \mathcal{L}_0/D \leq 4$	<i>Monotonous increase in vortex strength with stroke length up to a maximum at $\mathcal{L}_0/D = 4$.</i>
<i>(b)</i>	$4 \leq \mathcal{L}_0/D \leq 8$	<i>Additional ejected fluid (beyond $\mathcal{L}_0/D = 4$) forms a trailing jet following the vortex, resulting in a wider vortex core.</i>
<i>(c)</i>	$8 \leq \mathcal{L}_0/D \leq 16$	<i>Maximum ejection velocity occurs in the trailing jet, which destabilises the preceding vortex and results in increased flow mixing.</i>
<i>(d)</i>	$\mathcal{L}_0/D \geq 16$	<i>The flow is dominated by the trailing jet which overtakes the vortex, resulting in a highly turbulent intermittent jet flow.</i>

Table 3.4 - Free synthetic jet flow morphology regimes as function of the stroke length (adapted from [85]).

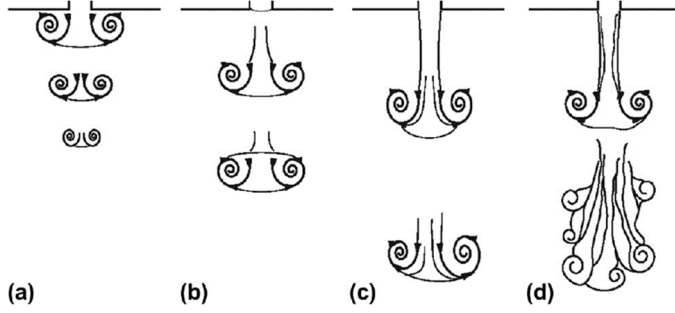


Fig. 3.12 - Flow morphology of vortex formation and evolution at various stroke lengths: a) $L_0/D \leq 4$; b) $4 \leq L_0/D \leq 8$; c) $8 \leq L_0/D \leq 16$; d) $L_0/D \geq 16$ (adapted from [85]).

3.3.2. THE SYNTHETIC JET EXPERIMENTAL APPARATUS

A schematic of the synthetic jet device is reported in Fig. 3.13: a HERTZ DS250.3 loudspeaker is installed to the rear side of a 5 dm^3 in volume wooden box, while a nozzle, of length $L_{sj} = 210 \text{ mm}$ and inner diameter $D = 20 \text{ mm}$, is attached to its front side. A signal generator (DIGILENT Analog DiscoveryTM) is used to supply, with a sinusoidal input, the loudspeaker. The cavity coupled with the pipe acts as a driven Helmholtz resonator [87] having a frequency $f_H \cong 28.7 \text{ Hz}$, evaluated following the classical formula:

$$f_H = \frac{a}{2\pi} \sqrt{\frac{\pi D^2 / 4}{V_c \cdot L'_{sj}}} \quad (3.8)$$

where a is the air speed of sound, V_c is the cavity volume and $L'_{sj} = L_{sj} + 2D\beta'$ is an equivalent nozzle length that takes into account the end corrections by means of β' (an added mass coefficient that has been set equal to 0.307 following [88]). The nominal loudspeaker resonance frequency and diameter are $f_L = 36 \text{ Hz}$ and $D_L = 250 \text{ mm}$.

Both the gas dynamics (Helmholtz resonance) and the mechanical dynamics of the loudspeaker influence the overall device dynamics, resulting in a two degrees of freedom mass-spring-damper system [87, 89]. The two resonance frequencies have been experimentally evaluated, for all the device configurations, by measuring the device impedance Z reported in Fig. 3.14, finding $f_1 = 8.8 \text{ Hz}$ and $f_2 = 88.7 \text{ Hz}$.

$$Z = \frac{\mathcal{V}}{\mathcal{I}} = \frac{|\mathcal{V}|}{|\mathcal{I}|} e^{j(\theta_v - \theta_j)} = \frac{|\mathcal{V}|}{|\mathcal{I}|} e^{j\Delta\theta} \quad (3.9)$$

where \mathcal{V} and \mathcal{I} are, respectively, the voltage and the current intensity supplied to the loudspeaker.

3.3. THE SYNTHETIC JET EXPERIMENTS

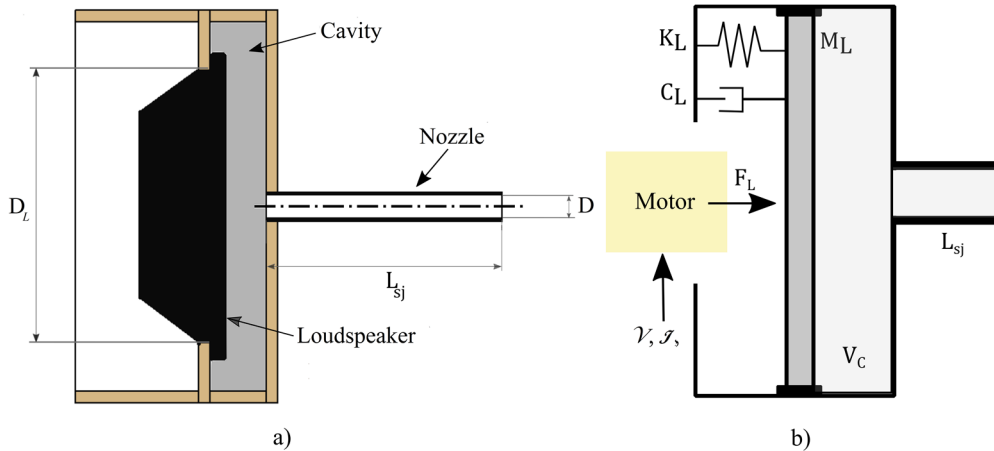


Fig. 3.13 - Schematic representation of the synthetic jet device.

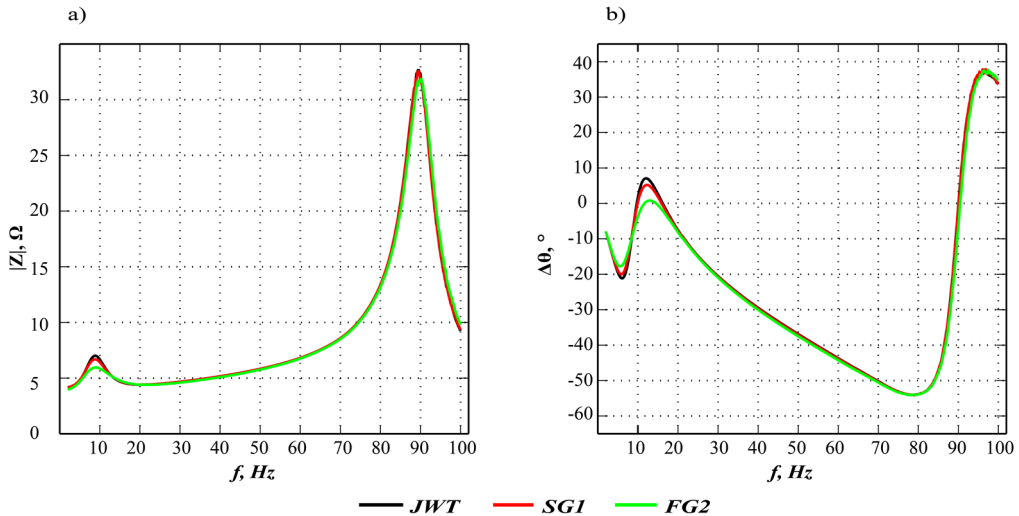


Fig. 3.14 - Device impedance versus input frequency for all the device configurations.

Fig. 3.14 points out that significant changes in the device response due to a different exit section geometry, and therefore to a different nozzle damping, are only visible close to resonance frequencies, above all near the modified Helmholtz one, according to [87].

A schematic of the whole synthetic jet generating system is reported in Fig. 3.15. A signal generator connected to the computer is used to produce a sinusoidal signal that, opportunely amplified, is supplied to the loudspeaker. Oil tracing particles, produced by a Laskin nozzle, are collected within a temperature-conditioned air volume so that the synthetic jet device injects and ejects the mixed fluid.

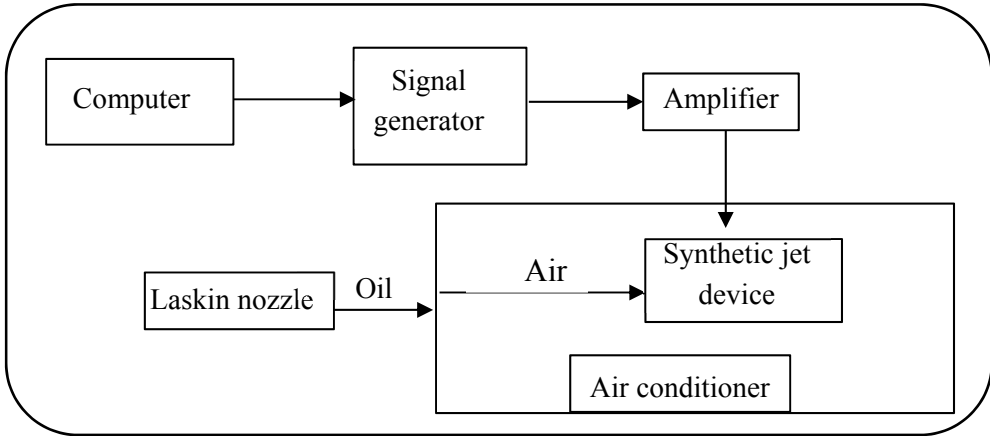


Fig. 3.15 - Schematic of the synthetic jet experimental apparatus.

The instantaneous flow fields have been analysed by means of PIV, adopting the same laser, cameras and optical lenses setup arranged for the CJ/A experiment and described in 3.2.2 (see also Fig. 3.7). However, in order to perform phase-averaged flow field measurements, the same signal generator used to trigger the loudspeaker, is also used to trigger the laser and the cameras. Three different actuation frequencies f have been analysed, respectively equal to 5 Hz, 13 Hz and 35 Hz. For each phase, 200 instantaneous flow fields have been evaluated.

In order to perform a comparison between the synthetic and the continuous jet flow fields, following [90], the device input voltage has been opportunely chosen depending on f , to have $Re_{sj} = Re = 6700$ (referred to the *JWT*). The resulting \mathcal{L}_0/D values are, respectively, 50.0, 19.2 and 7.1.

Only the effects due to the introduction of the *SG1* and of the *FG2*, at the exit section of the synthetic jet device, have been analysed. For fixed f , tests have been conducted by supplying almost the same active power developed to the synthetic jet device, as reported in Table 3.5. The coordinate system coincides with the one introduced for the CJ/A experiments. Moreover, even in this case, the effects due to the grid's introduction have been analysed both along the 0° and the 45° direction.

P_{rms}	5 Hz	13 Hz	35 Hz
JWT	2.44 W	1.37 W	18.83 W
SG1	2.41 W	1.36 W	18.83 W
FG2	2.45 W	1.39 W	18.79 W

Table 3.5 - Active power developed in the synthetic jet device for the *JWT*, the *SG1* and the *FG2* configuration.

3.3. THE SYNTHETIC JET EXPERIMENTS

A temporal minimum image subtraction is applied to the raw images; the same home-made software introduced in 3.2.2 has also been used to evaluate the *6,000* instantaneous flow fields. As for the *CJA* experiment, a final interrogation window size of 48×48 *pixels*, with 87.5% of overlap, is used to cross-correlate the images acquired by using the SFV camera, with a resulting vector pitch of 0.125 *mm*. A final interrogation of 16×16 *pixels*, with 75% of overlap, is instead used to process the images acquired by the LFV camera, with a resulting vector pitch of 0.4 *mm*.

4. THE EFFECTS OF THE SECONDARY ITERATIONS BARS ON CONTINUOUS TURBULENT JETS

In this chapter, the effects of the secondary iterations bars of square fractal grids on the continuous jet flow fields have been investigated. Either a single square grid or a 3-iterations square fractal grid is inserted at the exit section of a short pipe nozzle; the resulting flow field is analysed by means of 2D2C-PIV realizations at a fixed Reynolds number Re equal to 6,700. Results are compared to those related to the widely studied axisymmetric turbulent jet. In order to extract more information on the wakes developed past the bars and to their interaction with the external shear layer, the Proper Orthogonal Decomposition is also applied to small regions past the grids.

4.1. MAIN FLOW FEATURES

6,000 instantaneous 2D-velocity flow fields, for both the *SF1* and the *FG2*, have been analysed both along the 0° and the 45° directions, as sketched in Fig. 4.1.

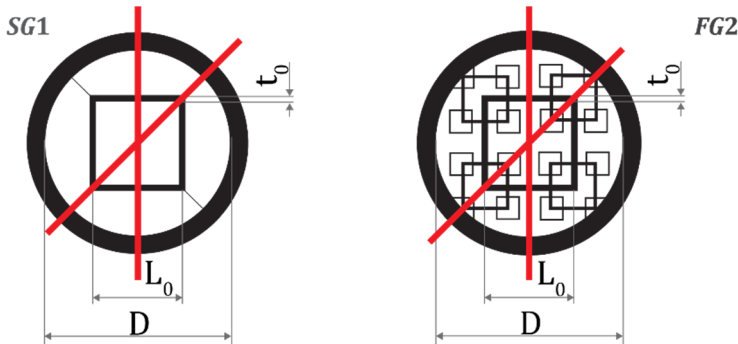


Fig. 4.1- Sketch of the tested grids; the measurement planes are indicated in red.

The results are analysed by means of the well-known Reynolds decomposition:

$$U_j(\underline{x}, t) = \bar{U}_j(\underline{x}) + u_j(\underline{x}, t) \quad (4.1)$$

where $U_1 = U$, $U_2 = V$ are the axial and radial instantaneous velocity components and $\underline{x} = (x, y)$. \bar{U}_j is the j^{th} time-averaged velocity component, and u_j is the j^{th} component of the velocity fluctuations.

4.1. MAIN FLOW FEATURES

In this paragraph, all the velocity components are normalised using the bulk velocity $U_b = 5.0 \text{ m/s}$. Moreover, due to the symmetry of the analysed flow fields with respect to the x -axis, their statistics are evaluated by averaging the $y < 0$ and the $y > 0$ velocity values in order to reduce the measurement noise.

The normalised time-averaged axial velocity contour maps, of both the LFV and SFV cameras, are reported in Fig. 4.2. The mean axial velocity profiles evaluated with the SFV camera at x/D equal to 0.15, 0.5, 1 and 2, respectively, are reported in Fig. 4.3.

According to the literature ([2, 74, 76] among the others; see also §3.2.1 for a brief description) the round jet, coming out from the nozzle, shows a nearly top-hat velocity profile and an initial region, in which the flow is still developing, which extends up to $2D$. With increasing the axial distance, the flow instabilities grow, the shear layer widens and the jet spreads radially.

As the grids are inserted, the flow field close to the nozzle exit section strongly changes. Both the $SG1-0$ and the $SG1-45$ axial velocity maps are characterised by three regions of maxima (related to the A_{SG} and B_{SG} regions sketched in Fig. 4.4) and by two recirculation areas due to the grid's bars. In the $SG1-0$ map the external accelerated regions move away from the jet axis as x increases, with the three-peaks profile disappearing at x/D equal about to 1.7 (see also Fig. 4.3). On the other hand, in the $SG1-45$ map they move towards the jet axis with the velocity profile approaching a bell-shape at about $1.5D$ from the nozzle exit section. This different jet evolution along the square's side and diagonal direction that, in the 3D space, corresponds to a cross shaped jet, was already observed by [37] for single square grids and, more pronounced, by [37, 1, 2] for fractal grids.

The $FG2-0$ and the $FG2-45$ axial velocity maps are, instead, quite different close to the grid because of the mesh imprint. The $FG2-0$ and the $SG1-0$ sections are equal (see Fig. 4.4), hence the same accelerated and decelerated regions previously described are present, as also reported in [29, 2]. However, due to the higher blockage ratio imposed by the $FG2$, larger velocity values are measured. The recirculation regions past the 1st iteration bars are, moreover, considerably wider: their width suddenly increase from about x/D equal to 0.15 up to 0.5 (as also visible by looking at the axial velocity profiles reported in Fig. 4.3 for $x/D = 0.15$ and 0.50). This feature must be addressed to the out-of-plane 2nd and the 3rd iteration bars, as already observed in [29]. Referring to the $FG2-45$ configuration, in Fig. 4.2, five regions of high axial velocity can be detected close to the grid. As for the $SG1-45$ map, the outer ones are sucked towards the jet axis while moving downstream, before disappearing.

4. THE EFFECTS OF THE SECONDARY ITERATIONS BARS ON CONTINUOUS TURBULENT JETS

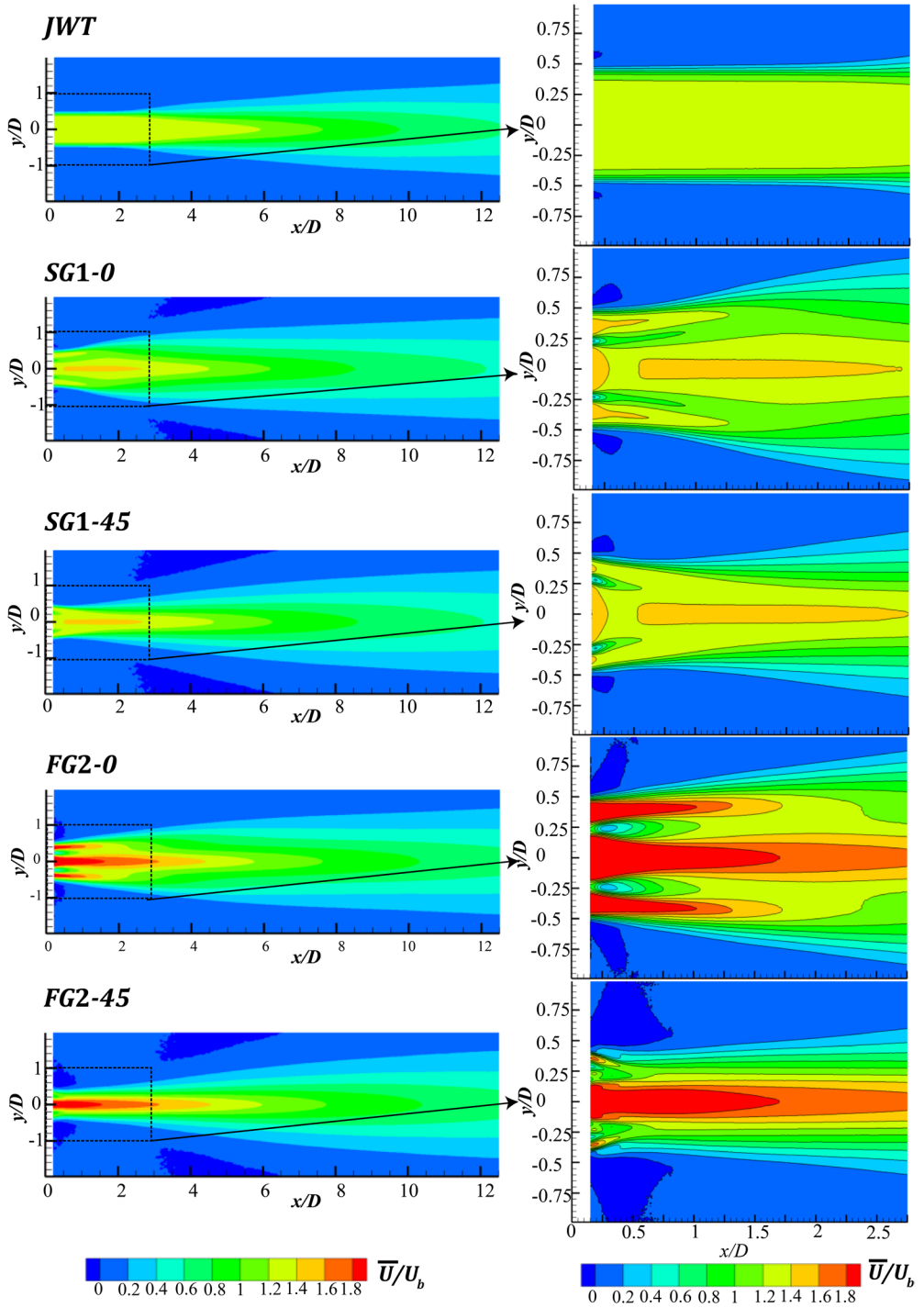


Fig. 4.2 - Time-averaged axial velocity component maps (left: LFV camera / right: SFV camera).

4.1. MAIN FLOW FEATURES

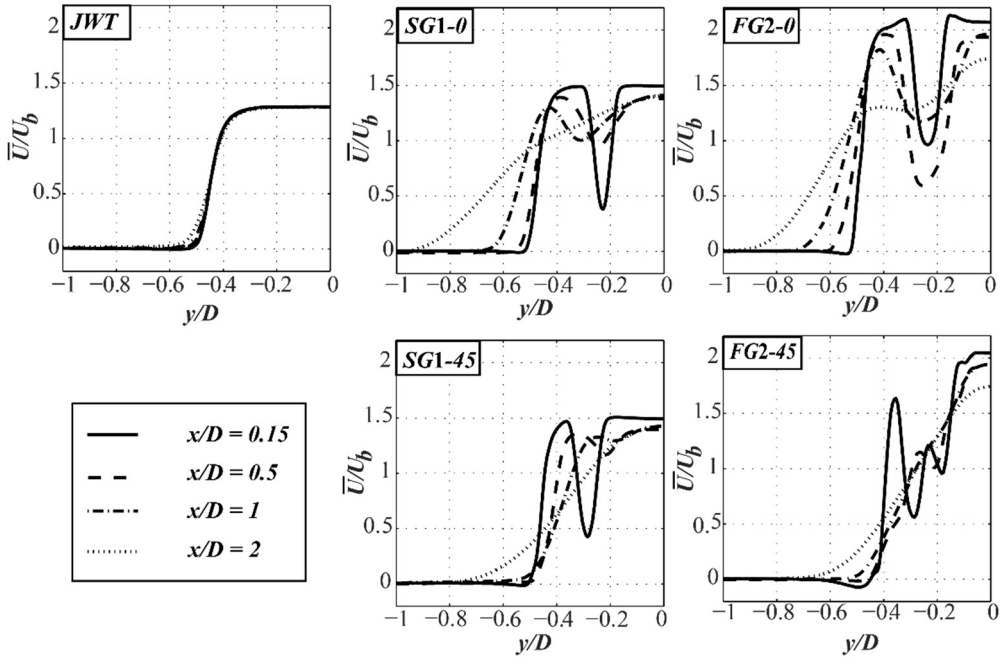


Fig. 4.3 - Mean axial velocity profiles at x/D equal to 0.15, 0.5, 1 and 2, respectively (SFV camera).

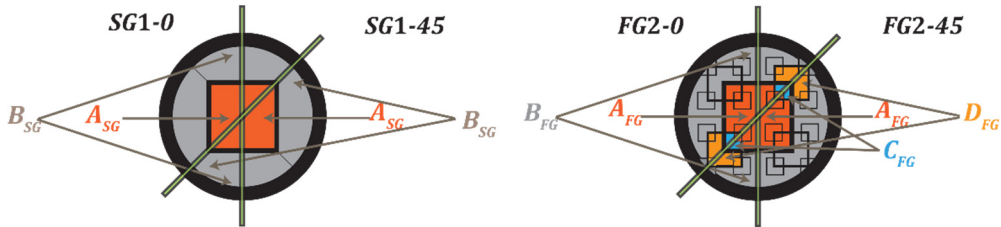


Fig. 4.4 - Schematic of the grids' regions.

Analysing the axial velocity profile for $x/D = 0.15$ reported in Fig. 4.3 it is possible to associate each peak with the corresponding grid's area sketched in Fig. 4.4: the absolute maximum, located at $y/D = 0$, is related to the jet issuing through the A_{FG} -area; the local maximum located at $y/D = -0.23$ is related to the C_{FG} -region; the maximum located at $y/D = -0.35$ corresponds to the D_{FG} -region. The effects of the smallest bars are only slightly appreciable as a slope variation of the axial velocity profile at $y/D = -0.11$. As x/D increases, the velocity peaks are rapidly smeared out: only the A_{FG} -region peak and D_{FG} -region peak are visible at x/D equal to 0.5.

4. THE EFFECTS OF THE SECONDARY ITERATIONS BARS ON CONTINUOUS TURBULENT JETS

The radial velocity maps reported in Fig. 4.5 show that the grid is responsible for nonzero values at short distances from the nozzle due to the momentum diffusion between the different “sub-jets”, as also reported in [2, 3].

The more complex fractal grid geometry reflects in more complex and wider regions of large radial velocity values both close to the nozzle exit section and at the jet boundaries. The effect of secondary iterations bars becomes clearly visible when comparing the *SG1-0* and the *FG2-0* maps. Moreover, at short distances from the nozzle exit section both the *SG1* and the *FG2* maps show larger values of the radial velocity component along the diagonal direction as a consequence of the aforementioned jet shrinking.

It is important to point out that, since the radial velocity distributions are much smaller in intensity than the axial ones, the contour maps are more affected by both systematic and random errors (such as non-perfect uniform magnification or non-perfect alignment with the grid’s middle planes).

The axial velocity component along the jet centreline and the dimensionless jet’s half-width, b_j/D , defined as the radial distance at which the mean axial velocity is equal to the 50 % of its local maximum [73], are reported in Fig. 4.6.

In particular, being the flow fields related to both the *SG1* and the *FG2* not axisymmetric and taking into account of their cross-shaped morphology in proximity of the grid [1, 4], b_j/D is evaluated following the formula used in [91] for cruciform jets:

$$\frac{b_j}{D} = \sqrt{\left(\frac{b_j}{D}\right)_0 * \left(\frac{b_j}{D}\right)_{45}} \quad (4.2)$$

where $\left(\frac{b_j}{D}\right)_0$ is the jet’s half-width evaluated along the xy plane and $\left(\frac{b_j}{D}\right)_{45}$ is the jet’s half-width evaluated along the plane tilted of 45° with respect to the xy one.

In the *JWT* configuration, the axial velocity profile along the centreline shows a *potential-core* region, (defined by the distance up to which the axial velocity along the centreline remains equal to the exit one) that extends up to $4.5D$, in agreement with [2]. For $x/D > 6 \bar{U}/U_b$ and b_j/D increases and decreases almost linearly.

Higher velocity values are reached for the *SG1* and the *FG2* configuration, at short distance from the nozzle, as a consequence of the blockage ratio σ imposed by the grid. Finally, Fig. 4.6-a) shows that, as x/D increases, the flow will eventually loose memory of the grid, approaching the *JWT* profile.

The grids affect the jet width as well, causing a wider and faster jet spreading. In the *JWT* the jet’s half-width is nearly constant for $x/D < 2$ and starts to spread

4.1. MAIN FLOW FEATURES

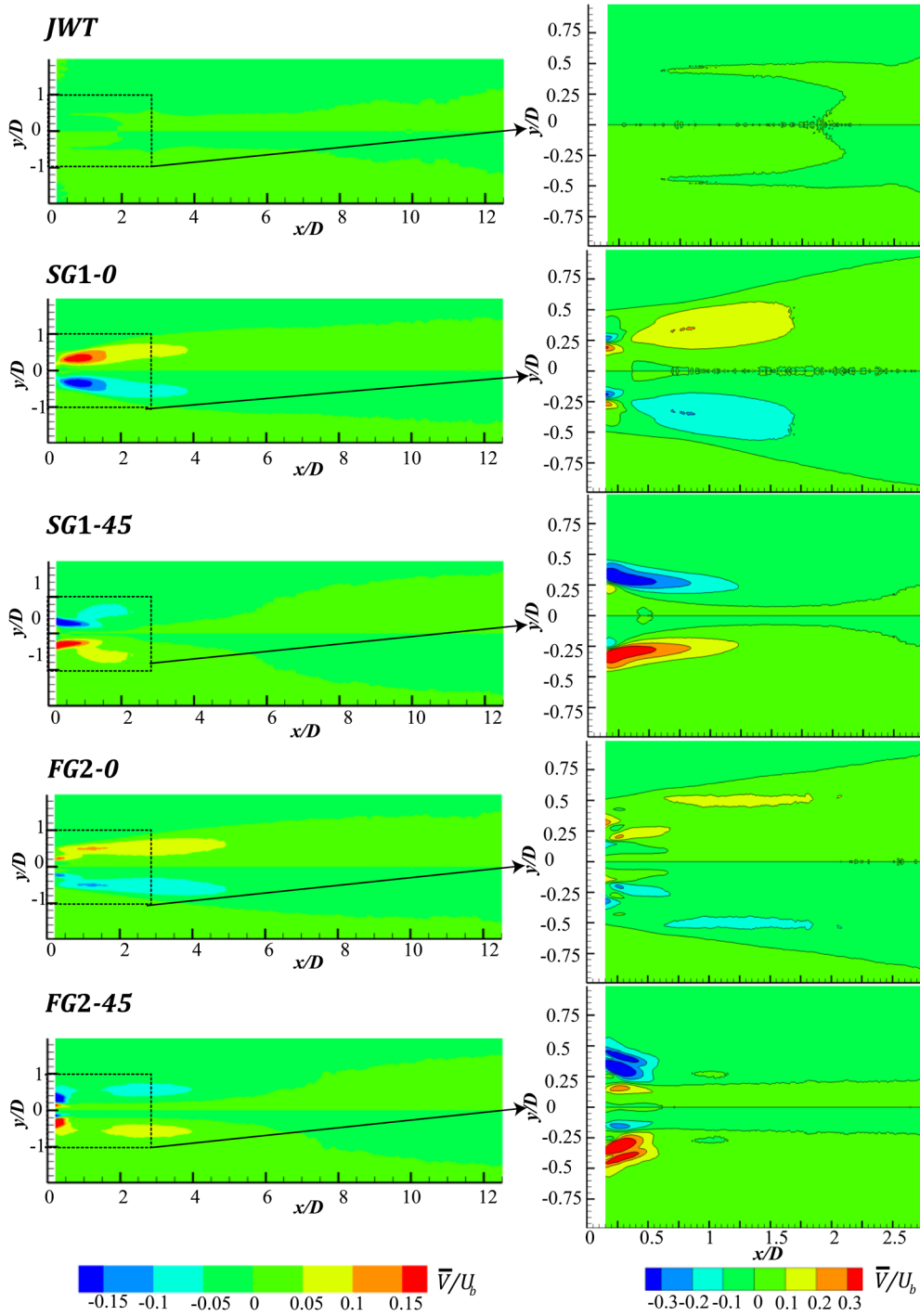


Fig. 4.5 - Time-averaged radial velocity component maps (left: LFV camera / right: SFV camera).

4. THE EFFECTS OF THE SECONDARY ITERATIONS BARS ON CONTINUOUS TURBULENT JETS

linearly at the end of the potential-core ($x/D > 6$) with a jet spreading rate $S = db_j/dx$ equal about to 0.07 (which is consistent with the values reported in the literature [73]).

In the *SG1* case, the jet width remains constant up to $1D$ from the nozzle exit section and starts to spread almost linearly from about $5D$. In the *FG2* case, a thinner jet can be observed close to the grid due to the blockage imposed by the 2nd and 3rd iteration bars'. However, it spreads almost linearly, with $S = 0.048$, for $0.15 < x/D < 4$. This rapid jet spreading, immediately past the grid, is due to the streamwise vorticity generated by the grid itself [2]. The spreading rate attains a constant value of about 0.07 at x/D equal to 5. Finally, Fig. 4.6 also shows that, within the measurement domain, the *SG1* jet is the widest one.

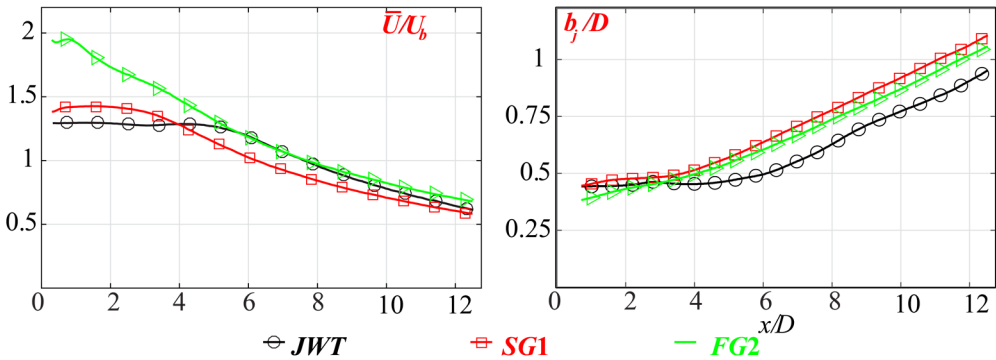


Fig. 4.6 - Mean-axial velocity decay along the jet centreline and jet's half-width for the *JWT*, the *SG1* and the *FG2* cases (LFV camera).

Fig. 4.7 reports the mean axial velocity and the *r.m.s* of the axial and radial components of the velocity fluctuations, u' and v' , measured along the jet centreline by means of the SFV camera. The *JWT* results confirm that, for $x/D < 2.75$, a potential-core region exists. A plateau region can be identified both for the axial and radial fluctuations up to x/D equal to $1.5D$, afterwards the shear layer penetrates towards the jet axis so that u' starts to increase. Moreover, as already discussed, Fig. 4.7 shows that higher velocity values are obtained along the jet centreline when a grid is present. Both the *SG1* and the *FG2* axial velocity profiles \bar{U}/U_b show that the highest velocity is obtained at $x/D = 0.15$ (which is the starting point of the measurement region). \bar{U}/U_b rapidly decreases with x , reaching a local minimum at x/D equal about to 0.4 and 0.5, respectively, and then slightly increase. An almost constant region, for $1.4 < x/D < 2.75$, can be detected for the *SG1* case while the *FG2* profile shows a local maximum at x/D equal to 0.95, after which it monotonically decreases.

4.1. MAIN FLOW FEATURES

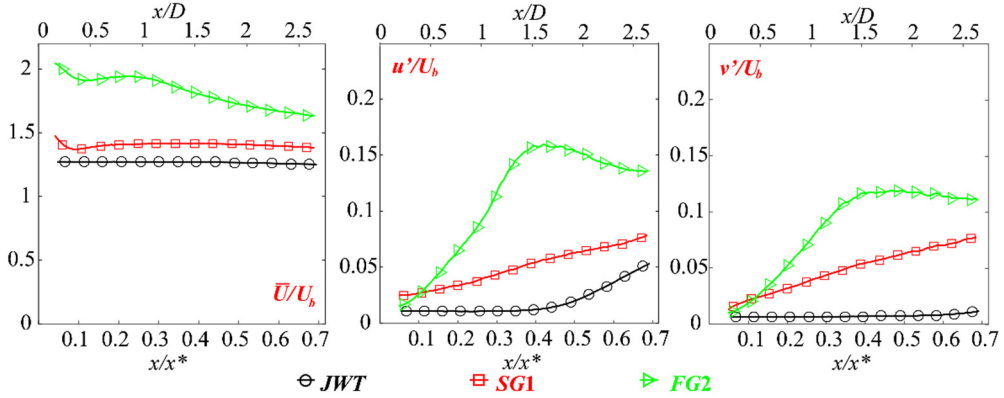


Fig. 4.7 - Mean axial velocity component and r.m.s. of axial and radial velocity fluctuations evaluated along the jet centreline as function of x/x^* and x/D , for all the device configurations (SFV camera).

The grid presence also causes a turbulence production region immediately past the grid, with u' and v' growing faster in the *FG2* case with respect to the *SG1* one. Moreover, while in the *SG1* configuration they increase monotonically for $x/D < 2.75$, the 2nd and the 3rd iteration bars are responsible for a local maximum at x/D equal to about 1.6, according to [2]. In Fig. 4.7, all the velocity components are also reported with respect to x/x^* showing that the u' and v' local maxima are located at about $0.4x^*$. Even if this peak location is only dependent on the biggest iteration bars' sizes, it is surprisingly not present in the *SG1* case. Present results differ from the ones reported in [39, 40] on turbulence generated past a single square grid, in which a peak in the axial fluctuations, located at about $0.5x^*$ and mainly addressed to the vortex shedding generated by the grid's bars, is shown. Therefore, the absence of this peak in the present measurements can be associated with the grid's geometrical features (i.e. L_0 and t_0) and to the Reynolds number Re [92], both influencing the bar's wake development and/or its coupling with the external shear layer.

By means of the LFV camera results the interaction between the grid's effects and the shear layer development can be analysed. The in-plane turbulent kinetic energy $tke = (u'^2 + v'^2)/2$ evaluated along the centreline, for each case, is reported in Fig. 4.8. The inferior spatial resolution of this measurement, with respect to the SFV camera, results in slightly smaller tke values. In the *JWT* configuration, the tke profile shows an initial plateau region which extends up to $2D$. Beyond this point, as the shear layer widens and penetrates towards the jet axis, it increases until reaching a maximum at about $x/D = 7$ after which it decreases (see also the tke maps reported in Fig. 4.9).

4. THE EFFECTS OF THE SECONDARY ITERATIONS BARS ON CONTINUOUS TURBULENT JETS

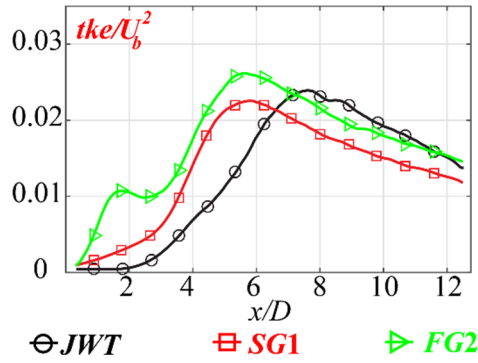


Fig. 4.8 - Time-averaged tke profiles evaluated along the jet centreline and related to the JWT, the SG1 and the FG2 configurations (LFV camera).

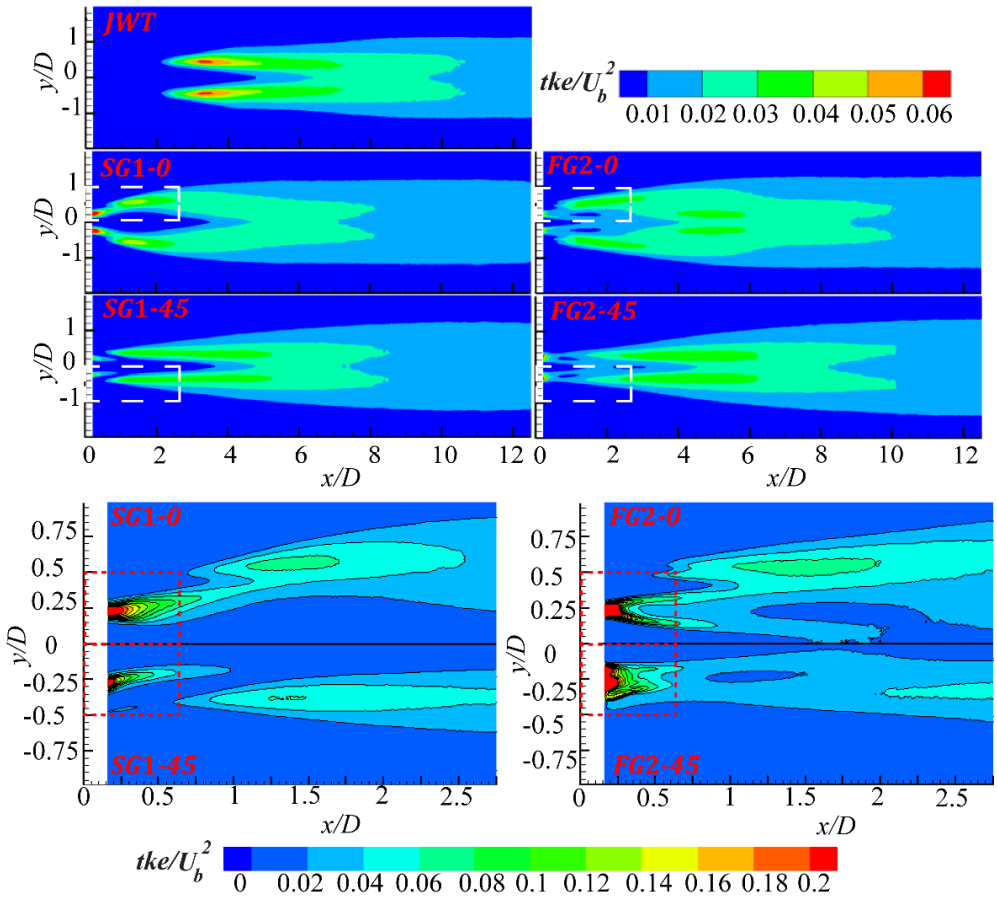


Fig. 4.9 - Time-averaged tke contour maps (top: LFV camera / bottom: SFV camera).

4.1. MAIN FLOW FEATURES

Because of the grid presence, in the *SG1* case the *tke* increases suddenly past the grid, showing a slope variation at about $x/D = 3$. It achieves an absolute maximum at $x/D = 6$, and then decreases. In the *FG2* configuration, the *tke* increases very rapidly for $x/D > 0$ reaching a local maximum at about $x/D = 1.5$. It, then, slightly decreases before increasing again at about $x/D = 3$. An absolute maximum is reached at about $x/D = 5.5$, beyond which the *tke* decreases merging with the *JWT* profile at about $x/D = 11$.

The *tke* contour maps are reported in Fig. 4.9 for both the LFV and the SFV cameras. Both the *SG1* and the *FG2* configurations show different evolutions of the velocity fluctuations along the two measurement planes with regions of nonzero velocity fluctuations, related to the grid-generated turbulence and the shear layer development.

The *SG1* maps, obtained with the SFV camera, show that, along the 0° direction, the wakes generated past the 1st iteration bar expand outward up to merge to the shear layer while, along the 45° plane, they develop towards the jet axis. The introduction of the secondary iterations increases the *tke* values and affects their evolution, also forcing their spreading towards the jet centreline.

The LFV camera results clearly show that the advantages in using both the fractal and the single square grids are significantly reduced at large distances from the nozzle exit section. Indeed, in the external shear layer, higher values of the velocity fluctuations are reached in the *JWT* case.

A low-order-reconstruction of the instantaneous vorticity field is reported in Fig. 4.10: the reconstructed vorticity field is obtained by applying the *snapshot* Proper Orthogonal Decomposition (POD) [93, 94, 95] to the 6,000 instantaneous velocity fields and by using, to perform the reconstruction, an opportune number of POD modes similarly to what suggested by Raiola et al. in [96]. Fig. 4.10 can be useful for understanding the grid's wake development and its interaction with the Kelvin-Helmholtz instabilities.

Two wakes, developing away from the jet centreline, can be observed in the *SG1-0* configuration until they interact with the external jet shear layer. Differently, along the diagonal direction, the wakes develop moving towards the centreline without, however, reaching it because of the interaction with the shear layer. A very different situation is found by using the *FG2*. As reported in Fig. 4.10 the interaction between the wakes generated by bars of different sizes, some of which located very close to each other, affect the vortex shedding originated by the largest bars [39] so that no periodic phenomena can be detected in the present measurement. As expected, the *FG2* produces a wider nonzero vorticity region and the *FG2-0* map shows, differently from the *SG1-0* case, that the 2nd and the 3rd iterations bars cause the grid's wake to

4. THE EFFECTS OF THE SECONDARY ITERATIONS BARS ON CONTINUOUS TURBULENT JETS

develop almost symmetrically with respect to the 1st iteration bars, on one side reaching the x axis at x/D equal about to 1.5 and, on the other side, merging with the external shear layer.

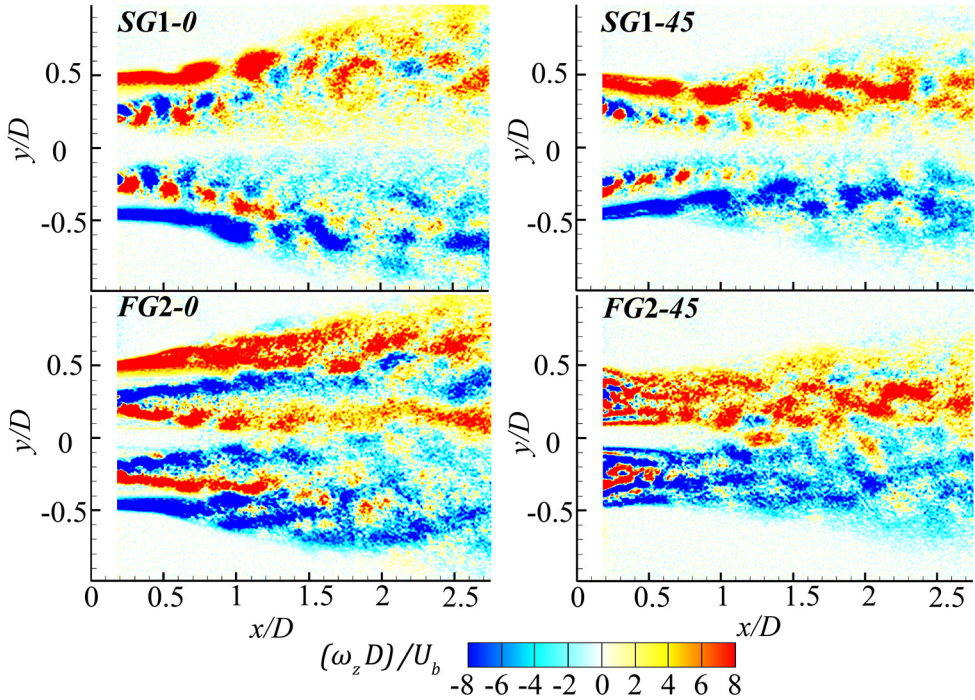


Fig. 4.10 – Low order POD reconstruction of the instantaneous dimensionless vorticity field (SFV camera).

Finally, whilst in the *FG2-0* it is possible to distinguish between the vorticity generated by the grid and the one due to the interaction with the quiescent ambient, at least up to $x/D = 1.5$, in the *FG2-45* map the two contributions cannot be separated probably because of the grid geometry and a lack of spatial resolution.

It is important to underline that Fig. 4.10 is an additional proof for the three-dimensionality of the *FG2* flow field because of the effects of the out-of-plane bars just discussed. Furthermore, it confirms that the shear layer distortions observed in [2, 3], addressed to the grid presence and considered as main actors in the enhancement of the heat and mass transfer due to these turbulators.

4.2. ANALYSES OF THE BARS' WAKES BY MEANS OF THE SNAPSHOT POD

4.2. ANALYSES OF THE BARS' WAKES BY MEANS OF THE SNAPSHOT POD

For both the SG and the FG configurations, the *snapshot* POD technique [93, 94, 95] is also applied to a small area (past the grids' bars) of the 6,000 instantaneous velocity fluctuations fields (identified in Fig. 4.9 by the red dotted lines) in order get further information on the wakes' evolution in a region where their interaction with the external shear layer is negligible.

The eigenvalues λ corresponding to the 30 most energetic modes, nondimensionalised with respect to the total *tke*, for both the *SG1* and the *FG2* configurations, are reported in Fig. 4.11. The nondimensionalised *z*-vorticity $(\omega_z D)/U_b$ maps reported in Fig. 4.12 show that the alternate von-Kármán vortex shedding developed by the bar having a $t_0 \times \ell$ rectangular section (where ℓ indicates the grid thickness) is predominant in the *SG1-0* case, with the first two POD modes accounting for the 33.0% and 29.8% of the total *tke*, respectively. The *tke* contribution rapidly decreases with increasing the POD mode number, down to 2.3% for the 3rd mode, which, as shown by the vector field in Fig. 4.12 and according to the results reported in [97] on the near wake of a 2D square cylinder, could correspond to a symmetrical vortex shedding. Along the 45° direction (see Fig. 4.13), because of the presence of the holding bars and the square edges, the energy content of the first two POD modes is strongly reduced to 10.5% and 9.7% of the total *tke*, respectively. On the other hand, the percentage of energy associated with the 3rd mode increases up to 7%.

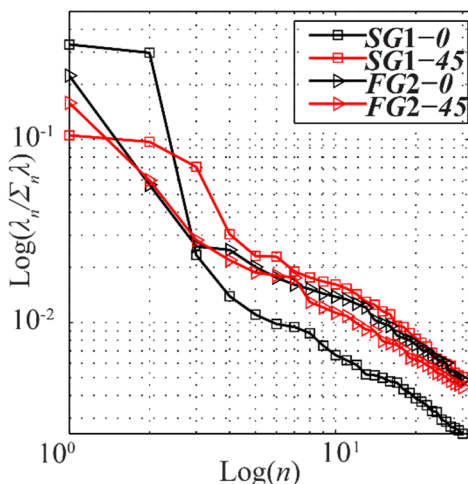


Fig. 4.11 - Eigenvalue distributions of the velocity fluctuations fields, related to the 30 most energetic modes.

4. THE EFFECTS OF THE SECONDARY ITERATIONS BARS ON CONTINUOUS TURBULENT JETS

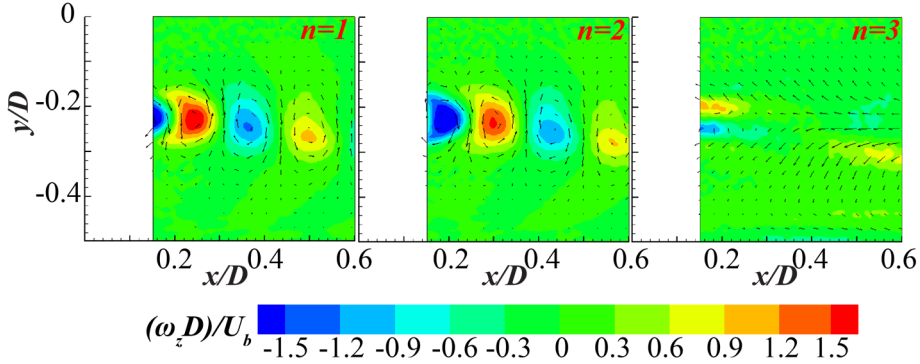


Fig. 4.12 - Nondimensionalised z -vorticity $(\omega_z D)/U_b$ contour maps of the three most energetic modes related to the SG1-0 case (SFV camera).

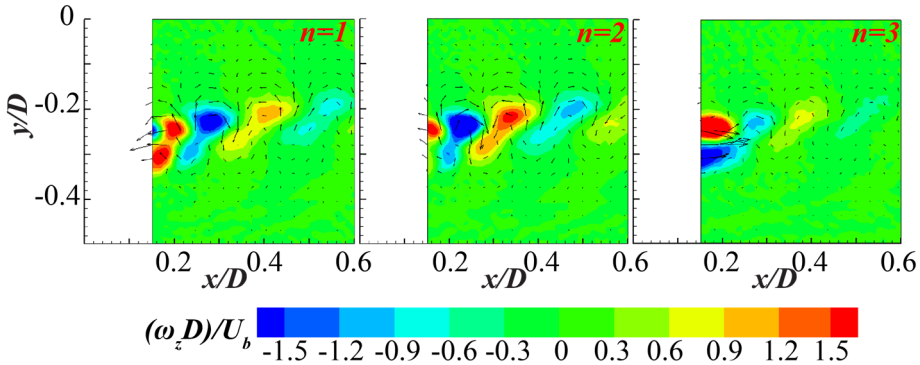


Fig. 4.13 - Nondimensionalised z -vorticity $(\omega_z D)/U_b$ contour maps of the three most energetic modes related to the SG1-45 case (SFV camera).

Because of the secondary iterations bars, the eigenvalues distribution, for the *FG2*, is significantly different. In the *FG2-0*, the wakes developed past the out-of-plane bars interact with the ones generated by the biggest ones affecting their dynamics. In Fig. 4.14 the ω_z contour maps of the most two energetic modes are shown: they account respectively for the 22.3% and then 5.7% of the total kinetic energy and represent the shear layer phenomena produced by the wake of the main bar. The superimposed velocity vectors suggest that they are related to the reverse flow past the 1st iteration bars. Patterns resembling a von-Kármán vortex shedding and showing the interaction between the different wakes can be found visualizing the ω_z contour maps related to higher POD modes, as reported in Fig. 4.14 for $n = 7$. This is a direct consequence of the different bars' sizes, in the sense that smaller bars develop lower energetic modes. On the other hand, even if POD has proved to be an efficient method to describe the turbulent flow past the single square grid (above all for the SG1-0 case), it is not able to separate different shedding phenomena, as already pointed out

4.3. MAIN CONCLUSIONS

in [98]. Therefore, no indication of a univocal correspondence between the mode and the bar generating that coherent vortical structure can be found if the wakes interact (as this interaction changes the mode frequency). Moreover, it must be considered that POD is the representation of the flow fields in a different basis which comes out from a mathematical manipulation, therefore some of the found modes, above all the ones with low energy content, may not have a clear physical meaning.

It is important to notice that, despite the short distance from the grid- $3t_0$ - for the given geometrical parameters of the turbulator, the effect of the secondary iterations on the wakes past the 1st iteration bars is not negligible, differently from what reported in [98] for the medium bar of a square fractal grid located at the entrance of an open water flume facility.

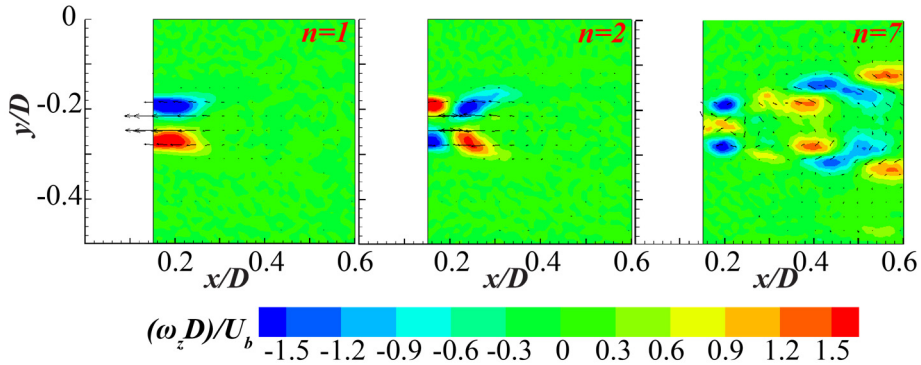


Fig. 4.14 - Nondimensionalised z -vorticity $(\omega_z D)/U_b$ contour maps of the three most energetic modes related to the FG2-0 case (SFV camera).

Finally, the results related to the FG2-45 case show quite a similar distribution of the first eigenvalues with respect to the FG2-0. Even in this case the ω_z contour maps, reported in Fig. 4.15, show the predominance of shear layer phenomena past the bars while for higher mode numbers (i.e. $n = 5,6,7$) von-Kármán like shedding patterns are clearly visible.

4.3. MAIN CONCLUSIONS

In this chapter, the effects due to the secondary iterations of square fractal grids on continuous jets have been experimentally investigated by means of planar PIV, at a fixed Reynolds number equal to 6,700.

4. THE EFFECTS OF THE SECONDARY ITERATIONS BARS ON CONTINUOUS TURBULENT JETS

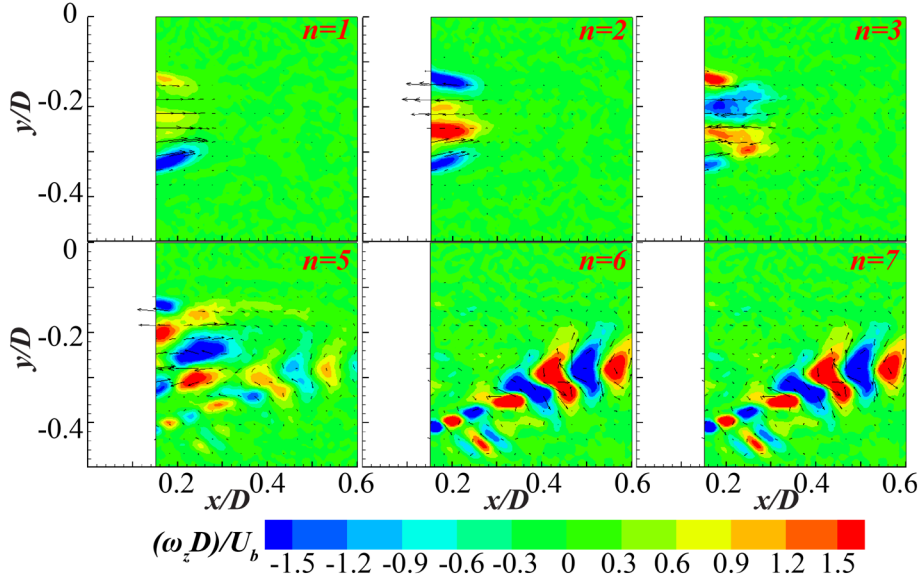


Fig. 4.15 - Nondimensionalised z-vorticity $(\omega_z D)/U_b$ contour maps of the three most energetic modes related to the FG2-45 case.

The main conclusions are here summarised:

- the secondary iterations strongly increase the efficiency in terms of turbulence production of fractal grids, above all at short distances from the nozzle;
- the validity of wake-interaction length scale for predicting the turbulence peak location strongly depends on the global Reynolds number, the grid's geometrical parameters and interaction of the grid-generated turbulence with the jet shear layer;
- the secondary iterations reduce (eventually, suppress) the vortex shedding generated by the largest bars of the fractal grids.

5. THE EFFECTS OF THE SECONDARY ITERATIONS BARS ON SYNTHETIC TURBULENT JETS

In this chapter, the effects of the secondary iterations bars of square fractal grids on the synthetic jet flow field have been investigated by means of 2D2C PIV. Both a 3-iterations square fractal grid or a single square grid, located at the exit section of a round short pipe, are investigated at three different dimensionless stroke lengths, $\mathcal{L}_0/D = 50.0, 19.2$ and 7.1 and at fixed Reynolds number $Re_{sj} = 6,700$. Both time-averaged and phase-averaged results are discussed, with also making a comparison with the synthetic axisymmetric turbulent jet. Finally, comparisons with the continuous jets are reported.

5.1. INTRODUCTION

In this chapter, the free flow field of the synthetic jet device introduced in §3.3.2, is experimentally analysed. Three different actuation frequencies $f = 5 \text{ Hz}, 13 \text{ Hz}$ and 35 Hz are considered for a fixed Reynolds number $Re_{sj} = 6,700$. Three different inlet configurations are considered: *SG1*, *FG2* and no grid. It is worth to underline that this Re_{sj} value only refers to the *JWT* configurations while, for each actuation frequency, for both the *SG1* and the *FG2* cases the operating parameters have been chosen so to produce almost the same active power of the corresponding *JWT* case (see Table 3.5). The corresponding \mathcal{L}_0/D values are $50.0, 19.2$ and 7.1 , respectively, as already reported in §3.3.2. In the following, the results are described by means of the triple decomposition [99]:

$$U_j(\underline{x}, t) = \bar{U}_j(\underline{x}) + \tilde{u}_j(\underline{x}, t) + u_j(\underline{x}, t) \quad (5.1)$$

where $j = 1, 2$ represents the x and the y direction, respectively, and \tilde{u}_j is j^{th} component of the phase-correlated organized contribution to velocity.

The phase-averaged velocity component is defined as:

$$\langle U_j(\underline{x}, t) \rangle = \lim_{N \rightarrow \infty} \frac{1}{N} \sum_{n=0}^{N-1} U_j(\underline{x}, t + n\tau) \quad (5.2)$$

where N is the number of the instantaneous flow fields at same phase and τ is the phenomenon period.

5.2. TIME-AVERAGED FLOW FIELDS

Therefore, the phase-correlated organized contribution is:

$$\tilde{u}_j(\underline{x}, t) = \langle U_j(\underline{x}, t) \rangle - \bar{U}_j(\underline{x}) \quad (5.3)$$

and the turbulent velocity fluctuations are evaluated as:

$$u_j(\underline{x}, t) = U_j(\underline{x}, t) - \langle U_j(\underline{x}, t) \rangle \quad (5.4)$$

This velocity decomposition is introduced to provide a more consistent statistical description of the investigated turbulent flows. In this respect, an underlying hypothesis is that the phase-averaged velocity field defined by Eq. (5.2) coincides with the statistical mean of the instantaneous velocity fields, considered as a random process, at any time corresponding to the same phase. A necessary condition for this is that the statistical properties of the velocity field do not change when shifted by an integer number of periods in time (i.e. the random process is statistically periodic). Considering that the observations corresponding to the same phase are taken, in the worst case, every 10τ such observations are uncorrelated from each other and, under the above assumptions, their mean converges rapidly to the phase-averaged velocity at the considered phase.

Therefore, in the present experiments, the phase-averaged velocity is obtained by simply averaging the observations related to the same phase: as aforementioned, 200 samples per phase are acquired. For what concerns the time-averaged velocity, they can be regarded as the integral of the phase-averaged velocity over the entire period. Therefore, the time-averages of the velocity and all turbulent quantities are calculated by averaging all the 6,000 instantaneous realizations.

All the velocity components are non-dimensionalised with respect to $U_0 = 5.0 \text{ m/s}$ (calculated following the Eq. (3.6) for the *JWT*). Moreover, because of their symmetry with respect to the jet axis, for all the time-averaged velocity quantities an average of the $y < 0$ and $y > 0$ values is performed.

5.2. TIME-AVERAGED FLOW FIELDS

Fig. 5.1-3 show the time-averaged axial velocity component \bar{U}/U_0 maps for all the device configurations and for all the analysed actuation frequencies. Moreover, the \bar{U}/U_0 profiles evaluated along the jet centreline and the jets' half widths (calculated, as for the *CJA* experiment results, by means of Eq. (4.2)) are reported in Fig. 5.4 and Fig. 5.5. According to [85, 100, 101], all these results show that the flow fields are strongly dependent on \mathcal{L}_0/D . Moreover, they are affected by the exit-section geometry, as also found in in [101, 102, 103, 104].

5. THE EFFECTS OF THE SECONDARY ITERATIONS BARS ON SYNTHETIC TURBULENT JETS

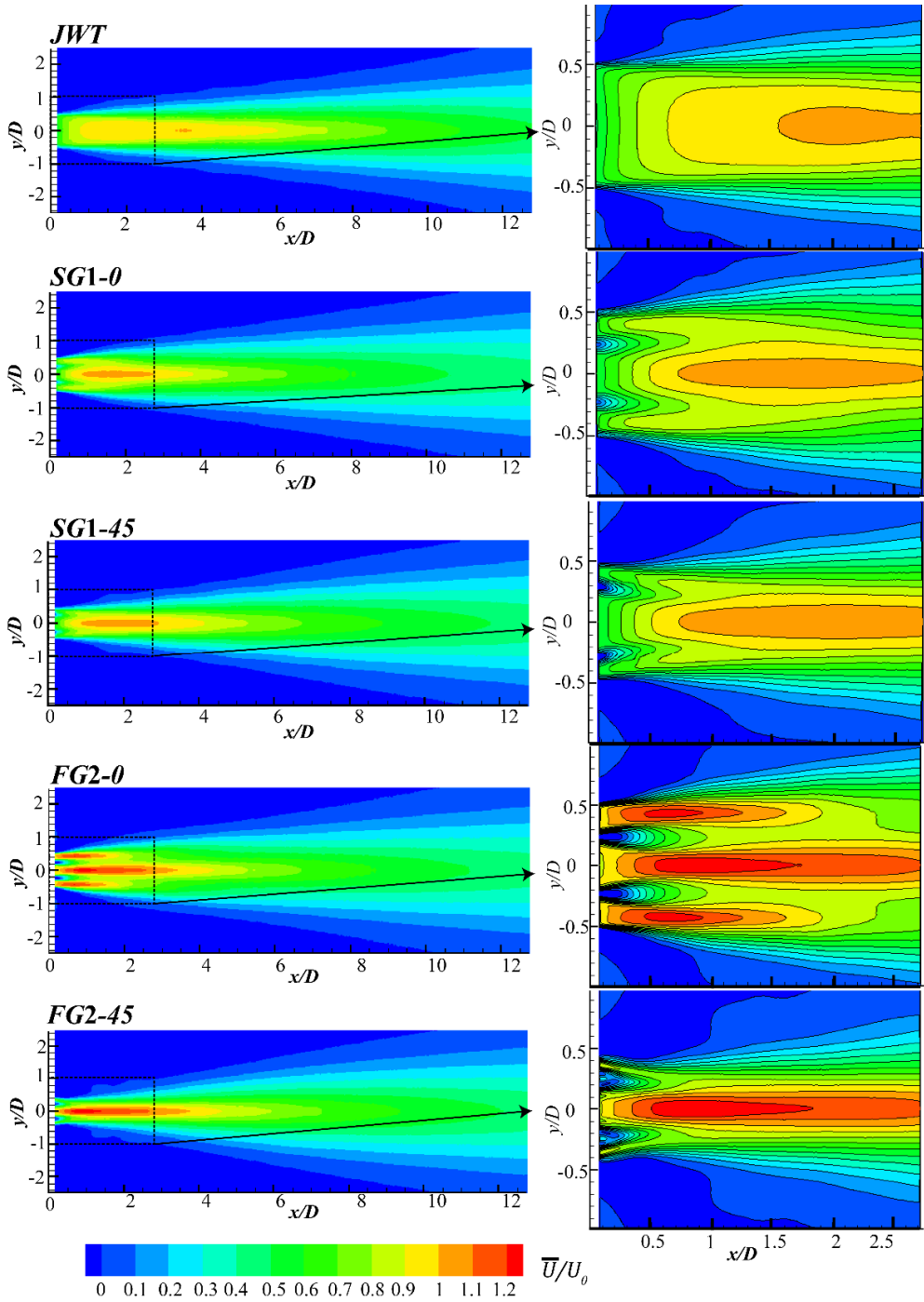


Fig. 5.1 - Time-averaged axial velocity component maps, for $L_0/D = 50.0$ (left: LFV camera / right: SFV camera).

5.2. TIME-AVERAGED FLOW FIELDS

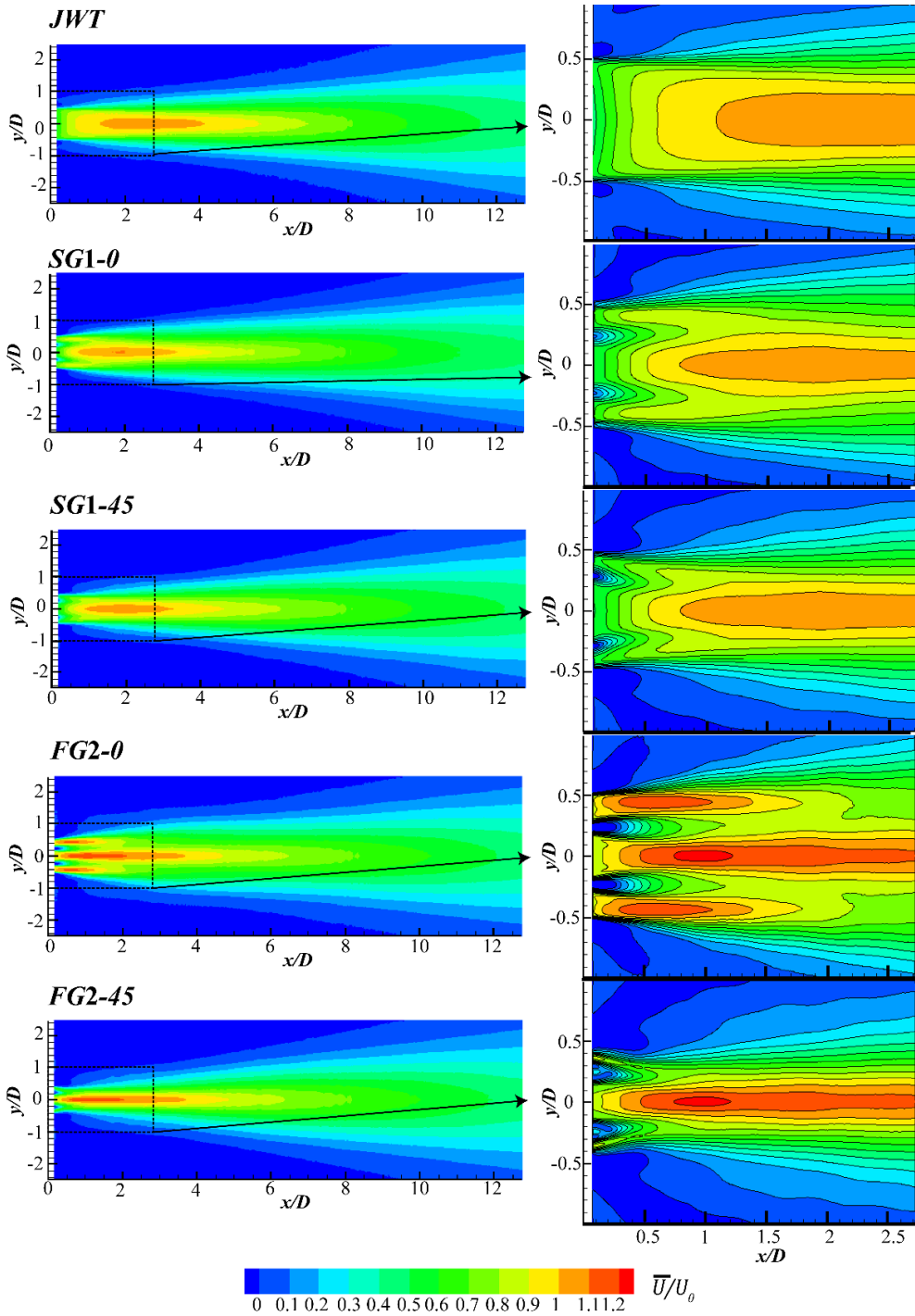


Fig. 5.2 - Time-averaged axial velocity component maps, for $L_0/D = 19.2$ (left: LFV camera / right: SFV camera).

5. THE EFFECTS OF THE SECONDARY ITERATIONS BARS ON SYNTHETIC TURBULENT JETS

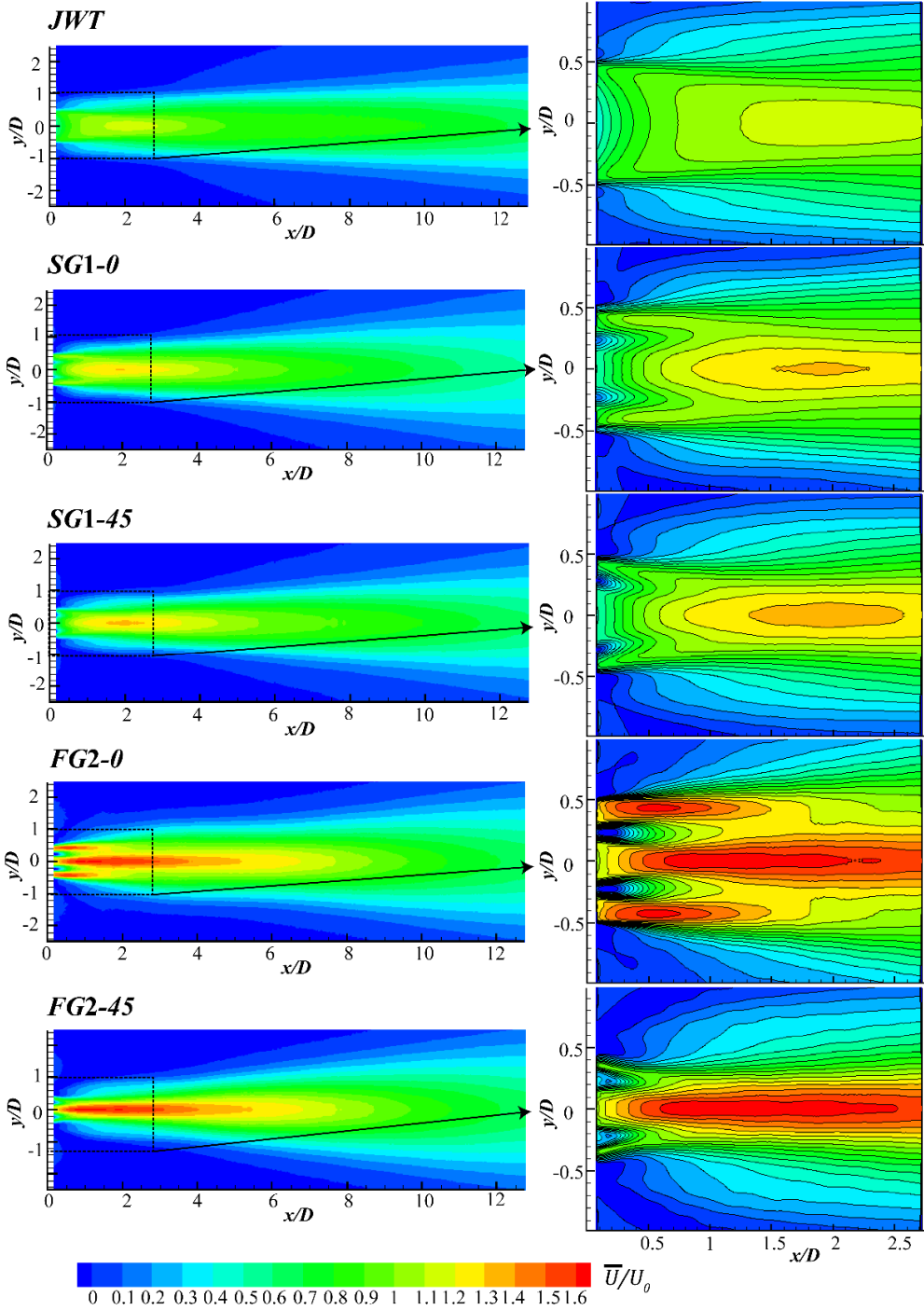


Fig. 5.3 - Time-averaged axial velocity component maps, for $L_0/D = 7.1$ (left: LFV camera / right: SFV camera).

5.2. TIME-AVERAGED FLOW FIELDS

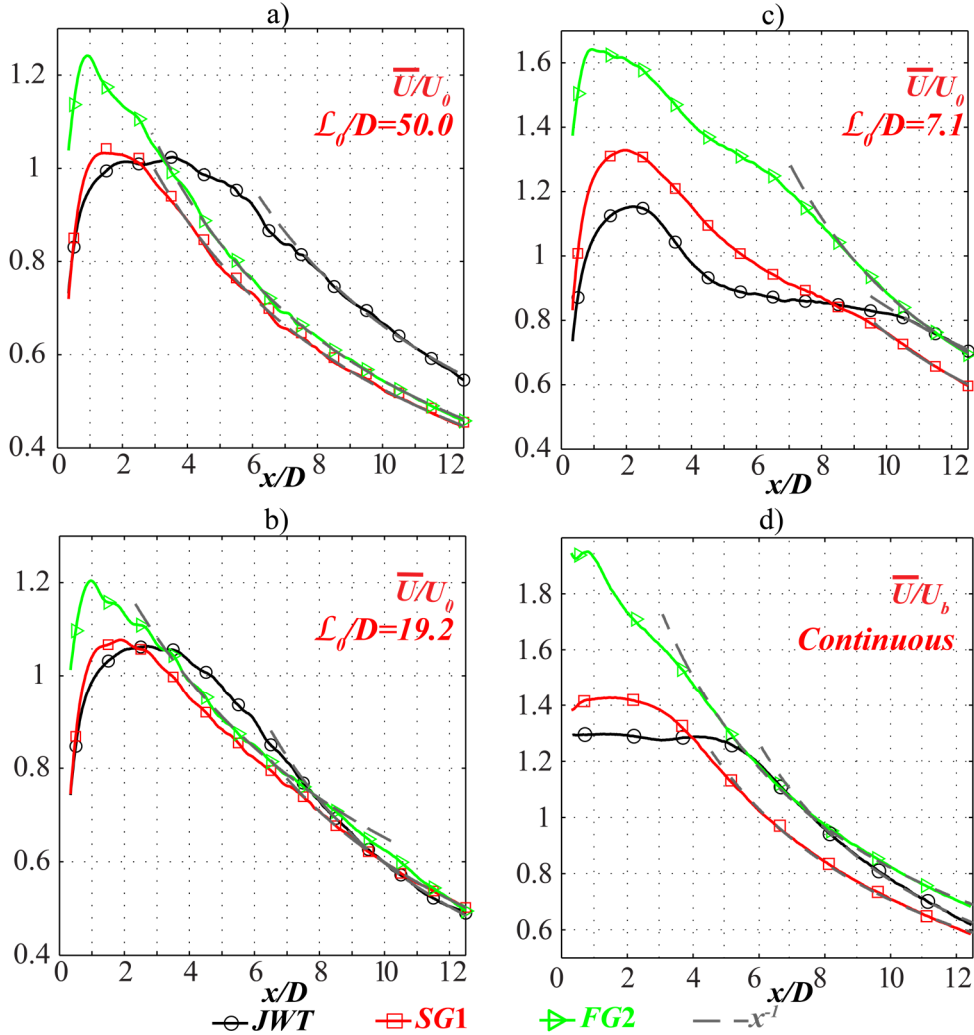


Fig. 5.4 - Time-averaged axial velocity profile \bar{U}/U_0 evaluated along the centreline for both the synthetic jets a) $\mathcal{L}_0/D = 50.0$; b) $\mathcal{L}_0/D = 19.2$, c) $\mathcal{L}_0/D = 7.1$ and the continuous jets d).

As expected because of the peculiarity of synthetic jets to be ZNMF jets, the time-averaged velocity at the nozzle exit section is zero, independently on the nozzle exit section geometry and \mathcal{L}_0/D . Focusing on the *JWT*, differently from the steady turbulent jet evolution reported in Fig. 4.2, for all the three stroke lengths, the mean-axial velocity first increases and then decreases with x/D . Looking at velocity profiles reported in Fig. 5.4, different regions of the synthetic jet evolution are clearly recognizable. For $\mathcal{L}_0/D = 50.0$ (i.e. $f = 5$ Hz), a first zone characterised by the continuous increase of \bar{U}/U_0 from the jet exit section lasts up to $x/D \approx 2$, and it is

5. THE EFFECTS OF THE SECONDARY ITERATIONS BARS ON SYNTHETIC TURBULENT JETS

then followed by a plateau region for $2 < x/D < 4$. Finally, a monotonical velocity decay is shown.

A similar evolution is also visible for $\mathcal{L}_0/D = 19.2$ (i.e. $f = 13 \text{ Hz}$), with however, a slightly larger velocity maximum, a shorter plateau region and a more rapid decay. A different scenario is shown for the lowest dimensionless stroke length (i.e. $f = 35 \text{ Hz}$) as the velocity does not decay monotonically but presents a second plateau for $5.5 < x/D < 10.5$ and then starts to decrease again. This slope variation in the velocity decay must be related to the interaction between the subsequent vortices. Indeed from the phase-averaged flow field shown in Fig. 5.6 for the *JWT* configuration and for this given \mathcal{L}_0/D value, two vortex rings are clearly recognizable in the velocity measurements. This means that the coherent vortical structures (CVSs) are present through the all actuation period and the vortex ring generated by the previous device actuation period coexist with the current one. Fig. 5.6 also gives a more complete interpretation of the physical meaning of the dimensionless stroke length as the distances between the two vortical structures is about 8 diameters, therefore very similar to \mathcal{L}_0/D .

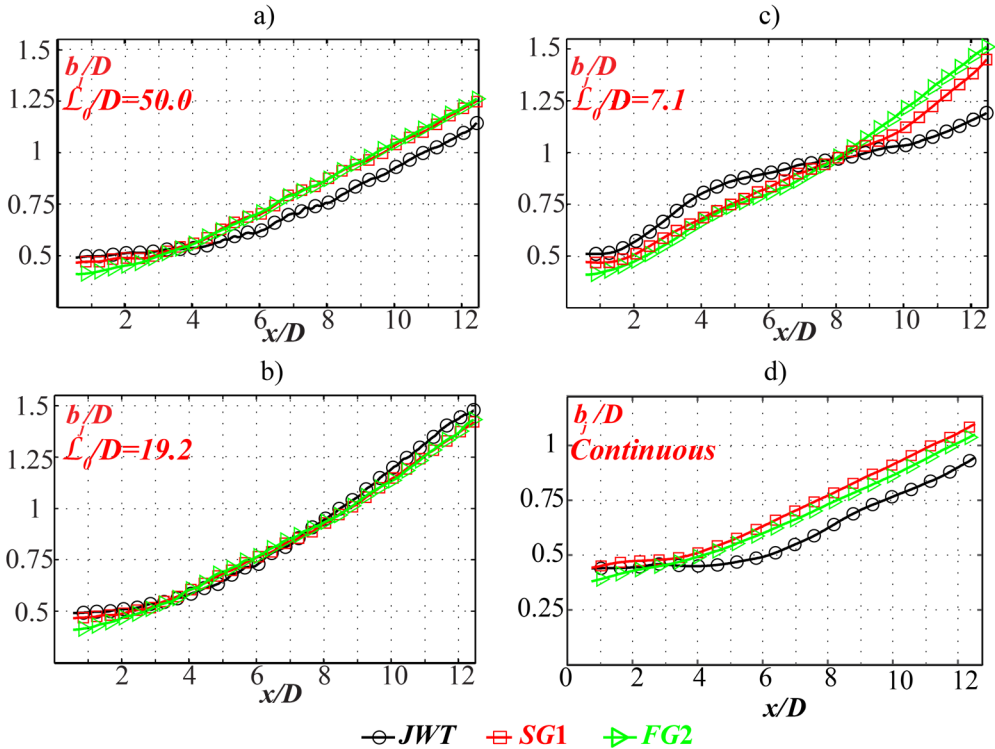


Fig. 5.5 - Jet's half-width b_j/D for both the synthetic a) $\mathcal{L}_0/D = 50.0$, b) $\mathcal{L}_0/D = 19.2$, c) $\mathcal{L}_0/D = 7.1$ and the continuous jets d).

5.2. TIME-AVERAGED FLOW FIELDS

Finally, the dashed lines in Fig. 5.4 are representative of the regions where \bar{U}/U_0 scales proportionally to x^{-1} that, for $\mathcal{L}_0/D = 50.0$ and 19.2 , hold from $x/D \approx 7.5$. For $\mathcal{L}_0/D = 7.1$ this region is not present because of the effect of the vortices coexistence, as already explained.

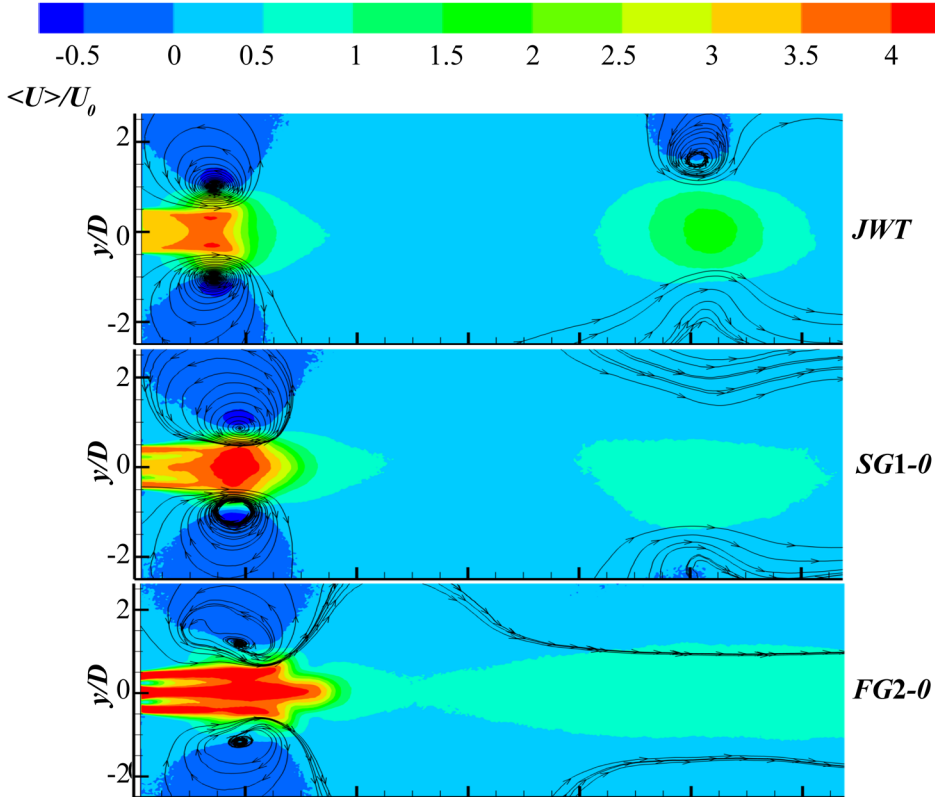


Fig. 5.6 - Axial phase-averaged velocity component $\langle U \rangle/U_0$ for $\mathcal{L}_0/D = 7.1$.

When introducing the grids, the time-averaged axial velocity maps reported in Fig. 5.1-3 resemble the ones shown in Fig. 4.2, therefore the same accelerated and decelerated regions described for the continuous jets can be detected. Moreover, as for the *JWT*, the \bar{U}/U_0 values and the jet spreading are influenced by the actuation frequency. The velocity decay along the jet centreline, reported in Fig. 5.4, shows, for $\mathcal{L}_0/D = 50.0$ and 19.2 , a similar evolution with respect to the *JWT* configuration, above all for the *SG1* case. However, because of the turbulator, the peak velocity is reached earlier as also the x^{-1} -law decay. Interestingly, for all the tested actuation frequencies f , in the *FG2* case the \bar{U}/U_0 maximum occurs at about $0.9D$, suggesting the grid's secondary iterations are of paramount importance on the evolution of the near field developed by this synthetic jet device. The grids' effects

5. THE EFFECTS OF THE SECONDARY ITERATIONS BARS ON SYNTHETIC TURBULENT JETS

on the vortical structures development are evident for $\mathcal{L}_0/D = 7.1$, where the plateau region present at $5.5 < x/D < 10.5$ in the *JWT* configuration disappears. In this respect, the vector fields in Fig. 5.5 show that the strength of the vortex ring related to the previous actuation period is strongly reduced by the grids, above all in the *FG2* case.

The jet's half-width b_j/D for all the device configurations and \mathcal{L}_0/D values is reported in Fig. 5.5. As already reported in [105] for the circular jet, the width of the synthetic jet increases faster than the continuous one, and this conclusion still holds if the grids are inserted. The curves show that the reduction in \mathcal{L}_0/D , from 50.0 to 7.1, causes an increase in b_j/D . However, a different jet width evolution is visible at $\mathcal{L}_0/D = 7.1$ for the *JWT*, as already explained.

The *r.m.s* of the time-averaged axial velocity fluctuations u'/U_0 evaluated along the jet centreline are reported in Fig. 5.7. It is worth to notice that, despite the same experimental setup and processing algorithm, the noisier velocity fluctuations profiles obtained by analysing the synthetic jets with respect the steady ones are a direct consequence of the ensemble average of 6,000 realizations representing different phenomenon periods.

Focusing on the *JWT*, the u'/U_0 values close to the nozzle-exit section are significantly larger than the continuous jet ones, above all at the lowest stroke length. Moreover, for all the \mathcal{L}_0/D values, the axial fluctuations increase with the downstream location. However, the way in which they develop is strongly influenced by the stroke length (as it is clear by looking at the curve related to $\mathcal{L}_0/D = 7.1$).

The same trend can be detected even if the grids are introduced. Moreover, both the *SG1* and the *FG2* cause an increase in the turbulence production close to the nozzle exit section. Focusing on $\mathcal{L}_0/D = 50.0$ and $\mathcal{L}_0/D = 19.2$, it is worth to notice that, as for conventional jets, the advantages in using these grids as turbulence promoters are appreciable only close to the nozzle exit section since all the curves collapse at $x/D \geq 8$ and $x/D \geq 7$, respectively. No collapse is visible for the lowest \mathcal{L}_0/D : in terms of u' evaluated along the centreline, the introduction of the square turbulator becomes disadvantageous for $x/D \geq 11.5$ and at even shorter distances ($x/D \geq 9.75$) if the fractal geometry is used. The importance of the secondary iterations of the *FG2* is also appreciable by looking at Fig. 5.7 indeed, for all the analysed actuation frequencies, the obtained u'/u_0 profiles show a similar shape close to the grid with the presence of the same peculiar peak found for the continuous jets (see also Fig. 4.7 and Fig. 4.8) at about the same downstream location (i.e. $x/D = 1.6$).

5.3. PHASE-AVERAGED FLOW FIELDS

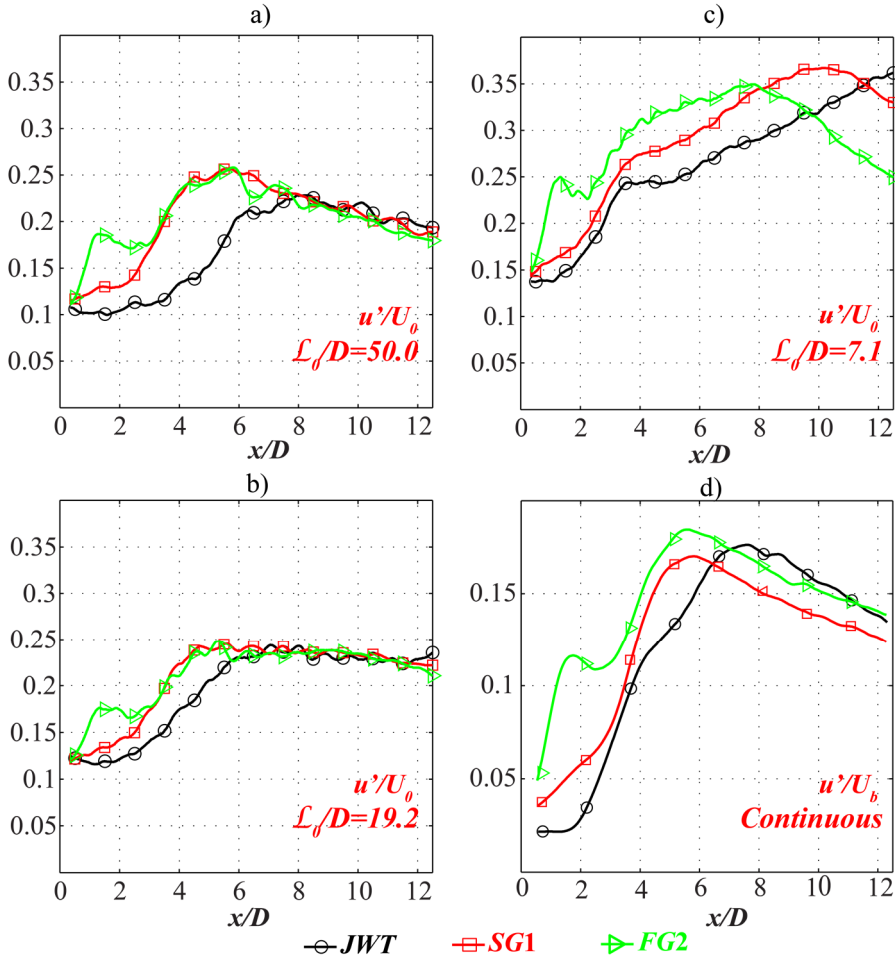


Fig. 5.7 - Time-averaged axial velocity fluctuations u'/U_0 evaluated along the jet centreline for both the synthetic a) $L_0/D = 50.0$, b) $L_0/D = 19.2$, c) $L_0/D = 7.1$ and the continuous jets d).

5.3. PHASE-AVERAGED FLOW FIELDS

In this paragraph, the phase-averaged results are reported. The phase value is indicated as Φ and the starting phase $\Phi = 0^\circ$ is assumed to be the one at which the axial velocity $\langle U \rangle/U_0$, at the centre of the nozzle exit section, switches from negative to positive values, in agreement with [100]. In the following, great importance is given to the CVSs and their evolution. The detection of these CVSs is performed by means of the Q-criterion, which identifies vortex regions as the ones where the rotation-rate magnitude exceeds the strain-rate magnitude:

5. THE EFFECTS OF THE SECONDARY ITERATIONS BARS ON SYNTHETIC TURBULENT JETS

$$Q = -\frac{1}{2} \frac{\partial \langle U_j \rangle}{\partial x_i} \frac{\partial \langle U_i \rangle}{\partial x_j} > 0 \quad (5.5)$$

where $x_1 = x$ and $x_2 = y$.

The phase-averaged axial velocity contours with superimposed velocity vectors, for the *JWT* configuration at $\mathcal{L}_0/D = 50.0$, are shown in Fig. 5.8 (for the sake of brevity, only the most representative phases are reported). At $\Phi = 12^\circ$, no vortical structures can be observed since the ejection phase has just begun; a fully-formed vortex ring can be, instead, detected, for $\Phi = 36^\circ$, at about $x/D = 2$. The toroidal structure is followed by a trailing jet, in agreement with the formation criterium presented by [85] (see also §3.3.1). As the phase increases, the vortex ring moves away from the nozzle exit section while spreading radially because of the faster fluid in the trailing jet. For $\Phi = 132^\circ$, it is outside of the measurement domain therefore it is not possible to assess if it accounts for the entire ejection period or if it dissipates earlier because of the destabilizing effects (first manifested by the skewed vortex ring for $\Phi = 84^\circ$) of the faster trailing jet (clearly visible for $\Phi \geq 84^\circ$), as reported in [85] for this given \mathcal{L}_0/D value.

The phase-averaged axial velocity contour maps related to *JWT* configuration at $\mathcal{L}_0/D = 19.2$ are reported in Fig. 5.9. They show a slower development of the vortex ring than the previous case. Moreover, differently to what observed by McGuinn et al. [85] at this \mathcal{L}_0/D value for an axisymmetric synthetic jet issued through an orifice (while in this case the device is also formed by a short-pipe), the peak velocity always occurs within the vortex core and the vortex ring does not break up during the device ejection phase (as clearly shown for $\Phi = 204^\circ$ where the reverse flow close to the nozzle identifies the suction period).

Fig. 5.10 shows that also at the highest frequency, i.e. $\mathcal{L}_0/D = 7.1$, a fully-formed vortex ring develops, as suggested by the formation of a trailing jet, which is, however, shorter than those of the previous cases, according to the lower amount of fluid issued during the ejection period. As already reported in the time-averaged results paragraph, the vortex ring does not disappear during the whole actuation period. Indeed, in almost all the phases, the presence of two CVSs can be observed simultaneously. Finally, the results show that the velocity peak still occurs in the vortex core and the vortex ring radius does not seem to increase significantly with the phase. Results related to both the *SG1* and the *FG2* configuration, both along the 0° and the 45° direction, for $\mathcal{L}_0/D = 50.0$, are shown in Fig. 5.11 and Fig. 5.12, respectively. For the sake of brevity also in this case only few representative phases of the periodical flow fields, in terms of mean axial velocity component $\langle U \rangle/U_0$ maps, are reported. These maps, superimposed with velocity vectors, show a similar

5.3. PHASE-AVERAGED FLOW FIELDS

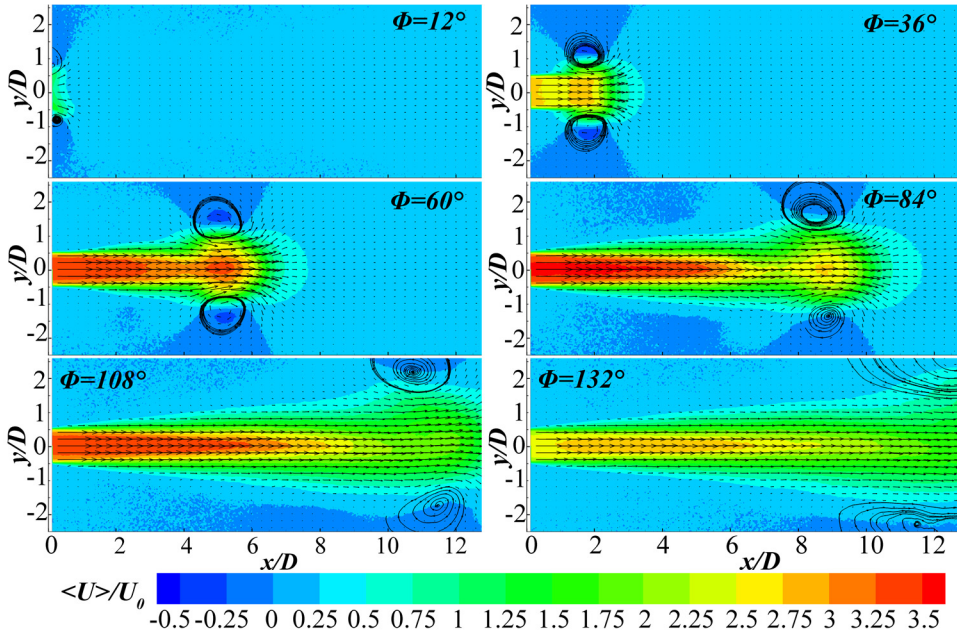


Fig. 5.8 - Contours of the phase-averaged axial velocity superimposed with velocity vectors (plotted each 15×10 points) for the JWT case at $L_0/D = 50.0$ (LFV camera).

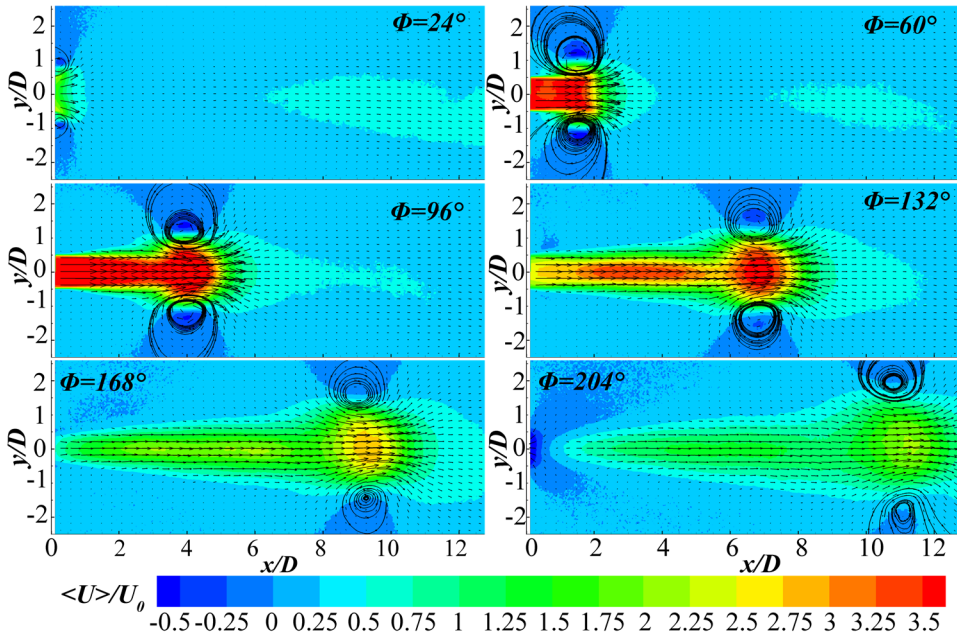


Fig. 5.9 - Contours of the phase-averaged axial velocity superimposed with velocity vectors (plotted each 15×10 points) for the JWT case at $L_0/D = 19.2$ (LFV camera).

5. THE EFFECTS OF THE SECONDARY ITERATIONS BARS ON SYNTHETIC TURBULENT JETS

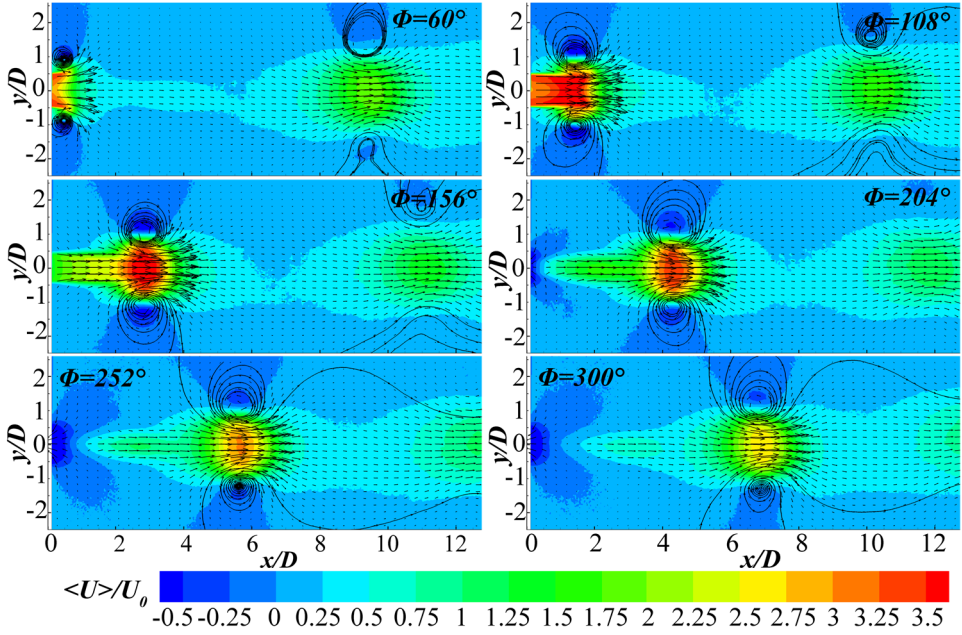


Fig. 5.10 - Contours of the phase-averaged axial velocity superimposed with velocity vectors (plotted each 15×10 points) for the JWT case at $L_0/D = 7.1$ (LFV camera).

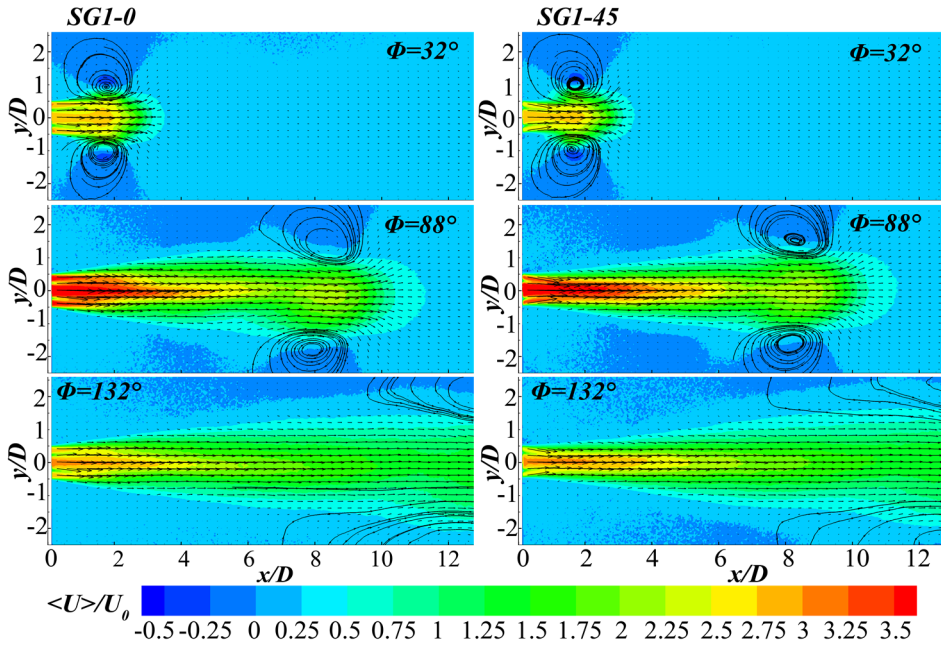


Fig. 5.11 - Contours of the phase-averaged axial velocity superimposed with velocity vectors (plotted each 15×10 points) for the SG1 case at $L_0/D = 50.0$ (LFV camera).

5.3. PHASE-AVERAGED FLOW FIELDS

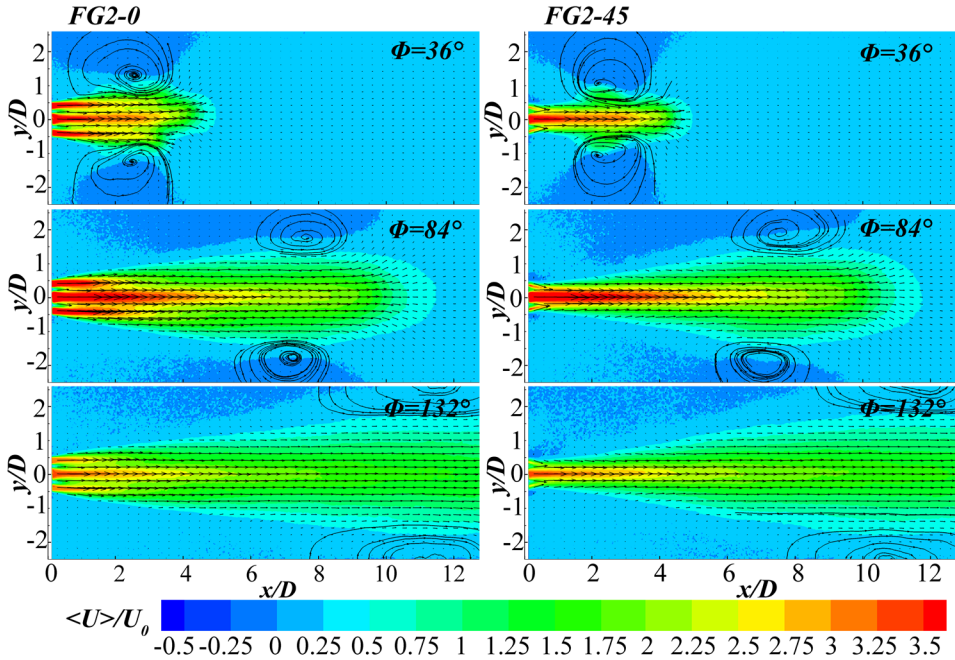


Fig. 5.12 - Contours of the phase-averaged axial velocity superimposed with velocity vectors (plotted each 15×10 points) for the FG2 case at $L_0/D = 50.0$ (LFV camera).

flow field evolution with respect to the *JWT*, whilst a different trailing jet morphology close to the grids (as expected). Moreover, despite the turbulators, the footprint of the external CVS (that cannot be certainly referred as a vortex ring since only 2D measurements are available), identified by means of the streamtracers, is still visible all along the measurement domain.

Similar conclusions can be also drawn for $L_0/D = 19.2$, as the $\langle U \rangle/U_0$ maps reported in Fig. 5.13 and Fig. 5.14 show similar evolutions of the CVSs with respect to the *JWT* (see Fig. 5.9). However, their radius seems to increase and their velocity decrease with the introduction of the turbulators, above all for the fractal geometry. Moreover, more significant differences can be seen comparing the *FG2-0* and the *FG2-45* maps with respect to the $L_0/D = 50.0$ measurements thus suggesting that the increase in frequency gives more importance to the grid geometry with respect to the synthetic jet phenomenology. This trend is also suggested by looking at the $L_0/D = 7.1$ results (see Fig. 5.15 and Fig. 5.16) where the differences pointed out while discussing the time-averaged measurements are still present. As expected higher velocities with respect to the *JWT* are reached, close to the nozzle exit section, because of the grid. Moreover, while the *SG1* flow topology resembles the *JWT* ones, the absence of the footprint of the CVS related to the previous actuation period

5. THE EFFECTS OF THE SECONDARY ITERATIONS BARS ON SYNTHETIC TURBULENT JETS

suggests that the CVS does not last for a complete cycle, probably because of a faster trailing jet that, overtaking it, promotes its breakdown.

In Fig. 5.17 and Fig. 5.18 the $Q > 0$ regions with superimposed velocity vectors, evaluated by means of the SFV camera measurements and related to the $\mathcal{L}_0/D = 19.2$ and $\mathcal{L}_0/D = 7.1$ runs, are reported. For the sake of brevity only some of the ejection phases, for each device configurations, are reported. Concerning the *JWT*, these contour maps do not give any further information with respect to phase-averaged axial velocity maps described above. On the other hand, they show that the introduction of either the *SG1* or the *FG2* causes the generation of additional vortical structures which develop past the grids' bars.

By analysing the $Q > 0$ contour maps related to the *SG1*, in Fig. 5.17, it can be observed that the CVSs develop in a different way along the 0° and the 45° direction, with the outer *SG1-45* Q -positive region lagging with respect to the corresponding *SG1-0* Q -positive region. The presence of two CVSs as also their different evolution along the two measurement planes is even more evident by looking at the *FG2* results, as direct consequence of the secondary iterations bars. The crosswise locations of the inner CVSs correspond to the 1st iterations grid's bars.

However, it could be possible that similar structures are also generated at the edges of the smallest bars and they are not visible in the measurement domain because they have already dissipated or interacted with the vortical regions developed past the 1st iteration bars or, more simply, because the spatial resolution is not fine enough to detect them.

As for $\mathcal{L}_0/D = 19.2$, the same CVSs can be also detected for $\mathcal{L}_0/D = 7.1$, as shown in Fig. 5.18. Moreover, for this given \mathcal{L}_0/D value, the different evolution of the CVSs along the two measurement planes, in the *FG2* case, is even more evident.

Looking at the maps corresponding to $\Phi = 96^\circ$ it can be observed that the centroid of the outer $Q > 0$ region is located at $x/D \approx 2$ along the 0° direction while it is located at about $1.5D$ from the nozzle exit section along the 45° direction. This difference is strongly reduced in the *SG1* maps. This different evolution of the CVSs shown in Fig. 5.17 and Fig. 5.18 (refer also to the streamtracers in Fig. 5.15 and Fig. 5.16), suggests that the analysed grids, for the tested \mathcal{L}_0/D values, not only do not prevent the generation of a synthetic jet but are also responsible for additional vortical structures which interact with the main one causing its azimuthal deformations and its more rapid breakdown, similarly to what has been observed for a synthetic jet device with a chevron nozzle exit [106]. As already found in [2, 3] for conventional steady jets, these azimuthal deformations could be responsible for an increase in the streamwise vorticity production (remarkable in terms of jet scalar transport and mixing efficiency [4, 107]) at short distances from the nozzle.

5.3. PHASE-AVERAGED FLOW FIELDS

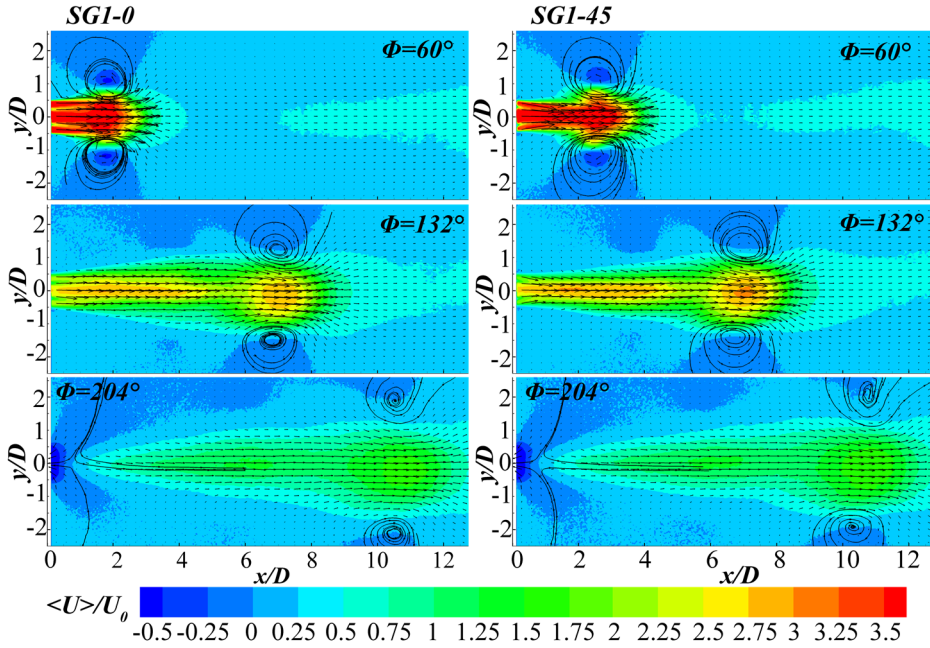


Fig. 5.13 - Contours of the phase-averaged axial velocity superimposed with velocity vectors (plotted each 15×10 points) for the SG1 case at $L_0/D = 19.2$ (LFV camera).

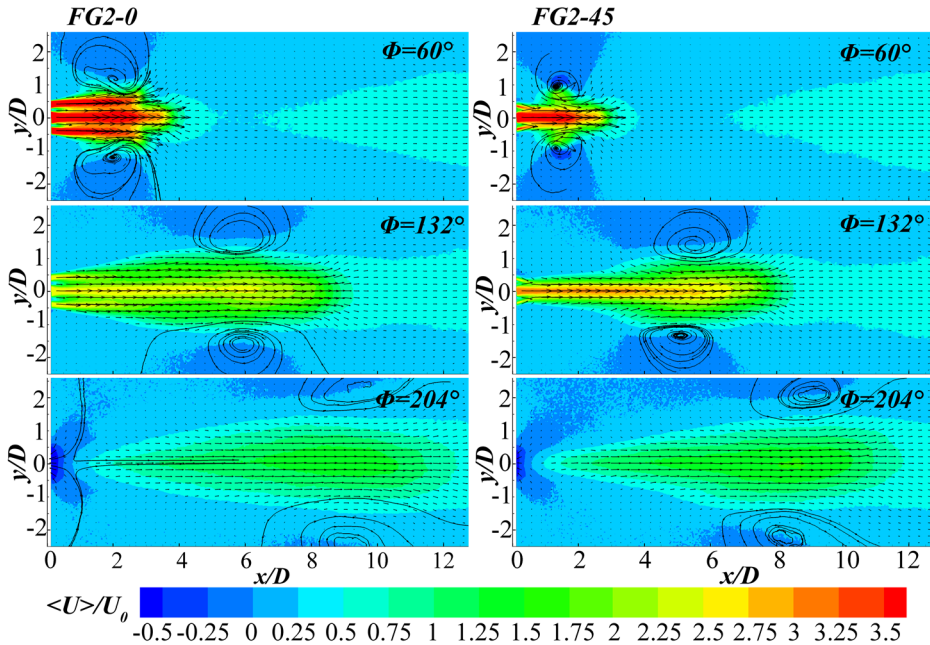


Fig. 5.14 - Contours of the phase-averaged axial velocity superimposed with velocity vectors (plotted each 15×10 points) for the FG2 case at $L_0/D = 19.2$ (LFV camera).

5. THE EFFECTS OF THE SECONDARY ITERATIONS BARS ON SYNTHETIC TURBULENT JETS

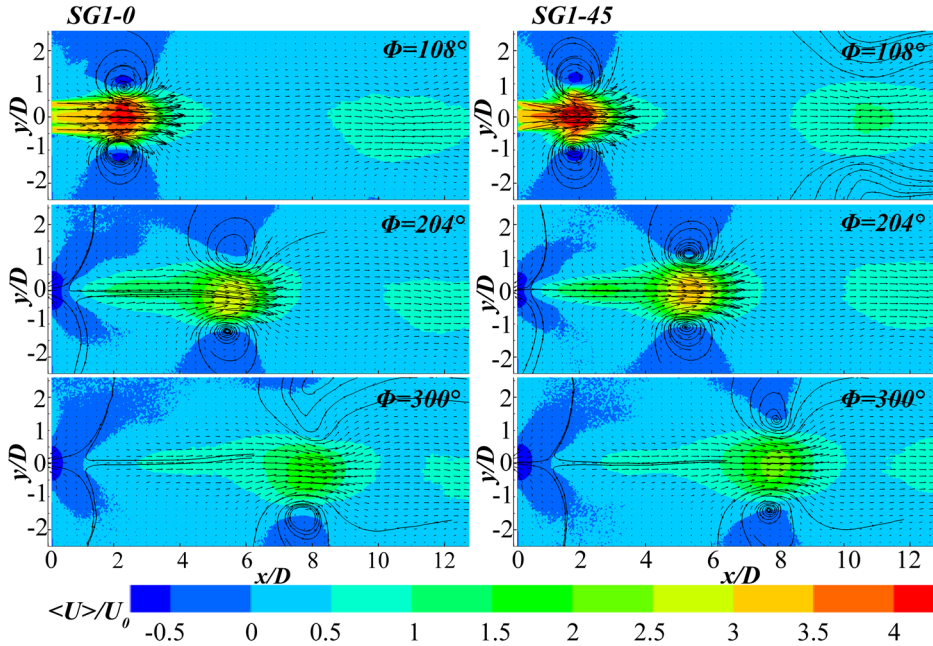


Fig. 5.15 - Contours of the phase-averaged axial velocity superimposed with velocity vectors (plotted each 15×10 points) for the SG1 case at $L_0/D = 7.1$ (LFV camera).

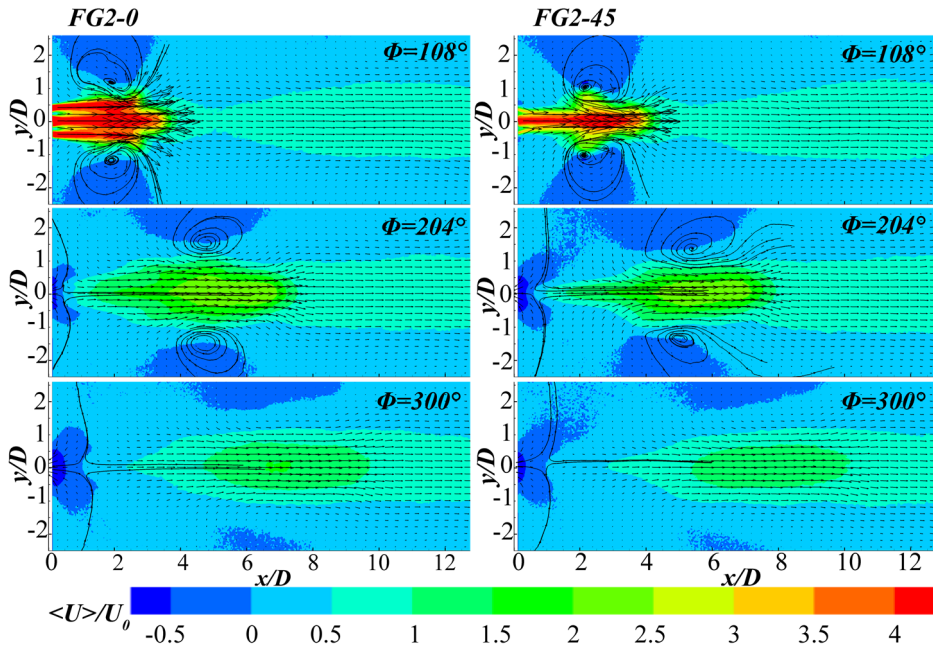


Fig. 5.16 - Contours of the phase-averaged axial velocity superimposed with velocity vectors (plotted each 15×10 points) for the FG2 case at $L_0/D = 7.1$ (LFV camera).

5.3. PHASE-AVERAGED FLOW FIELDS

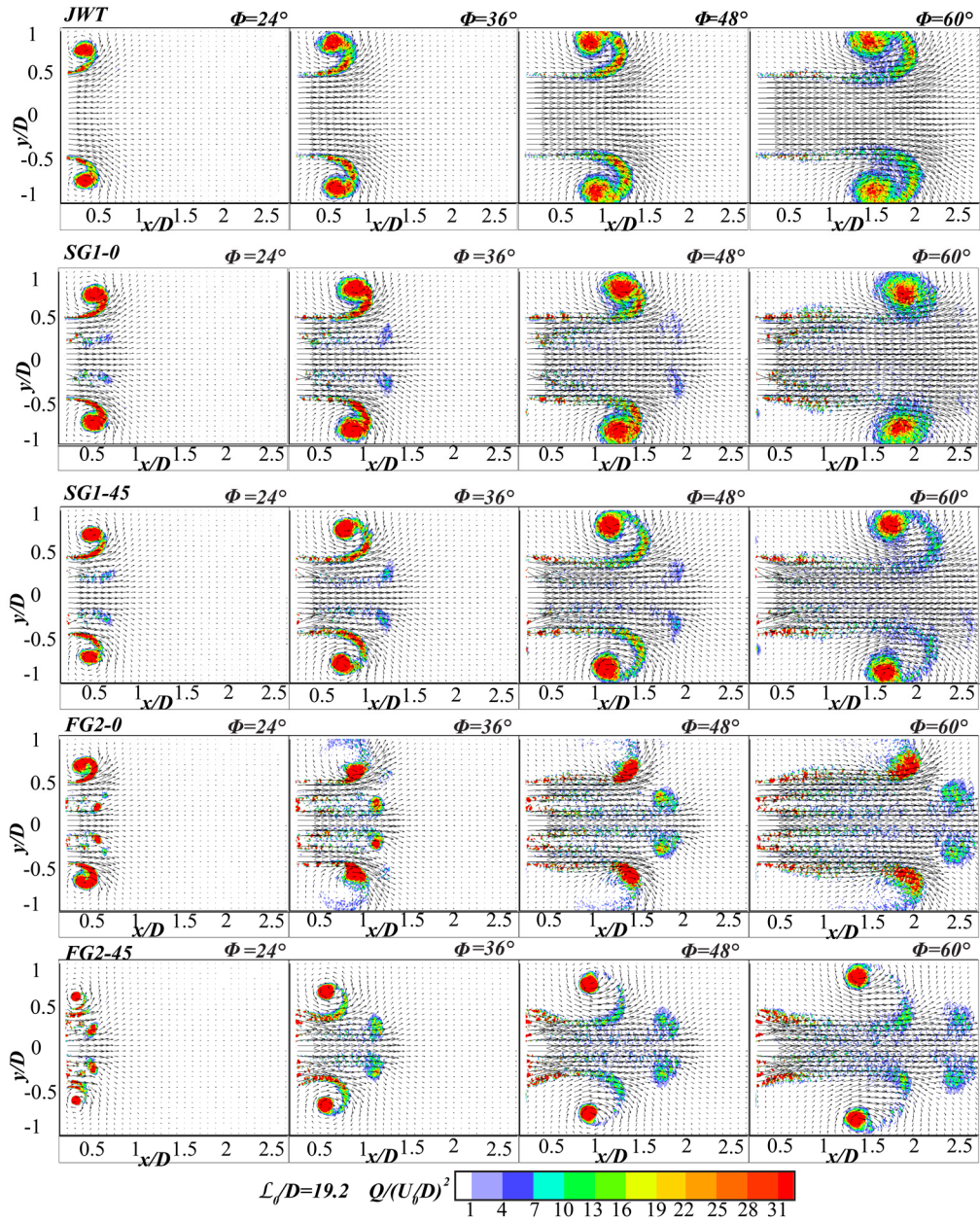


Fig. 5.17 - $Q > 0$ contour maps superimposed with velocity vector fields (plotted each 10×10 points), for $L_0/D = 19.2$ (SFV camera).

Following [108] the maximum streamwise excursion experienced by the saddle point Δx_{sp} is evaluated within the whole suction period, where the saddle point is defined as the stagnation point dividing the suction flow from the ejection one and is

5. THE EFFECTS OF THE SECONDARY ITERATIONS BARS ON SYNTHETIC TURBULENT JETS

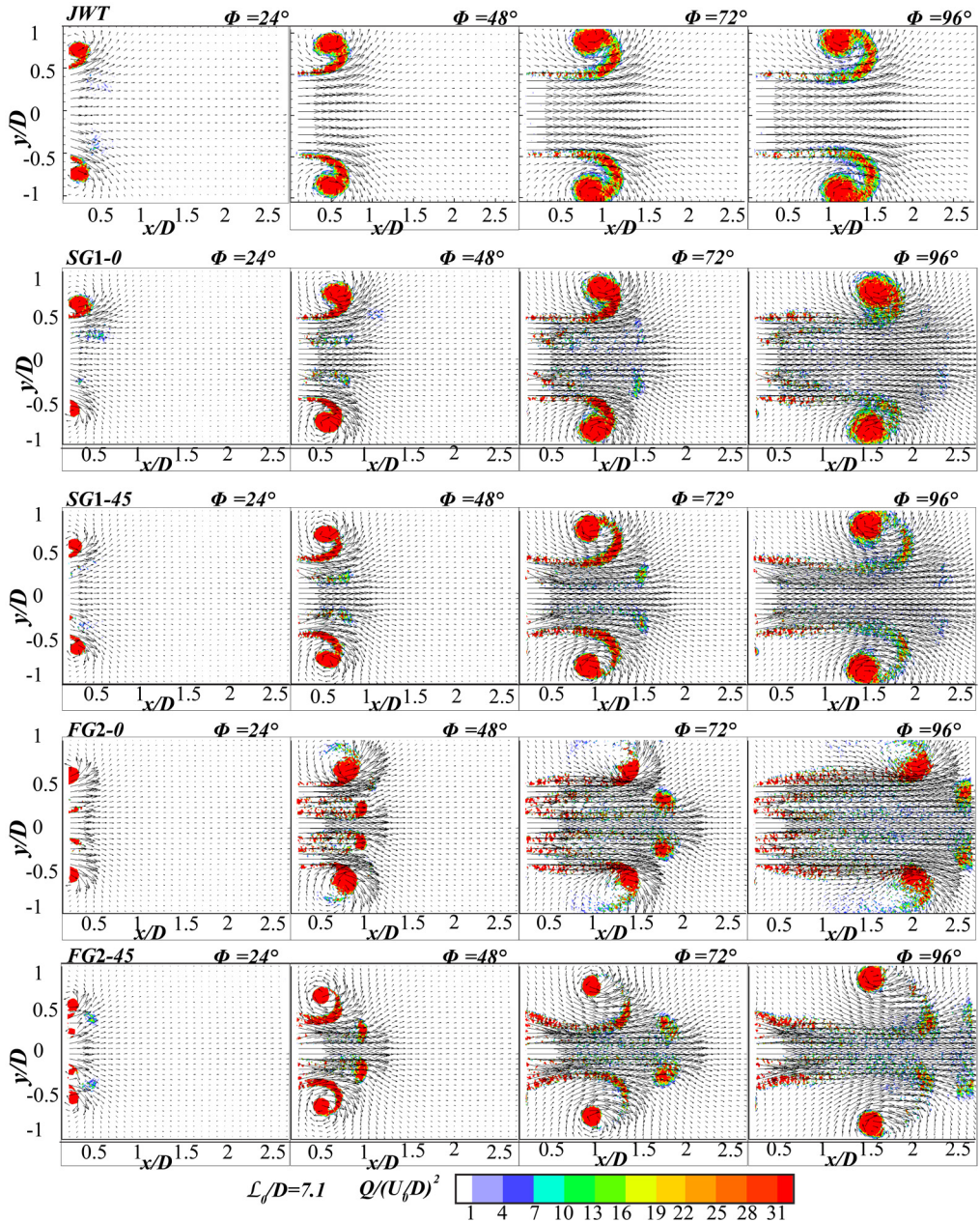


Fig. 5.18 - $Q > 0$ contour maps superimposed with velocity vectors (plotted each 10×10 points), for $L_0/D = 7.1$ (SFV camera).

represented by the white spot in Fig. 5.19. This is of interest if the synthetic jet devices are used as coolers because in this case, during the suction period, the device could ingest air coming from the target hot plate and this could deteriorate its convective heat transfer properties. No significant differences are found when

5.3. PHASE-AVERAGED FLOW FIELDS

comparing the three tested configurations, (see Fig. 5.19) and an almost linear increase of Δx_{sp} with \mathcal{L}_0/D is observed.

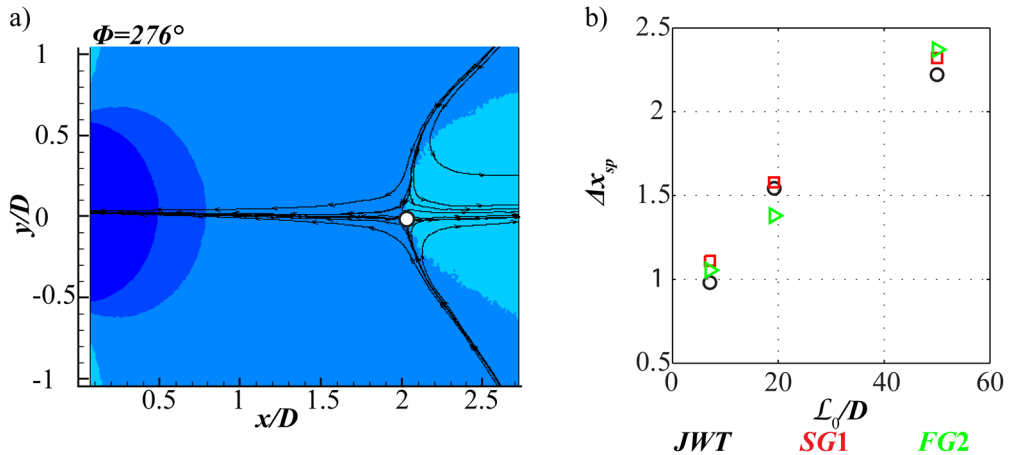


Fig. 5.19- a) Examples of saddle point; b) Maximum streamwise excursion experienced by the saddle point, Δx_{sp} .

It has been shown ([1, 4] and §6.3) that the continuous impinging turbulent jets equipped with the *FG2* produce an increase of the Nu at the stagnation point, Nu_0 , with respect to the *SG1* and the *JWT* for $x/D \leq 7$ and $x/D \leq 4$, respectively. In particular, the authors showed that, for $x/D = 2$, the enhancement in Nu_0 due to the *FG2* is maximum and equal to 40% with respect to the *SG1* and to 63% with respect to the *JWT*. If this enhancement should also hold for the analysed synthetic jet device equipped with this grid, it would be not possible to benefit of its maximum efficiency, at least for the highest \mathcal{L}_0/D value because the saddle point would reach the plate. Of course, convective heat transfer measurements on the flow developed by impinging synthetic jet device equipped with the *FG2* must be carried out to confirm these hypotheses.

In this regard, further information could be obtained by looking at the phase-locked $\langle tke \rangle$ contour maps reported in Fig. 5.20-22. For each dimensionless stroke-length \mathcal{L}_0/D , two different phases, in which the CVSs are respectively located close to the nozzle or far from it, are shown. High $\langle tke \rangle$ values can be detected across the trailing jet shear layer and within the cores of the developed CVSs. Moreover, as for continuous jets, regions of high velocity fluctuations levels are also represented by the grids' bars wakes.

For each device configuration the maps show that, according to the reduction of the jet stroke length, a decrease in \mathcal{L}_0/D corresponds to more localized and higher

5. THE EFFECTS OF THE SECONDARY ITERATIONS BARS ON SYNTHETIC TURBULENT JETS

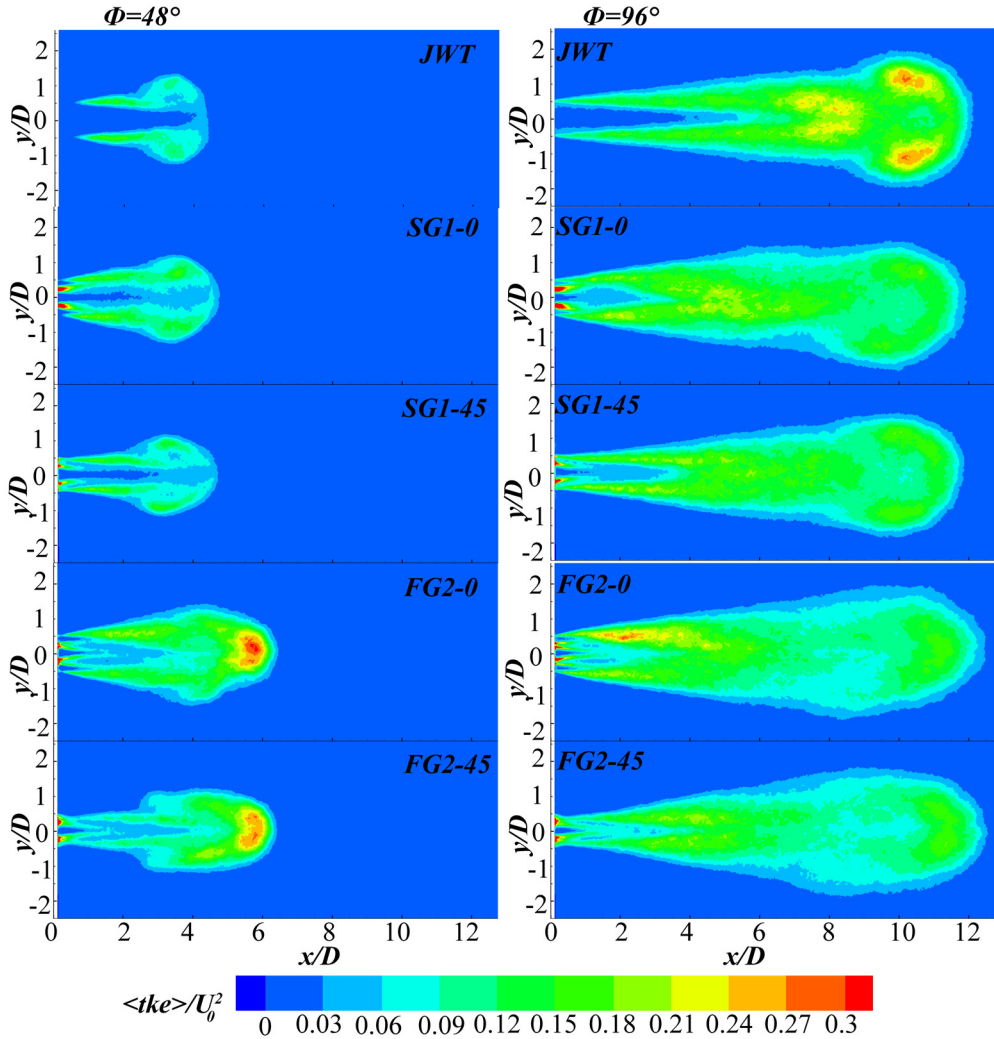


Fig. 5.20 - Phase-averaged $\langle tke \rangle$ maps at $L_0/D = 50.0$.

$\langle tke \rangle$ values. Focusing on $L_0/D = 50.0$ and for the *JWT* case, according to [106], it can be observed that as ϕ increases a wider region of high $\langle tke \rangle$ values develops with the $\langle tke \rangle$ peaks moving from the trailing jet shear layer to the vortex ring. A different scenario is found if the SG1 is inserted since the velocity fluctuations, in the ejection phase, reach their maxima in the bars' wakes. Moreover, for both the ejection and the suction phases, wider regions of nonzero velocity fluctuations and a faster shear layer spreading can be detected with respect to the *JWT* configuration. A stable $\langle tke \rangle$ peak located in the bars' wakes and an even faster shear layer development is visible in the FG2 configuration. Finally, for $\phi = 48^\circ$, a second region of significant high $\langle tke \rangle$ values, associated with the

5.3. PHASE-AVERAGED FLOW FIELDS

aforementioned inner CVS, develops in front of the outer CVS whilst it dissipates for $\phi = 96^\circ$.

The same conclusions drawn for $\mathcal{L}_0/D = 50.0$ are still valid for $\mathcal{L}_0/D = 19.2$, with the increase in the number of iterations causing wider regions of nonzero velocity fluctuations. It is interesting to note the different evolution of the $\langle tke \rangle$ along the two measurement planes both in the trailing jet shear layer and in the CVSs, above all in the *FG2* case. This difference is emphasized with the decrease in \mathcal{L}_0/D . All the maps suggest that, as for continuous jets, the fractal grids are significantly efficient turbulators close to the nozzle exit section while the interference between grid-generated turbulence and the vortices developed at the orifice edges reduces the turbulence level of CVSs' core at large distances from the grid.

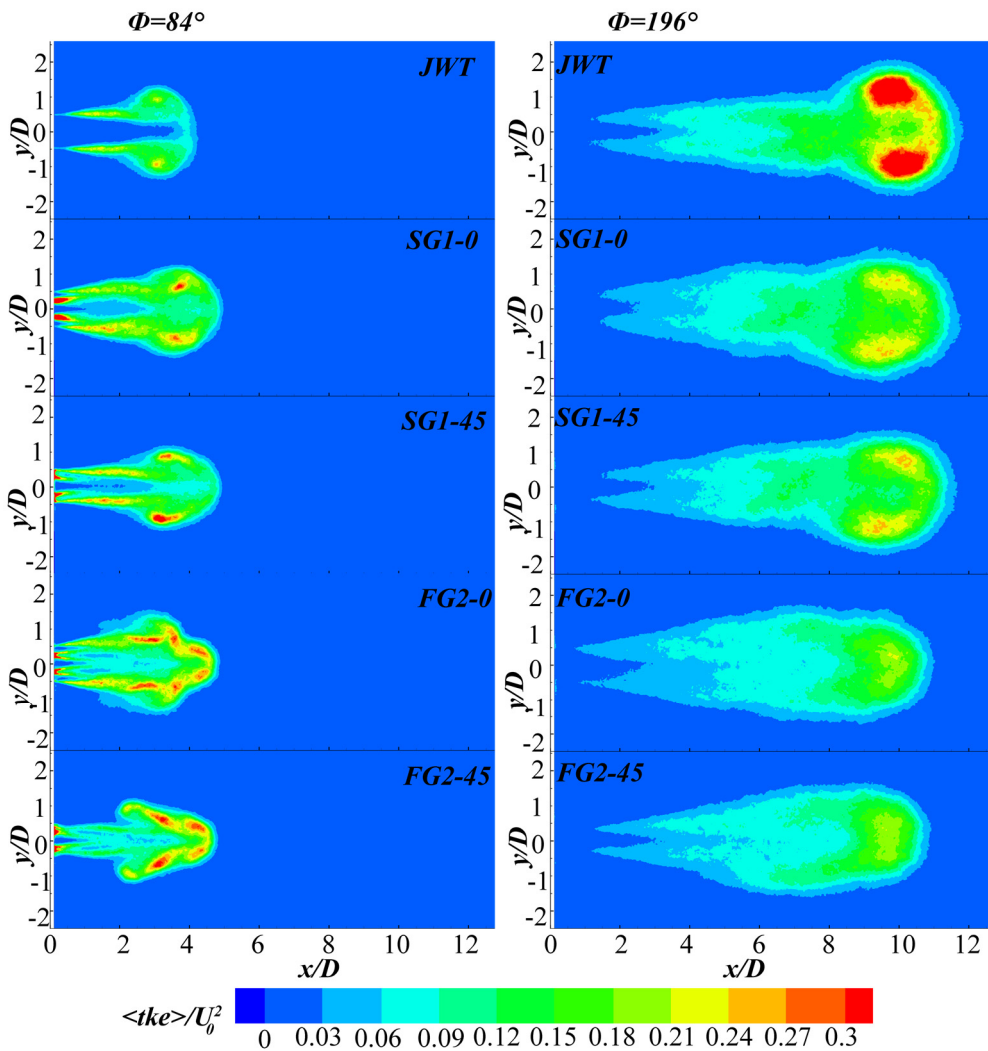


Fig. 5.21 - Phase-averaged $\langle tke \rangle$ maps at $\mathcal{L}_0/D = 19.2$.

5. THE EFFECTS OF THE SECONDARY ITERATIONS BARS ON SYNTHETIC TURBULENT JETS

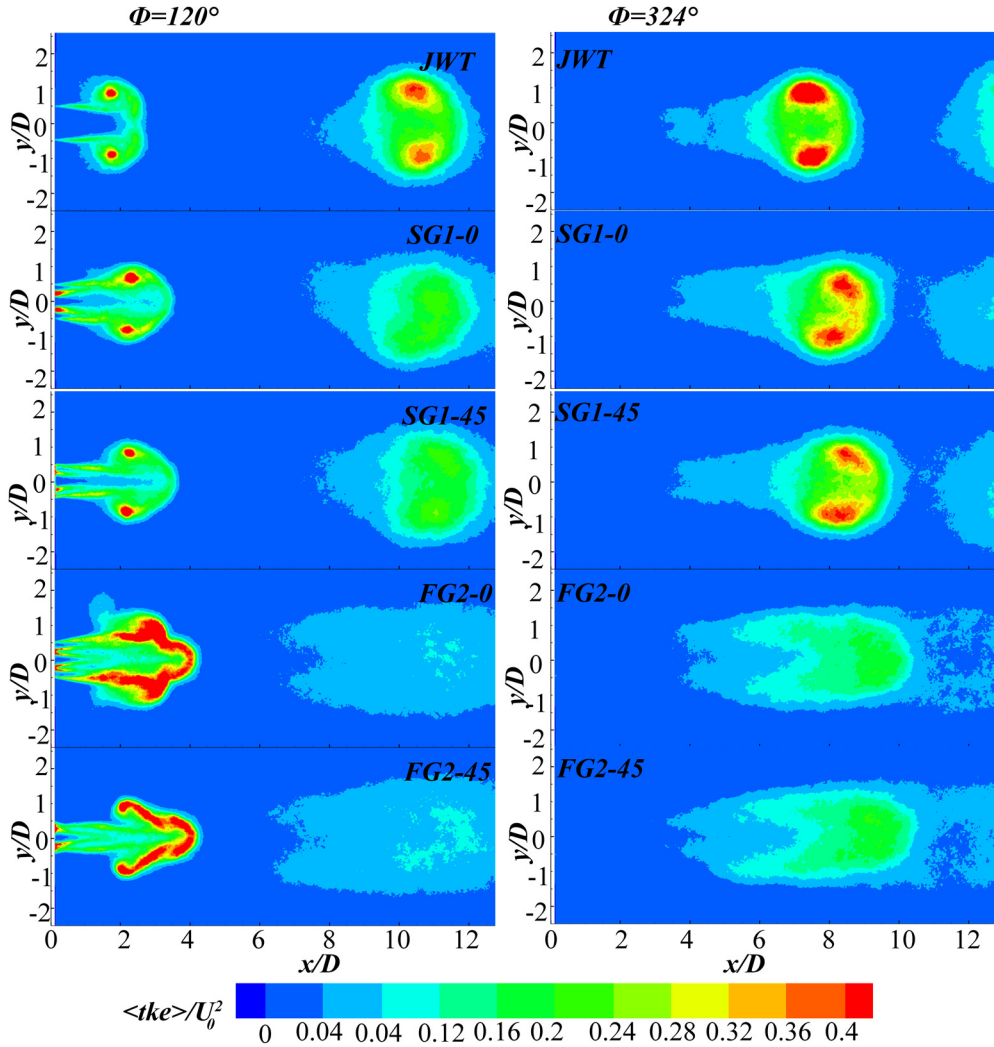


Fig. 5.22 - Phase-averaged $\langle tke \rangle$ maps at $L_0/D = 7.1$.

5.4. MAIN CONCLUSIONS

In this chapter, the effects due to both a 3-iteration square fractal grid and a single square grid on the flow field of round synthetic jets have been experimentally investigated by means of planar PIV. Measurements are carried out at a fixed Reynolds number equal to 6,700 and for three different dimensionless stroke lengths L_0/D equal to 50.0, 19.2 and 7.1.

The main results are here summarised:

5.4. MAIN CONCLUSIONS

- a synthetic jet is formed for all the tested \mathcal{L}_0/D values and for all the tested exit section geometries;
- both the grids (above all the fractal one) are responsible for additional vortical structures downstream the 1st iteration bars which interact with the one generated at the nozzle edges causing its azimuthal deformation and forcing its breakdown;
- the phase-averaged *tke* maps show that, as for continuous jets, the fractal grids are extremely efficient turbulators only at short distances from the nozzle;
- the turbulent jet developed past the fractal grid is less influenced by the actuation frequency: a stable peak in the mean axial velocity profile and a local maximum of the axial velocity fluctuations are found at $x/D = 0.9$ and $x/D = 1.6$, respectively, despite the stroke length.

6. EFFECT OF THE GRID GEOMETRY ON THE CONVECTIVE HEAT TRANSFER OF IMPINGING JETS

In this chapter², the effect of the grid geometry on the convective heat transfer properties of impinging jets is analysed by means of IR Thermography measurements. Both the influence of the secondary iterations bars and of the bars' thickness are experimentally investigated under the same power input (refer to §3.2.2 for a description of the used setup). The comparison is carried out in terms of both spatial averaged and local convective heat transfer. Moreover, the effect of the grid geometry onto the convective heat transfer uniformity is investigated.

6.1. INTRODUCTION

The convective heat transfer features of all the grids described in Table 3.1 are evaluated by analysing 1,000 images, collected at a frame rate of 100 Hz by means of an IR camera, and using the heated thin foil heat flux sensor (see §2.2.4). For each configuration, 13 nozzle-to-plate distances, equally spaced between $x/D = 1$ and 7, have been analysed.

The obtained convective heat transfer values are presented in non-dimensional form in terms of the Nusselt number spatial distribution Nu and area-averaged profiles $\overline{Nu}(r)$, where:

$$\overline{Nu}(r) = \frac{1}{\pi r^2} \int_0^r \int_0^{2\pi} Nu(\xi, \zeta) \xi d\zeta d\xi \quad (6.1)$$

Furthermore, similarly to what already done in [109], in order to assess the effect of the geometric parameters on the uniformity of the convective heat transfer rate, the spatial variance of the Nusselt number, $\sigma_{Nu}(r)$:

$$\sigma_{Nu}(r) = \frac{\sqrt{\frac{1}{\pi r^2} \int_0^r \int_0^{2\pi} (Nu(\xi, \zeta) - \overline{Nu}(\xi))^2 \xi d\zeta d\xi}}{\overline{Nu}(r)} \cdot 100 \quad (6.2)$$

is also reported.

The effects of the secondary iterations are assessed by comparing the performances of the square fractal grids (FG1-4) with those of the single square grids

² Contents in this chapter can also be found in [4].

6.2. HEAT TRANSFER SPATIAL DISTRIBUTION: MAIN FEATURES

(SG1-2). As already reported, the experiments are carried out under the same power input, i.e. the same product of the volumetric flow rate times the pressure drop across the grid, that turns into different Reynolds numbers (see Table 3.2) because of the different blockage ratios of the *FGs* with respect to the *SGs*. It is worth to notice that this choice allows to make comparisons in a way useful for engineering applications.

6.2. HEAT TRANSFER SPATIAL DISTRIBUTION: MAIN FEATURES

The Nusselt number maps related to the four fractal grids as a function of the grid bar thickness t_r is reported in Fig. 6.1 at three different nozzle-to-plate distances, namely $x/D = \{2, 4, 7\}$.

At $x/D = 2$ all the maps show qualitatively the same behaviour: the grid imprint onto the impinging plate is reflected in five regions of maxima, which must be addressed to the five *sub-jets* issuing through the fractal grid's holes. Four regions of local minima are also visible along the grid's diagonals. These regions must be addressed to the presence of counter-rotating wall vortices that produce a local upwash to the fluid, thus causing a low convective heat transfer rate region (refer to [3] for a more detailed discussion). As the nozzle-to-plate distance increases, the grid imprint is less visible. Indeed, as also seen when discussing the flow field features of turbulent jets equipped with fractal grids, the outer jets are rapidly smeared out due to turbulent diffusion. At $x/D = 7$ the convective heat transfer rate maps lose the asymmetry introduced by the grid as the flow fields progressively approach the *JWT* one.

The Nusselt number maps of the reference fractal grid, the *FG2*, and of the *SG1* are reported for $x/D = \{2, 4, 7\}$ in Fig. 6.2. It is worth to notice that, despite the absence of the secondary iterations bars in the *SG1*, the two inserts show similar convective heat transfer features: a cross-shaped wall imprint is still visible in the *SG1* map, even if the maximum obtained in correspondence of the grid centre is significantly reduced. This must be addressed to the higher turbulence intensity level that can be achieved using the fractal insert with respect to the single square one. Moreover, the four regions of minima are still visible in the *SG1* configuration, thus suggesting that also in this case the near wall flow field is characterised by the presence of four counter-rotating vortices which produce a local upwash to the fluid. The differences between the two configurations are significantly reduced at $x/D = 7$ as the Nu distributions resemble the *JWT* one.

6. EFFECT OF THE GRID GEOMETRY ON THE CONVECTIVE HEAT TRANSFER OF IMPINGING JETS

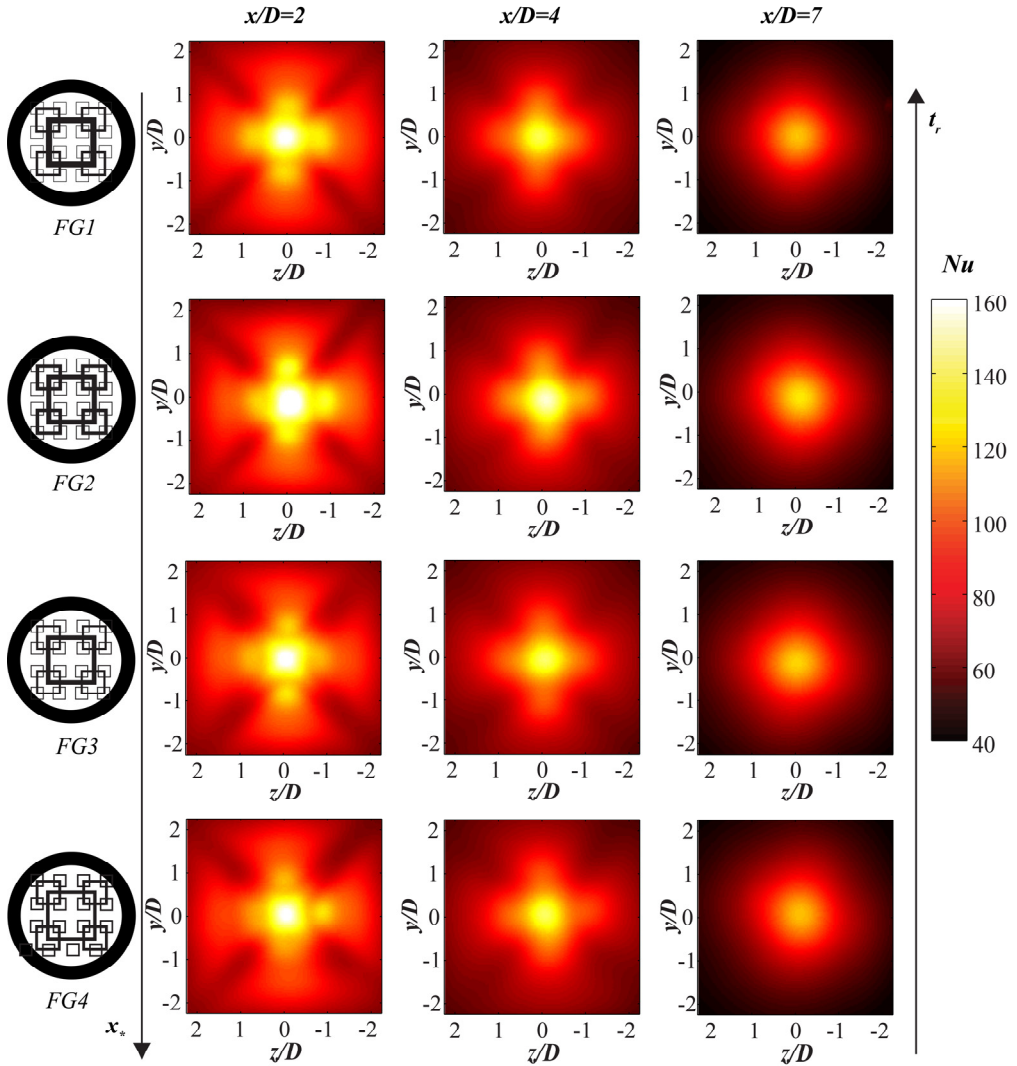


Fig. 6.1 - Nusselt number spatial distribution for the FGs: $t_r = \{6.25$ (FG1), 4 (FG2), 2.77 (FG3), 2.04 (FG4) $\}$ at three different nozzle-to-plate distances $x/D = \{2,4,7\}$.

6.3. AREA AVERAGED NUSSULT NUMBER PROFILES AND UNIFORMITY OF THE CONVECTIVE HEAT TRANSFER RATE

The area-averaged Nusselt number profiles \overline{Nu} along with the spatial variance profiles σ_{Nu} , for all the FGs, are reported in Fig. 6.3.

6.3. AREA AVERAGED NUSSELT NUMBER PROFILES AND UNIFORMITY OF THE CONVECTIVE HEAT TRANSFER RATE

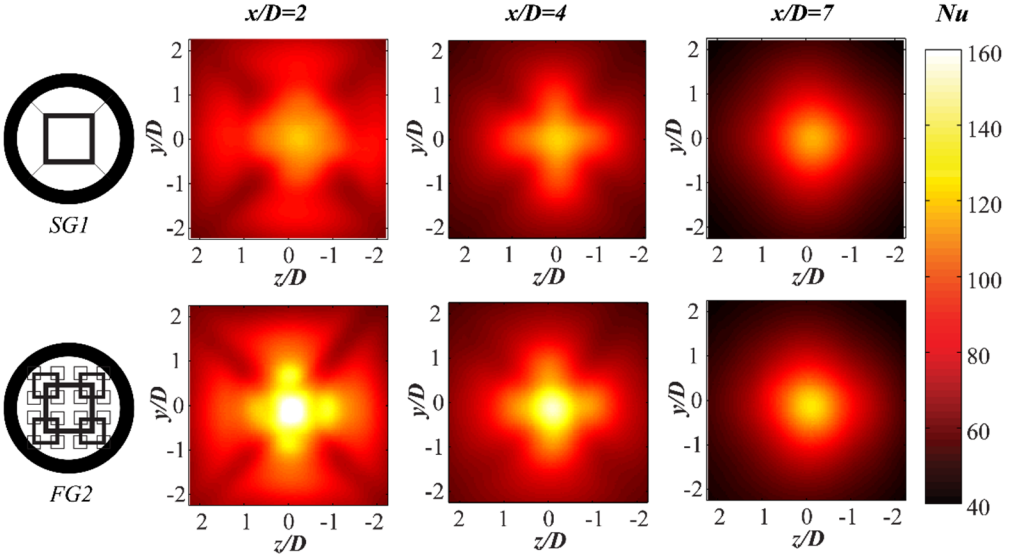


Fig. 6.2 - Nusselt number spatial distribution for the SG1 and FG2 at three different nozzle-to-plate distances $x/D = \{2,4,7\}$

The results show that the thickness ratio t_r affects both the stagnation point and the developing wall jet region Nusselt number. At short nozzle-to-plate distances, up to $r/D \approx 0.5$, a higher t_r is beneficial for the convective heat transfer rate. This is coherent with the fact that higher t_r values correspond to an anticipated turbulence peak (i.e. lower x_*/D values, as reported in Table 3.1; see also Fig. 7.5). Moreover, a lower t_r implies a higher uniformity, as the lowest σ_{Nu} is achieved for the lowest t_r value. This is directly related to the more uniform distribution of the grid blockage ratio: in the case of $t_r = 2.04$ a weaker contraction is imposed to the flow in correspondence of the nozzle axis with respect to the $t_r = 6.25$ case. Lower t_r values also imply higher area-averaged Nusselt numbers when both r/D and x/D increase. On one hand, it must be addressed to the larger momentum convected through the 1st iteration bars for higher t_r values (being the axial velocity higher) which leads to a momentum deficit for higher r/D locations. On the other hand, at lower t_r , as x/D increases, the more elongated turbulence production (due to the higher x_*/D) compensates for the axial velocity decay in the stagnation region (see also the following Fig. 7.5).

The stagnation point Nusselt number Nu_0 as a function of the nozzle-to-plate distances are reported in Fig. 6.4. Under the same flow rate and blockage ratio, the convective heat transfer rate is strongly influenced by the turbulence peak location (i.e. x_*/D). A smaller x_{peak} corresponds to a higher turbulence maximum.

6. EFFECT OF THE GRID GEOMETRY ON THE CONVECTIVE HEAT TRANSFER OF IMPINGING JETS

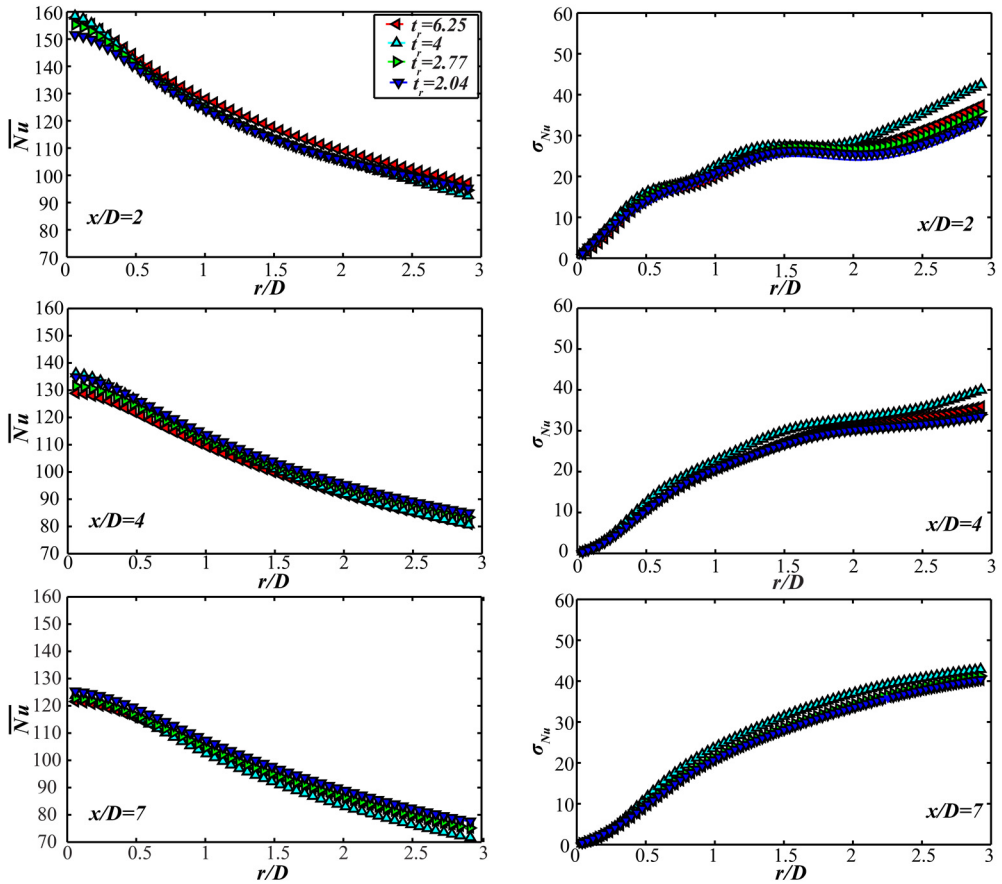


Fig. 6.3 - Area-averaged Nusselt number profiles and spatial variance of the Nusselt number as a function of the radial position at three nozzle-to-plate distances $x/D = \{2,4,7\}$ for the FGs: $t_r = \{6.25$ (FG1), 4 (FG2), 2.77 (FG3), 2.04 (FG4)}.

According to [2] x_{peak} is shifted upward with respect to the case of fractal-generated turbulence ($\approx 0.45x_*$) reported in [27] due to the effect of the penetrating shear layer onto the spreading wakes. As a consequence, for t_r equal to 4 and 6.25, the Nusselt number profiles monotonically decrease since both the axial velocity and the velocity fluctuations are decaying. On the other hand, for $t_r = 2.04$, Nu_0 increases from $x/D = 1$ to $x/D = 1.5$, since the turbulence production compensates for the axial velocity decay. Beyond that point, both the velocity fluctuations and the axial velocity decay, thus leading to the monotonic decrease in the Nusselt number profile. The dependence on t_r is visible up to $x/D \approx 2.5$ as beyond this point all the Nu_0

6.3. AREA AVERAGED NUSSLETT NUMBER PROFILES AND UNIFORMITY OF THE CONVECTIVE HEAT TRANSFER RATE

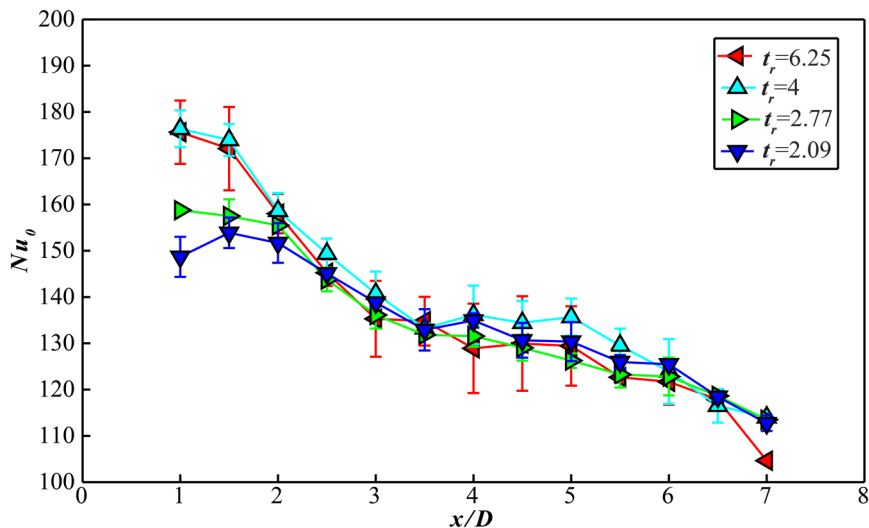


Fig. 6.4 - Stagnation point Nusselt number profiles as a function of the nozzle-to-plate distances x/D for the FGs: $t_r = \{6.25$ (FG1), 4 (FG2), 2.77 (FG3), 2.04 (FG4) $\}$.

show a similar behaviour. A plateau region can be detected for $3.5 < x/D < 5.5$. It must be addressed to the contribution of the penetrating shear layer towards the centreline which compensates the grid turbulence decay [2]. Finally, for $x/D > 5.5$ the effect of the shear layer is not able to compensate for the axial velocity decay causing a further change in the Nu_0 slope, which progressively approaches the power-law decay characterising the *JWT* case [67].

The effects of the iterations on the convective heat transfer rate and its uniformity are investigated by comparing the reference *FG2* with respect to the *SGs* as a function of the radial position r/D and for different nozzle-to-plate distances, $x/D = \{2, 4, 7\}$, as shown in Fig. 6.5. The contributions of the holding bars have also been analysed.

The σ_{Nu} profiles related to the two *SGs* agree quite well, thus suggesting no significant effect of the holding bars onto the convective heat transfer rate distribution are present. Independently of the nozzle-to-plate distance, Nu_0 always reaches higher values in the *FG2* case than in the *SGs* ones. Particularly sensitive is the increase for $x/D = 2$ as the *FG2* attains values that are about 40% larger than the intensity levels related to the *SGs*. On one side, this must be ascribed to the larger turbulence levels reached by means of the *FG2* and, on the other side, to the higher capability of the *FGs* in producing streamwise vorticity which leads to a strong enhancement of the entrainment rate and, as consequence, of the scalar transfer. These differences are smeared out at higher x/D values. In particular, at $x/D = 7$ the \overline{Nu} profiles related to the *SGs* and the *FG2* are practically equivalent. However,

6. EFFECT OF THE GRID GEOMETRY ON THE CONVECTIVE HEAT TRANSFER OF IMPINGING JETS

higher uniformity levels are always reached by using the SGs, independently on the x/D location.

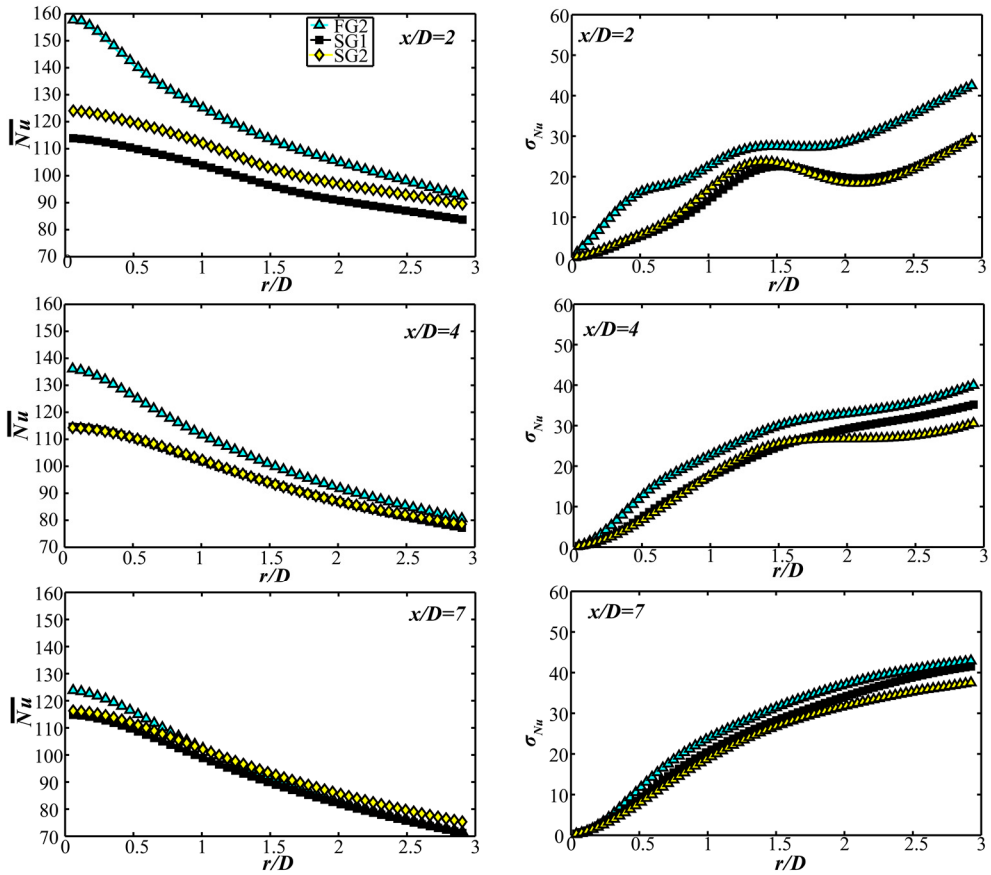


Fig. 6.5 - Area-averaged Nusselt number profiles and spatial variance of the Nusselt number as a function of the radial position at three nozzle-to-plate distances $x/D = \{2,4,7\}$ for the FG2 and the SGs.

The effect of the nozzle-to-plate distance on Nu_0 for the FG2 and both the SGs is shown in Fig. 6.6. The profiles clearly point out the key-role that the grid's secondary iterations play on the convective heat transfer process. Indeed, in the SGs cases, Nu_0 remains almost constant up to $x/D = 6$ and then decreases. In the FG2 case, as already said, a plateau region is present for $3.5 < x/D < 6$ because the penetrating shear layer has a direct effect on the heat transfer rate; for $x/D > 6$ the curve approaches the SGs' ones.

6.4. MAIN CONCLUSIONS

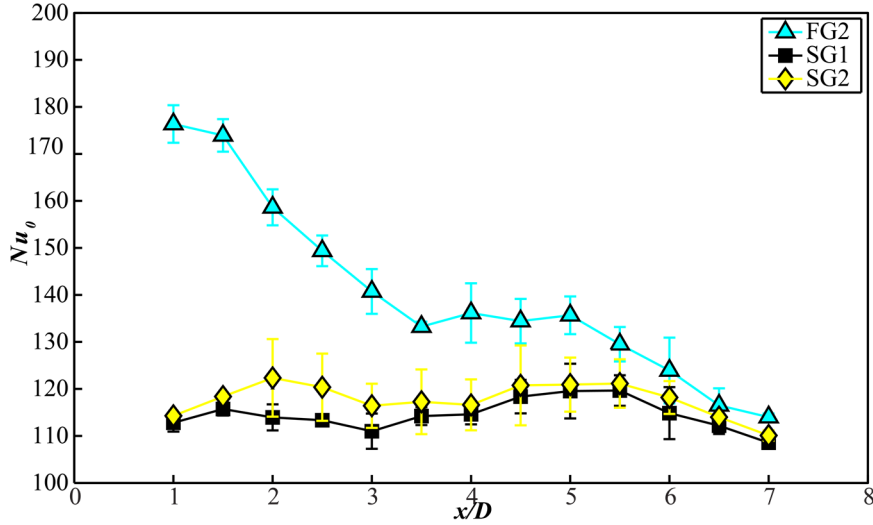


Fig. 6.6 - Stagnation point Nusselt number profiles as a function of the nozzle-to-plate distance x/D for the FG2 and the SGs.

6.4. MAIN CONCLUSIONS

In this chapter, the effect of the fractal geometry on the convective heat transfer rate of turbulent continuous jets equipped with fractal grids is assessed by means of IR Thermography measurements.

The main outcome of the investigation is:

- the introduction of the secondary iterations to single square grids significantly increases the convective heat transfer rate while significantly reduces the uniformity of the Nusselt number maps;
- the increase of the bars' thickness ratio in fractal square grids characterised by the same blockage ratio and bars' length causes an increase of the convective heat transfer rate but less uniform Nusselt number distributions;
- the effect of the secondary iterations (and more generally, of the turbulators) on the convective heat transfer rate is significantly reduced at large nozzle-to-plate distances.

7. EFFECT OF THE GRID GEOMETRY ON THE CONTINUOUS JET FLOW FIELD

In this chapter, the effects of the bar thickness of square-fractal grids on the flow field of turbulent jets are investigated. Four 3-iterations square fractal grids, having the same blockage ratio and L_0 but different t_0 , are located at the exit section of a short-pipe nozzle: the resulting flow fields are analysed and compared with those obtained by inserting a regular grid characterised by the same blockage ratio and effective meshlength. Moreover, the jet flow developing past two single square grids, that only differ for the holding bars, is studied. All the measurements are performed at a fixed Reynolds number, $Re \approx 16,000$, and the results are compared with the axisymmetric turbulent jet, reported as reference.

7.1. MEAN FLOW FEATURES

For each of the grids introduced in Table 3.1, 6,000 instantaneous PIV realizations are acquired, both along the 0° and the 45° direction, in order to assess the streamwise evolution of the flow field. 6,000 instantaneous flow fields are also evaluated for the *RG* and the *JWT* configurations. The reader can refer to §3.2.2 for details about the experimental apparatus and cross-correlation process.

Fig. 7.1, Fig. 7.2 and Fig. 7.3 report the time-averaged axial velocity contour maps related to the *SGs*, the *FGs* and the *RG*, respectively. It is worth to notice that, in order to reduce the measurement noise, their values are averaged with respect to the plane of symmetry.

Fig. 7.1 points out that the effects related to the different holding bars can only be appreciated close to the nozzle exit section, as they affect the recirculation regions' evolution, while no significant differences can be observed in the axial velocity values, consistently with their equal blockage ratio. On the other hand, according to their higher σ values (which is almost thrice the blockage ratio of the single square grids), all the maps relative to the *FGs* (see Fig. 7.2) are characterised by higher velocity values with respect to the *SGs* ones. As expected, the different bars' thickness influences the jet evolution close to the nozzle exit section, so that, in the 0° -maps, higher t_0 values correspond to wider recirculation regions past the 1st iteration bars. On the other hand, less amount of fluid moves through the secondary iterations squares (refers to the 45° -maps in Fig. 7.2). Therefore, a more uniform axial velocity distribution can be observed for decreasing t_r values (as also suggested

7.1. MEAN FLOW FEATURES

by the σ_{Nu} profiles reported in Fig. 6.3) because of a weaker contraction imposed to the flow in correspondence of the nozzle axis. Moving downstream, the jet loses memory of the grid geometry and no significant difference between the maps can be perceived for $x/D > 6$, justifying the similar Nu maps reported in Fig. 6.1 for $x/D = 7$ and the collapse of the Nu_0 profiles in Fig. 6.4 for $x/D > 6$.

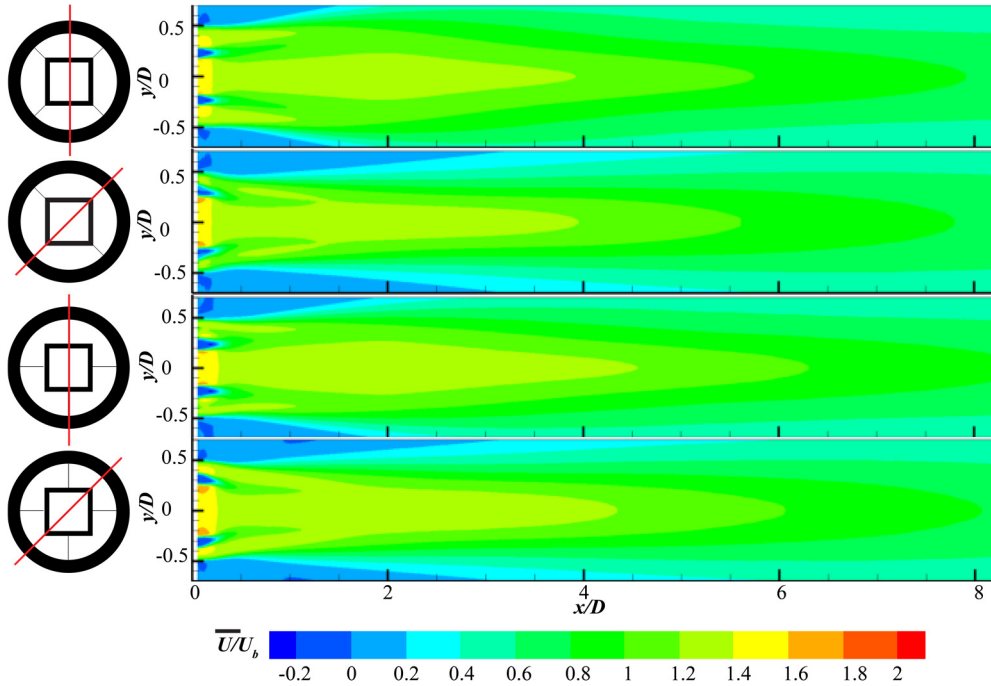


Fig. 7.1 - Time-averaged axial velocity component contour maps related to the SGs.

Fig. 7.3 reports the time-averaged axial velocity contour maps past the *RG*. Since the laser sheet intersects along one of the grid's bar, an initial velocity defect can be detected. As x/D increases, the axial velocity is recovered; moreover, a more elongated potential-core like region can be observed with respect to the *JWT* (whose time-averaged axial velocity map is not here reported for the sake of brevity: the reader can refer to §4.1, as no significant differences on the flow field morphology emerge for the two different Reynolds numbers). For $x/D < 2.5$, the highest axial velocity values are located at the interface between the potential-core like region and the penetrating shear layer.

The time-averaged axial velocity profiles, evaluated along the centreline, for all the analysed grids are shown in Fig. 7.4, together with the results related to the *JWT*. As already discussed in Chapter 4, both the single- and the fractal-square grids cause

7. EFFECT OF THE GRID GEOMETRY ON THE CONTINUOUS JET FLOW FIELD

a significant increase of the mean axial velocity suddenly past the grid, with respect to the *JWT* and the *RG*.

Both the \bar{U}/U_b *SGs* profiles attain values of about 1.5 at $x/D = 0.05$, (i.e. the first point of the measurement domain) because of the grid presence, however higher \bar{U}/U_b values than the *JWT* ones, along the centreline, can be just detected up to $4D$ and $4.65D$ from the nozzle exit section, respectively for the *SG1* and the *SG2*.

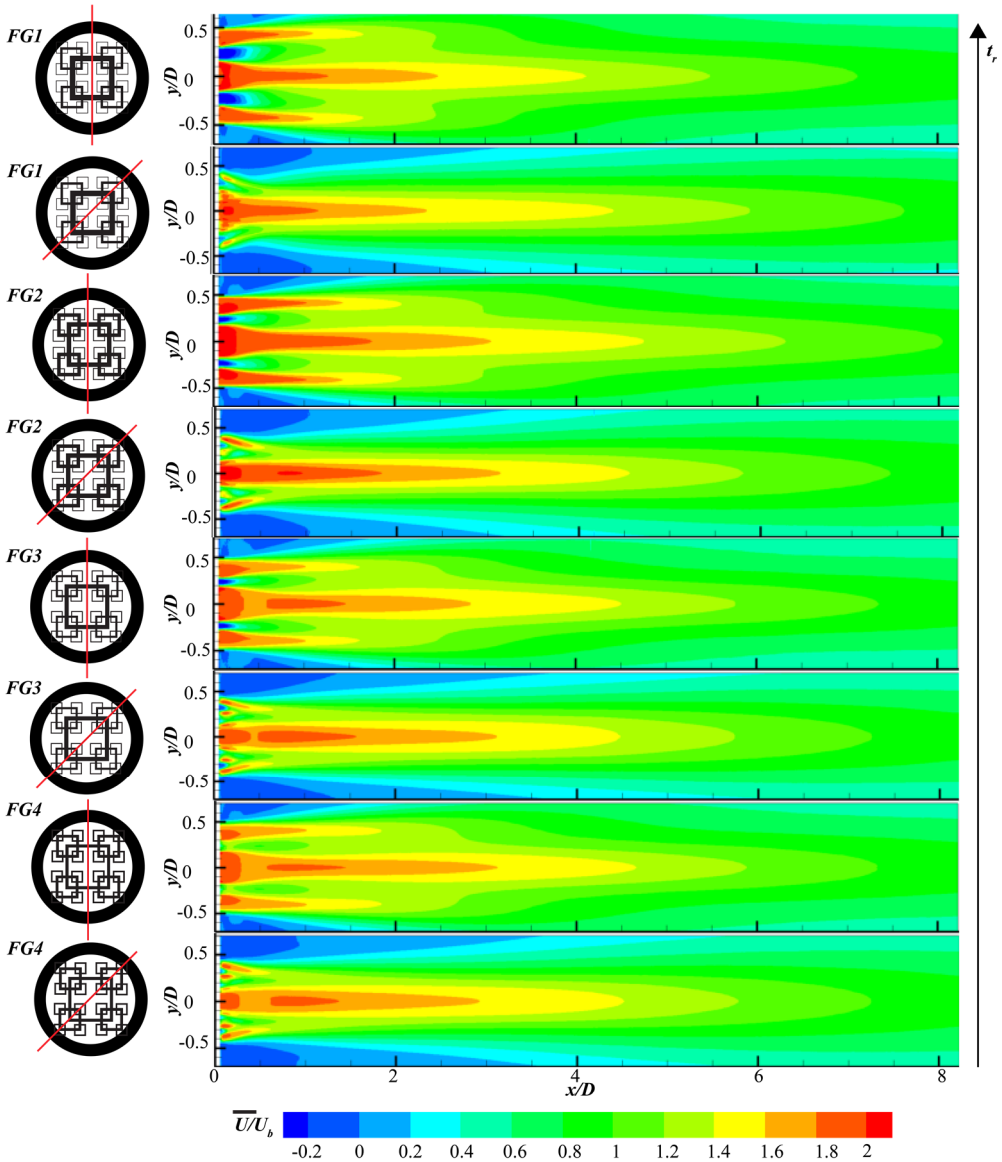


Fig. 7.2 - Time-averaged axial velocity component contour maps related to the *FGs*.

7.1. MEAN FLOW FEATURES

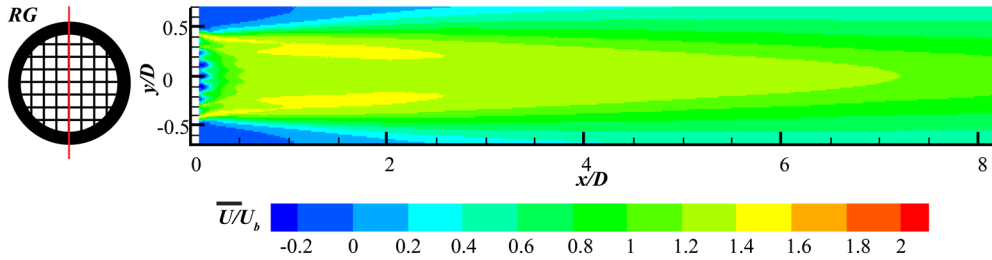


Fig. 7.3 - Time-averaged axial velocity component contour map related to the RG.

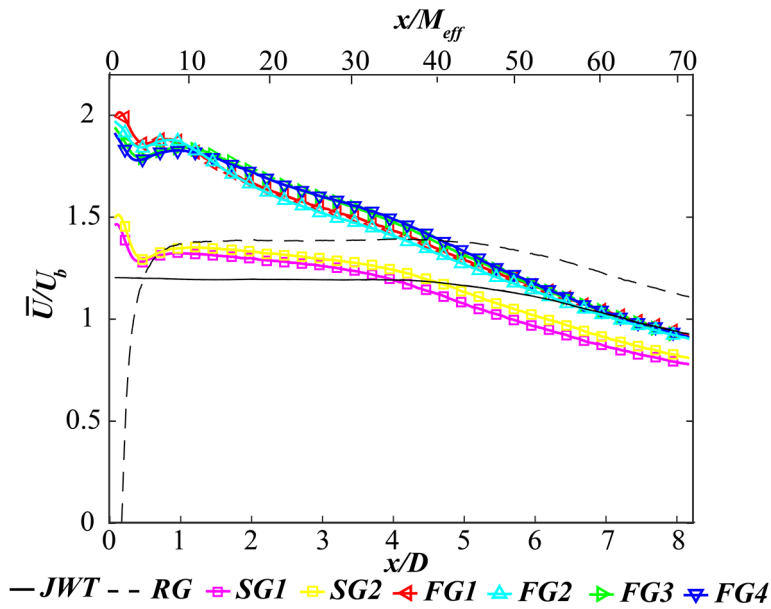


Fig. 7.4 - Time-averaged axial velocity profile \bar{U}/U_b evaluated along the centreline.

The length of the measurement domain is, probably, not large enough for the complete jet development past both the *SG1* and the *SG2*. Therefore, the velocity profiles do not recover the behaviour of the *JWT* flow field. It is the author's opinion that the slight discrepancies between the *SG1* and *SG2* profiles reported both in Fig. 7.4 and Fig. 7.5 are due the experimental uncertainty of the measurements.

The increase of t_r from 2.04 to 6.25 in the *FGs* causes an increase of the mean axial velocity at short distances from the nozzle, because of the larger momentum convected through the 1st iteration square. On the other hand, for $1.5 < x/D < 7$, the highest velocity is reached by means of the *FG4* (i.e. for the lowest t_r value). Finally, all the *FGs* curves practically collapse to the *JWT* one for $x/D > 7$.

Fig. 7.4 also shows that all the *SGs* and *FGs* profiles reach a local minimum at $0.4 < x/D < 0.5$, as already shown in Fig. 4.7 for the *FG2*. This initial reduction of

7. EFFECT OF THE GRID GEOMETRY ON THE CONTINUOUS JET FLOW FIELD

the mean streamwise velocity could be associated with a *vena contracta* effect, according to results reported in [91] for sharp-edged orifice round and cruciform jets.

The *RG* mean axial profile strongly differs from the ones described above: as already suggested by the contour map (see Fig. 7.3), after an initial recovery, \bar{U}/U_b attains a constant value of about 1.4 for $1 < x/D < 5.5$ and it then decreases. Conversely to the *SGs* profiles, apart from the initial stage, \bar{U}/U_b always shows higher values than the *JWT*.

The axial and the radial velocity fluctuations evaluated along the centreline are reported in Fig. 7.5-a) and -b). According to [26, 27, 39] both the number of fractal iterations and the bars' thickness affect the turbulence production peak.

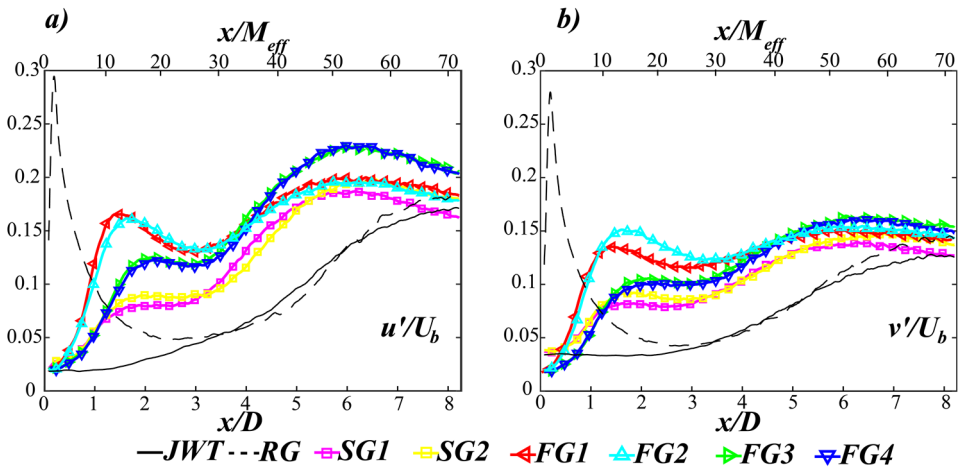


Fig. 7.5 - Time-averaged -a) axial velocity fluctuations u'/U_b evaluated along the jet centreline; b) radial velocity fluctuations v'/U_b evaluated along the jet centreline.

By looking at *SGs*' profiles a mild local maximum in the velocity fluctuations can be envisaged at $x/D \approx 2$, differently to the corresponding results discussed in Chapter 4 (see Fig. 4.7) and Chapter 5 (see Fig. 5.7), for $Re \approx 6,700$, thus confirming the influence of the Reynolds number in the wakes development downstream of the bars.

The comparison between the *SGs* and the *FG2* (i.e. the square fractal grid having same L_0 and t_0 values), shows that the increase in N not only causes a higher turbulence production close to the grid but also seems to involve lower x_{peak} values, according to the wind tunnel measurements reported in [39], for $1 \leq N \leq 3$. Unfortunately, the turbulence produced by the shear layer masks the real shape of the first local maximum preventing the certain assessment of the last observation. Additional measurements employing *SGs* are required in order to further confirm it.

7.2. LARGE SCALE ISOTROPY

The increase in t_r is responsible of a monotonic increase of the axial velocity fluctuations peak u'_{peak}/U_b , close to the grid, as also reported in [26, 27] for wind-tunnel experiments. Moreover, a monotonic decrease of its axial location, x_{peak} , can be observed with increasing t_r , according to [27]. On the other hand, for *FG2*, x_{peak} is not influenced by the global Reynolds number Re (at least for the two tested Re values) since, as in Chapter 4 and according to [2], it corresponds to $0.4x_*$. The same $x_{peak}/x_* \approx 0.4$ is also found for the *FG1* and the *FG3* whilst it attains a value of 0.35 for the *FG4* configuration.

The radial velocity fluctuations peak related to the grid, v'_{peak}/U_b , does not show the same monotonic increase with t_r (see Fig. 7.5-b)) so that a lower peak can be observed in the *FG1* with respect to the *FG2*.

For $x > x_{peak}$, the velocity fluctuations do not decay monotonically because of the development of the external shear layer, such that a second turbulence production region is visible. Fig. 7.5 shows that the axial location at which the shear-layer turbulence production overcomes the grid-turbulence decay depends on both N and t_r , so that lower N and t_r values anticipate this position. Moreover, for fixed N values, whilst the radial fluctuations profiles almost collapse for $x/D > 5$, significant differences can be observed in the axial fluctuations curves: the *FG4* curve shows an absolute maximum of u'/U_b at about $x/D = 6$ which is 15% higher than the corresponding peak related to the *FG1*.

Finally, Fig. 7.5 also shows the u'/U_b and the v'/U_b profiles related to the *RG*. As can be seen, it is capable to develop the highest turbulence level, at about $x/D = 0.2$ (i.e. $x/x_* = 0.31$), after which, initially both the velocity fluctuations components rapidly decay, following the power-law which is expected for regular-grid generated turbulence [24]. Even in this case a second region of turbulence production is detected for $x/D > 3$ where, on the contrary with respect to the *FGs* and the *SGs*, the profiles collapse on the *JWT* ones, thus suggesting most of the turbulence produced by the grid has already been dissipated. It is worth to notice that the use of the *RG* is advantageous, in terms of turbulence production, up to $1.4D$ with respect to the *SGs* and up to $1.3D$ for the *FG4*, value that goes down to $0.9D$ for the *FG1*.

7.2. LARGE SCALE ISOTROPY

In the following, the flow field large-scale isotropy is assessed by means of the *isotropy factor* u'/v' , which is clearly equal to one for an isotropic flow [73].

7. EFFECT OF THE GRID GEOMETRY ON THE CONTINUOUS JET FLOW FIELD

The *isotropy factor* maps related to the *RG*, and all the *SGs* and the *FGs*, both along the 0° and the 45° direction, are reported in Fig. 7.6. For the sake of brevity, and because of the symmetry with respect to the jet centreline, within the measurement plane, only the results related to half of the imaged area are reported.

Previous measurements of the *isotropy factor* in wind tunnel experiments showed that, along the centreline, in the wake of fractal grids, the isotropy factor is 1.1 – 1.2 [23, 28, 32], whilst Discetti et al. [33] and Sponfeldner et al. [46], reporting 2D maps of the isotropy factor, showed that it has not a uniform distribution in the crosswise direction because of the inhomogeneity of the grids' blockage ratio.

Inhomogeneous *isotropy factor* distributions are also shown in Fig. 7.6, particularly at short distances from the nozzle exit section, where both the contributions of the developing shear-layer and of the turbulators can be appreciated. According to [46], regions in which u'/v' gets values lower than 1 are found, above all in the *SGs* maps, while the introduction of the secondary iterations significantly reduces their area and involves values of *isotropy factor* much higher than 1 up to further downstream locations. As soon as the external shear-layer has reached the jet centreline, it is not possible to distinguish between the two different contributions, and a more uniform u'/v' distribution, in which the isotropic factor reaches values of about 1.3, can be observed. The higher value of u'/v' for similar downstream locations with respect to the results reported in [33, 46] are related to the turbulent jet phenomenology characterised by higher velocity fluctuations in the streamwise direction. In order to assess the effects of the bars thickness on the large-scale isotropy, two crosswise profiles have been extracted and plotted in Fig. 7.7 for each of the analysed device configurations, at $x/D = 0.5$ and 7, respectively. For the *JWT* case only the profile at $x/D = 7$ is reported as the transversal fluctuations get values close to zero at the shortest nozzle distance.

For the *RG*, at $x/D = 0.5$ (i.e. $x/M_{eff} \approx 4.4$), higher values of u'/v' can be observed at the jet boundaries, while the *isotropy factor* is approximately equal to 1.1 for $-0.35 < y/D < 0$ with an “oscillating-like profile” which is clearly due to the grid geometry.

At the shortest distance from the grid and referring to the *SGs*' profiles in Fig. 7.7, a strong inhomogeneity can be detected both along the 0° - and the 45° -measurement plane: values of about 1.2 and 1.4 can be observed at crosswise locations corresponding to the external shear layer respectively in Fig. 7.7-a) and Fig. 7.7-b).

On the other hand, these figures show minimum values of about 0.6 and 0.7 downstream the 1st iteration bars, according to the importance that the vortex shedding generated past the bars assumes in these flow fields. Moving towards the jet axis, u'/v' first increases and then decreases up to 0.75 on the jet axis.

7.2. LARGE SCALE ISOTROPY

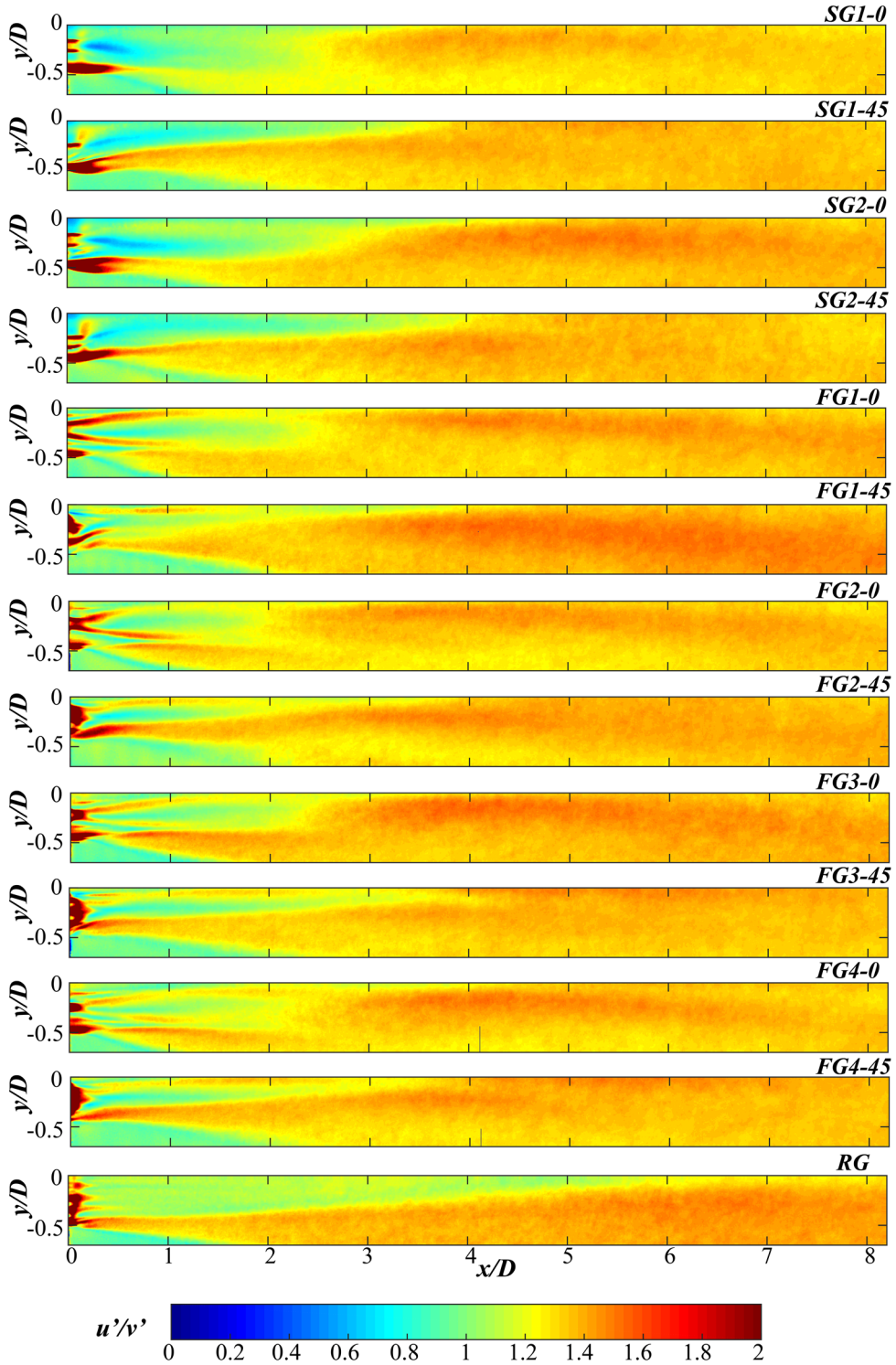


Fig. 7.6 - Isotropy factor maps u'/v' related to the SGs, the FGs and the RG.

7. EFFECT OF THE GRID GEOMETRY ON THE CONTINUOUS JET FLOW FIELD

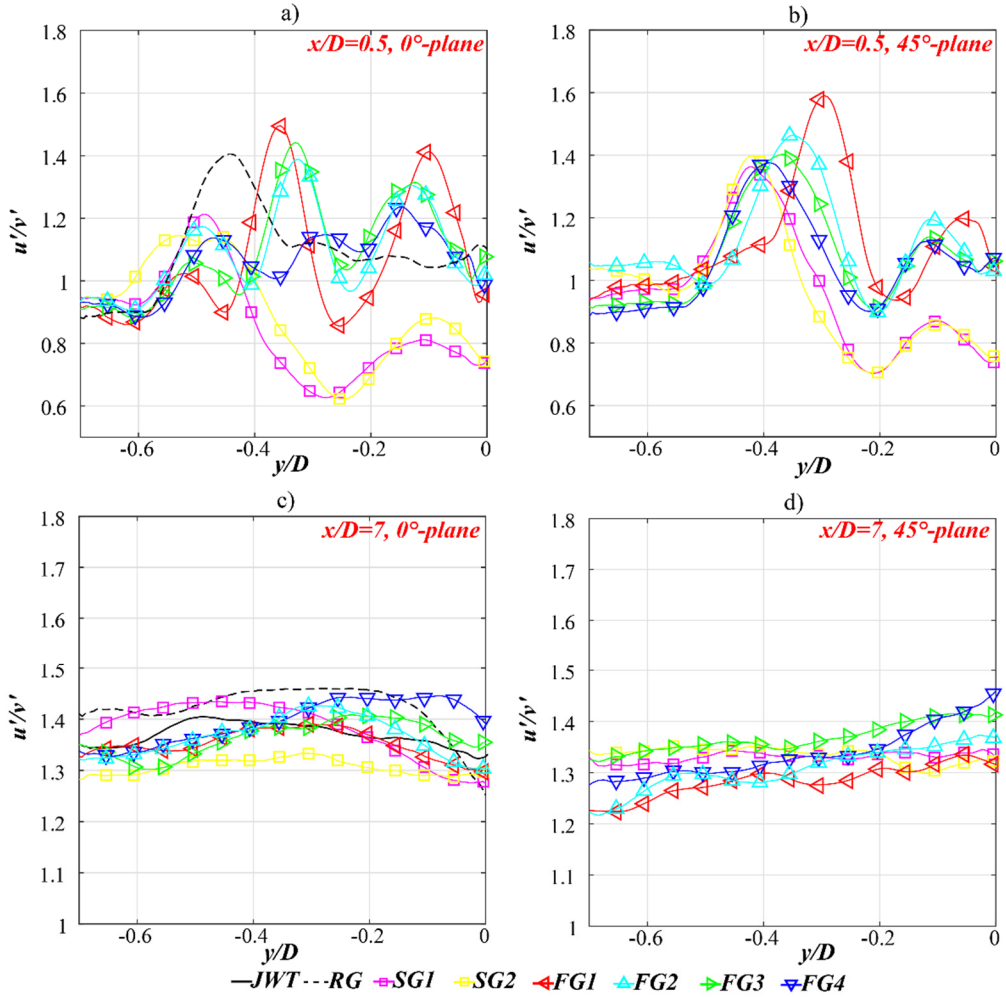


Fig. 7.7 - u'/v' crosswise profiles at: a) $x/D = 0.5$, along the 0° -plane, related to the SGs, the FGs and the RG; b) $x/D = 0.5$, along the 45° -plane, related to the SGs and the FGs; c) $x/D = 7$, along the 0° -plane, related to the SGs, the FGs, the RG and the JWT; d) $x/D = 7$, along the 45° -plane, related to the SGs and the FGs.

The introduction of the secondary iterations bars significantly increases the large-scale isotropy, as clearly shown by the profiles reported in Fig. 7.7-a) and Fig. 7.7-b) and according to [23, 46] in decaying grid-turbulence. These results also show that a key-role in the *isotropy factor* distribution is played by the bars' thickness ratio t_r . Indeed, along the 0° -direction, where the three-dimensionality of the flow can be easily detected by the u'/v' peaks which are not ascribable to the 1st iteration bars, it is evident that higher t_r values correspond to less uniform u'/v' distributions. In particular, for the smallest $t_r = 2.04$ (i.e. FG4), u'/v' ranges between 0.9 and 1.25 while it ranges between 0.9 and 1.5 for $t_r = 6.25$ (i.e. FG1). This result is also in

7.3. VELOCITY SPECTRA

line with ([4]; see also §6.3) where it is reported that a larger thickness ratio t_r is associated with higher localised convective heat transfer values, but less uniformity. A similar trend is also observed along the 45° -direction. Seven diameters downstream from the grid, where the external shear-layer has already reached the jet centreline, flatter u'/v' profiles are shown along both the two measurement planes, for all the investigated configurations. However, at this given downstream location, the less homogeneous FGs' profiles are those related to the lowest t_r value.

7.3. VELOCITY SPECTRA

The one-dimensional spectra evaluated along the axial direction of both the streamwise E_u and crosswise E_v velocity fluctuations have been analysed to get further information on the redistribution of the tke over the different spatial scales.

A first qualitatively description can be given by looking at the Fig. 7.8-11 that report the dimensional velocity spectra of both u and v for each crosswise location, both along the 0° - and the 45° - direction, respectively for the SGs , the $FG2$ and the RG . Not all the maps related to the other FGs are here reported for the sake of brevity; the wavenumber k is normalised with respect to the nozzle diameter D .

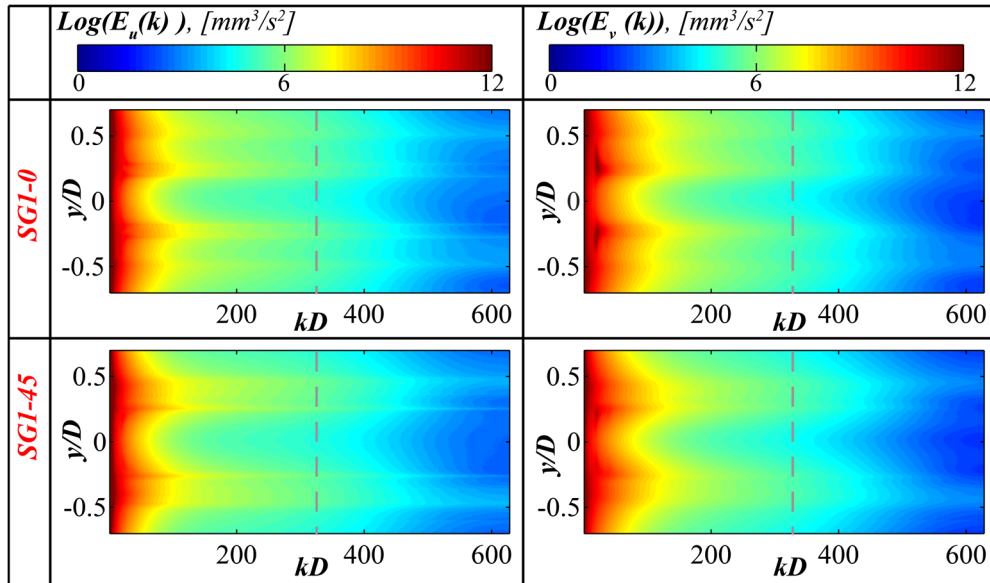


Fig. 7.8 - Velocity spectra of u (left) and v (right), related to the $SG1-0$ (top) and $SG1-45$ (bottom) configurations.

7. EFFECT OF THE GRID GEOMETRY ON THE CONTINUOUS JET FLOW FIELD

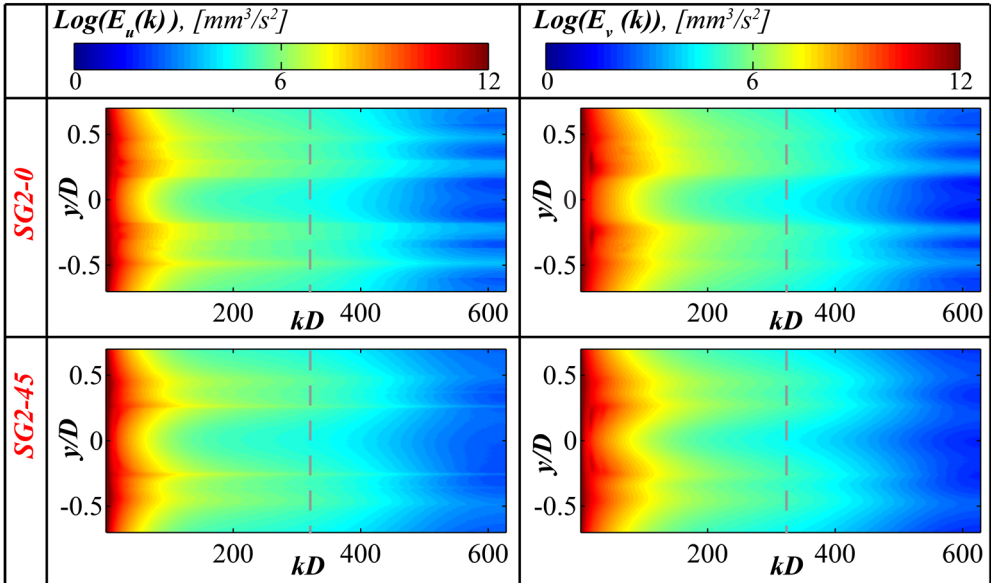


Fig. 7.9 - Velocity spectra of u (left) and v (right), related to the SG2-0 (top) and SG2-45 (bottom) configurations.

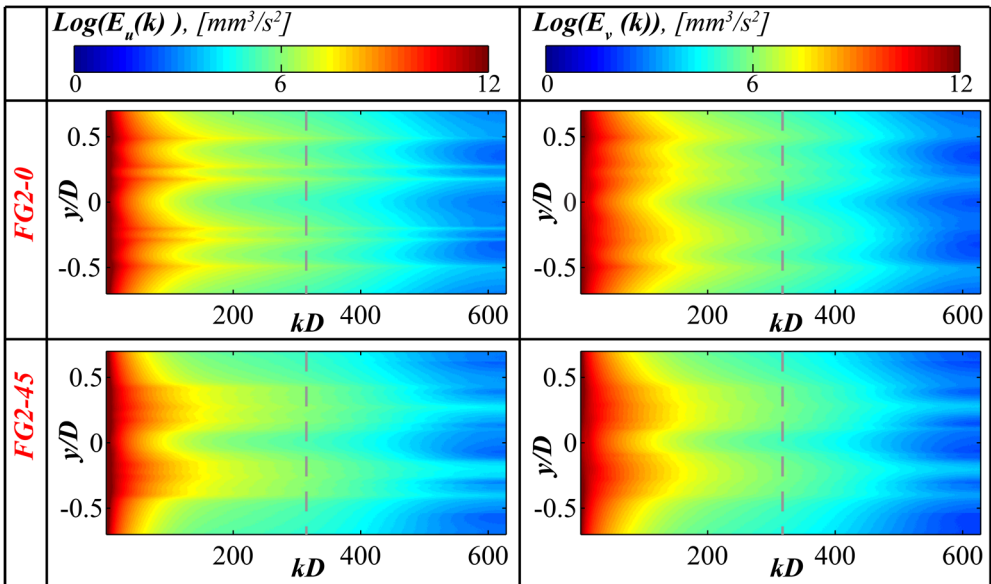


Fig. 7.10 - Velocity spectra of u (left) and v (right), related to the FG2-0 (top) and FG2-45 (bottom) configurations.

It is worth to notice that those reported are spatial-averaged energy spectra evaluated all along the streamwise length of the measurement domain, thus containing both the turbulence production and the decay region. A cut-off

7.3. VELOCITY SPECTRA

wavenumber $k_{cut-off}$ based on the used PIV algorithm is evaluated following [61]. As shown in Fig. 7.12, for the used $IW = 24 \text{ pixels}$, assuming a cut-off wavenumber $k_{cut-off} \approx 15.7 \text{ mm}^{-1}$ which corresponds to $\omega = 1$, where ω represents the normalised spatial frequency, the measurement error is less than 10%. In the following figures, this cut-off wavenumber is represented by a vertical dashed grey line.

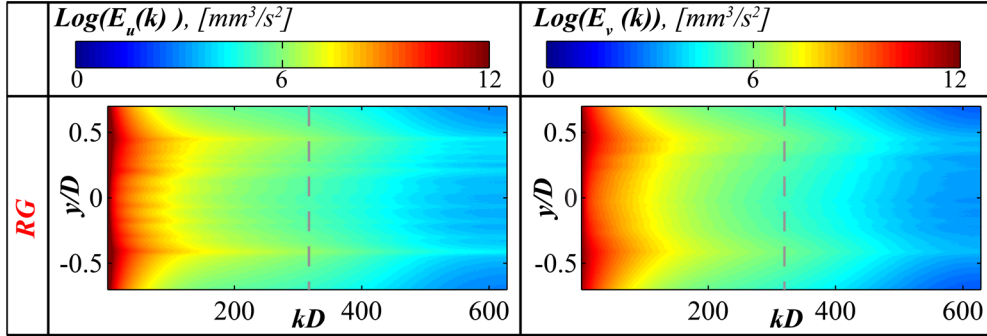


Fig. 7.11 - Velocity spectra of u (left) and v (right), related to the RG configuration.

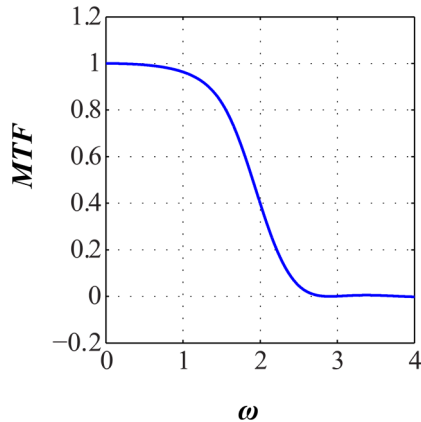


Fig. 7.12 - Modulation Transfer Function as a function of the normalised spatial frequency ω .

All the maps show that the highest energy levels are associated with the lowest wavenumber k , probably related to the jet column. However, the effects due to the external shear layer and the bars presence are clearly visible because of an energy redistribution towards higher k values at $y/D = \pm 0.5$ and $y/D = \pm 0.225$. In particular, the v -spectra related to the SGs show high values of E_v for a narrow range of wavenumbers downstream the 1st iteration bars. These peaks are mainly associated with the vortex shedding generated downstream the bars, as also found in [40, 110].

7. EFFECT OF THE GRID GEOMETRY ON THE CONTINUOUS JET FLOW FIELD

Moreover, they seem to be affected by both the holding bars (as a less persistent signature of the shedding can be observed in the *SG2* with respect to the *SG1*) and the measurement plane (as the strong jet shrinking observed along the 45° -direction reduces the intensity of this asymmetric vortex shedding; see also the eigenvalue distribution in Fig. 4.11).

In the *FG2* maps no patterns ascribable to the vortex shedding past the 1st iteration bars are visible, because of the wakes interaction, differing from the results reported in [40, 111] for free-shear flows. However, the maps show high energy levels developed past the grid bars because of the shear layers between the different *sub-jets* (see §4.1). Similarly, no vortex shedding patterns can be depicted in *RG* case but a multi-channel fashion, showing the energy associated with the shear layer across the bars, is present.

A more quantitative description of these spectra can be given by directly looking at the E_u profiles, compensated with $(kD)^{5/3}$, shown in Fig. 7.13. In these plots, that refer to the jet centreline (Fig. 7.13-a)) and to $y/D = 0.225$ (Fig. 7.13-b)), k is still nondimensionalised with respect to D . Moreover, the profiles related to the *JWT* are obtained for $4 < x/D < 8$, downstream of the potential-core region.

In Fig. 7.13-a), the *JWT* profile shows a peak at $kD \cong 4.5$ which can be associated with the Kelvin-Helmholtz instabilities. For higher kD values, the *JWT* configuration shows an almost constant profile (i.e. E_u scales as the well-known $-5/3$ power-law) over almost one decade, suggesting the presence of an inertial subrange, whilst it decreases for $kD > 20$ reaching a local minimum for $kD \approx 130$. The spectrum increases again up to the $k_{cut-off}$ value and then falls down on account to the PIV modulation. Similar results, with slightly larger energy values, are also shown for $y/D = 0.225$ in Fig. 7.13-b). A different behaviour is shown in the v -spectra reported in Fig. 7.14 since the first maximum appears to be shaded by a second stronger peak visible at around $kD = 4 \cdot 10^1$. For large wavenumbers the spectrum behaviour is very similar to the one already reported. A similar spectrum is also shown for $y/D = 0.225$.

The grid introduction significantly changes the way in which the turbulent kinetic energy redistributes over the different scales.

The *RG* curve in Fig. 7.13-a) shows a first flat region followed by an increase of E_u for $0.7 \cdot 10^1 < kD < 4 \cdot 10^1$, whilst, for higher kD a second plateau region, addressable to the inertial subrange and extending up to the $k_{cut-off}$ value, appears. This last result can be assumed as a further proof of a conservative choice for the $k_{cut-off}$ value as no-energy modulation is visible until this given wavenumber. For $y/D = 0.225$ (see Fig. 7.13-b)) the *RG* profile slightly changes at the highest

7.3. VELOCITY SPECTRA

wavenumber as a local minimum, which corresponds to the one observed in the *JWT* configuration, appears.

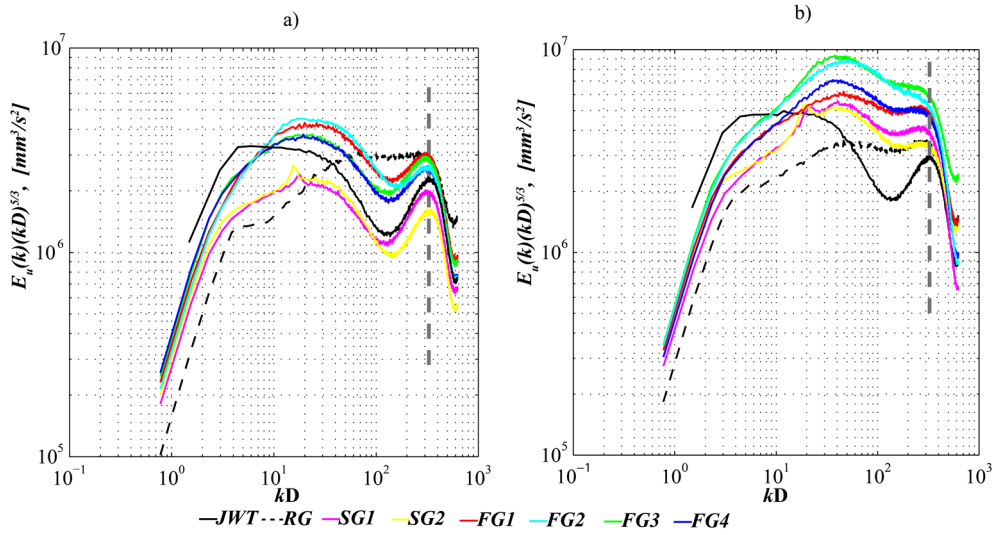


Fig. 7.13 - Compensated *u*-power spectra related to the SGs, the FGs, the RG and the JWT evaluated at a) $y/D = 0$; b) $y/D = 0.225$.

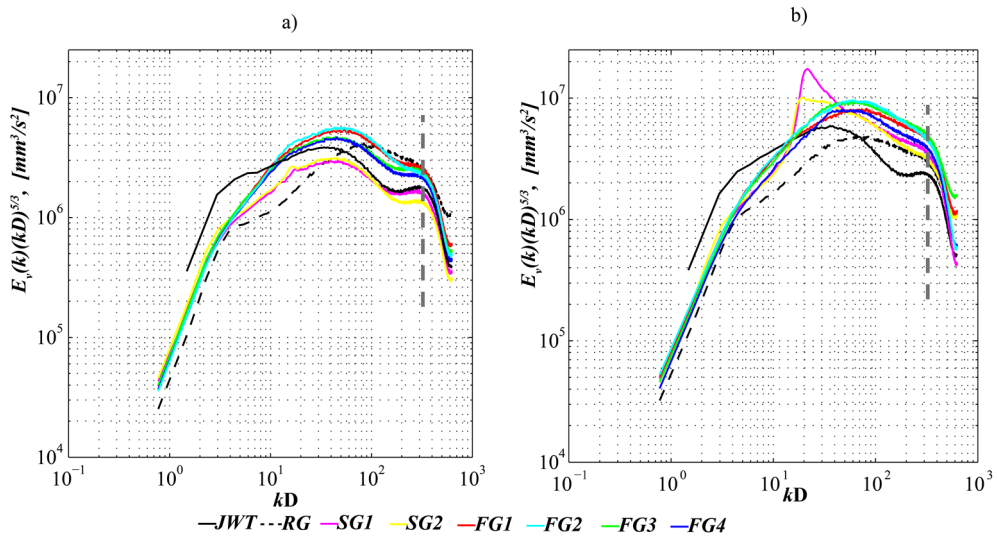


Fig. 7.14 - Compensated *v*-power spectra related to the SGs, the FGs, the RG and the JWT evaluated at a) $y/D = 0$; b) $y/D = 0.225$.

Referring to the SGs' profiles a clear peak, associated with the vortex shedding after the bars, can be detected in both Fig. 7.13 and Fig. 7.14. In particular, for the SG1*v*-spectra evaluated at $y/D = 0.225$, the Strouhal number referred to the bar

7. EFFECT OF THE GRID GEOMETRY ON THE CONTINUOUS JET FLOW FIELD

thickness, $St_{t_0} = k_{sh}t_0/2\pi$, corresponding to the peak-wavenumber k_{sh} , turn out to be $St_{t_0} = 0.17$. This value confirms that the peak in the velocity-spectra refers to the vortex shedding generated by the grid's bars. Similarly, for the *SG2* it has been found $St_{t_0} = 0.15$. These two values are only slightly lower than the ones reported by Melina et al. [40] for a single square grid in free-shear flows. Differently from the *RG*, for both *SG1* and *SG2* the u -spectra along the centreline do not show an inertial subrange. The behaviour of E_u and E_v on the centreline for $k > k_{sh}$ is very similar to the one observed for the *JWT*. On the other hand, for $y/D = 0.225$ and $k > k_{sh}$ a monotonic energy decrease is observed. Finally, by comparing the two streamwise locations, for both the *JWT* and *RG* configurations, the higher spectra values present at $y/D = 0.225$ with respect to $y/D = 0$ must be ascribed to a stronger influence of the shear layer.

As expected, no peak due to the vortex shedding past the 1st iteration bars can be observed in the *FGs*' profiles both for $y/D = 0$ and $y/D = 0.225$. On the other hand, referring to the u -spectra reported in Fig. 7.13-a) a plateau region appears for $10^1 < kD < 4 \cdot 10^1$ for all the tested *FGs*, followed by a local minimum at about $kD \approx 1.5 \cdot 10^2$. A second maximum, stronger than the one found for the *JWT* and at slightly smaller wavenumbers, is then visible. The wavenumber at which this maximum is reached slightly changes with t_r . For $y/D = 0.225$, the compensated u -spectra increase up to a kD value slightly larger than the one related to the vortex shedding of the *SGs* and then decrease. A short plateau region can be only observed for *FG1* and *FG4*. Even the compensated v -spectra only show a $-5/3$ behaviour at the highest evaluated wavenumbers, along the centreline; for $y/D = 0.225$, instead, the compensated v -spectra rapidly increase, reaching a maximum for $kD \approx 5 \cdot 10^1$ and then decrease up to the $k_{cut-off}D$ value.

The reported velocity-spectra clearly depend on N and t_r so that: 1) an increase in N causes higher spectra values over the whole range of the analysed spatial scales; 2) an increase in t_r , for fixed N value, causes larger axial and radial fluctuations values along the centreline while no clear trend is observed for $y/D = 0.225$. Indeed, while along the centreline an increase in t_r corresponds to larger momentum through the central square of the grid and thus to larger velocity-spectra, no such a clear dependence can be pointed out downstream of the bars as the energy strongly depends on the different wakes interaction.

Finally, as the majority of the velocity spectra reported in Fig. 7.13 and Fig. 7.14 show a double-peak shape, an attempt to identify which physical phenomenon is responsible for each peak is done by evaluating spatial-averaged velocity-spectra over different regions of the measurement domain. Results related to the *FG2*

7.3. VELOCITY SPECTRA

analysed along the centreline are reported in Fig. 7.15 in terms of compensated spectra. They show that, for $0 < x/D < 2$ (i.e. $0 < x/x_* < 0.49$), where the contribution of the external shear layer is less important than the grid-generated turbulence, the compensated u -spectrum increases, reaching a maximum at $kD \approx 17$ and then decreases while the compensated v -spectrum is almost constant over a whole kD decade and a dissipation region occurs for $kD \approx 10^2$. For $1 < x/D < 3$, the compensated u -spectrum shows a flatter profile at the lowest wavenumbers and a double-peak shape begins to form. Moreover a significant energy reduction is observed with respect to the previous x positions. For $2 < x/D < 4$ a well-defined peak is visible at $kD = 3 \cdot 10^2$. The spectra related to the largest x/D values all collapse on this profile for the highest wavenumbers whilst at the lowest ones they flatten out so that the production regions previously observed is substituted by an inertial subrange. Fig. 7.15-b) shows that for the v -spectra the double-peak shape appears further downstream with respect to the u -spectra (for $3 < x/D < 5$). However, the second peak does not represent an energy production region as it shows a $-5/3$ power-law behaviour.

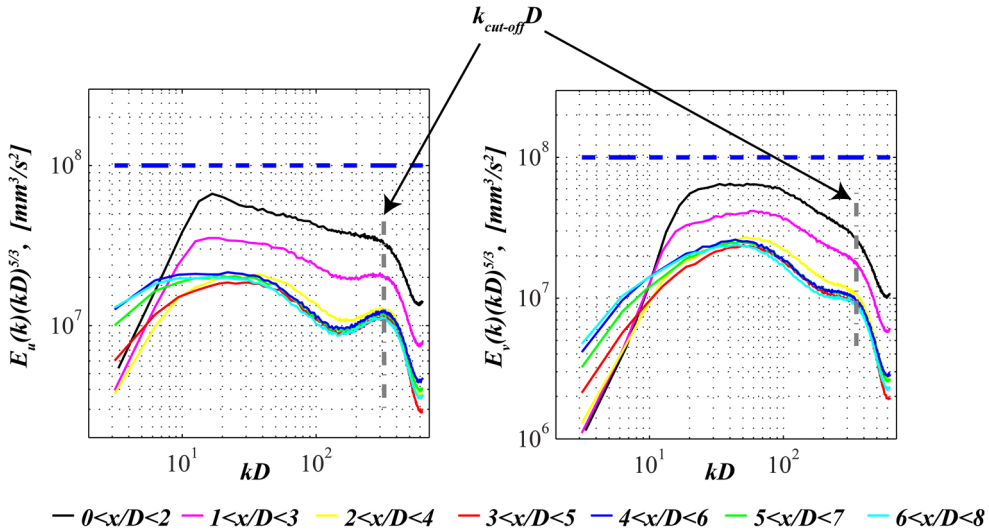


Fig. 7.15 - Compensated spatial-averaged: a) u -power spectra related to the FG2 at $y/D = 0$ for different downstream locations; b) v -power spectra related to the FG2 at $y/D = 0$ for different downstream locations.

It is worth to remind that the results presented in this chapter are obtained by stitching the flow fields evaluated with 4 different cameras that are evaluated with the same PIV algorithm. Therefore, it is unlikely that the double-peak shape is related to the cross-correlation algorithm as it is not present for $0 < x/D < 2$ (that actually

7. EFFECT OF THE GRID GEOMETRY ON THE CONTINUOUS JET FLOW FIELD

corresponds to the area imaged by one of the cameras). Moreover, considering that this shape was also observed in the *JWT* configuration, it should be addressed to the shear layer instabilities.

7.4. MAIN CONCLUSIONS

In this chapter, the effects of the bar thickness of square-fractal grids on the flow field of turbulent jets are investigated by analysing four 3-iterations square fractal grids, characterised by the same blockage ratio and L_0 but different t_0 . A regular grid having the same blockage ratio and two single square grids, both having bars of length L_0 and thickness t_0 but differing from each other for the holding bars, are also analysed. All the measurements are performed at a fixed Reynolds number, $Re \approx 16,000$; the results are compared with those relative to the axisymmetric turbulent jet.

The main obtained results are:

- the increase in t_r causes, close to the grid:
 - 1) an increase of the mean axial velocity because of the larger momentum convected through the largest square;
 - 2) a monotonic increase of the local maximum (due to the grid-generated turbulence) of u'/U_b ;
 - 3) the local peak (due to the grid-generated turbulence) of u'/U_b to move backward;
- the increase in t_r for larger x/D values, causes:
 - 1) lower values of both the mean axial velocity and the velocity fluctuations;
 - 2) the absolute peak (due to the shear layer development) of u'/U_b to move upward;
- the presence of mild peaks in the velocity fluctuations profiles evaluated along the centreline in both the *SGs* configurations confirm the importance of the Reynolds numbers on the wakes developed past the bars and on their interaction with the jet shear layer;
- close to the grid, the largescale isotropy is significantly increased by the introduction of the secondary iterations to the single square grids; moreover, for fixed N values, lower t_r also causes more isotropic velocity fluctuations;
- the velocity-spectra clearly depend on N and t_r so that:

7.4. MAIN CONCLUSIONS

- 1) an increase in N causes higher spectra values over the whole range of the analysed spatial scales (in particular, the secondary iterations strongly reduce the vortex shedding downstream the 1st iteration bars);
- 2) an increase in t_r , for fixed N value, causes larger axial and radial fluctuations values along the centreline.

CONCLUSIONS AND FUTURE PERSPECTIVES

In this thesis an experimental analysis of the effects of the secondary iterations of square-fractal grids on turbulent jets is carried out both in terms of flow field and heat transfer features. The practical goal of the study is to investigate the role played by the secondary iterations on the effectiveness of square-fractal grids as a passive method for increasing the convective heat transfer of impinging jets that are widely used for electronic device cooling, glass shaping, anti- and de-icing devices. Moreover, the parametrical analysis with respect to the bars' thickness attempts to give the reader useful information on the optimisation of the grid geometry. Finally, the application of fractal turbulators to synthetic jet devices that are very useful in industrial fields in which size, weight, and power are constrained is also investigated.

In Chapter 4, the free flow fields of a turbulent continuous jet equipped with either a 3-iterations square-fractal grid (*FG2*) or a single square grid (*SG1*) characterised by the same L_0 and t_0 values are analysed at a fixed Reynolds number $Re \approx 6,700$, by means of planar Particle Image Velocimetry, both along the square side (-0°) and the diagonal (-45°) directions. The evaluated mean axial velocity contour maps show that both the *FG2* and the *SG1* are characterised by a multi-channel flow close to the nozzle exit section, with the coexistence of both jet-like and wake-like behaviours. Moreover, the wider recirculation regions found in the *FG2-0* case with respect to the *SG1-0* one and due to the out-of-plane secondary iterations bars is a clear evidence of the high three-dimensionality of the *FG2*-flow field.

The investigation of the velocity fluctuations confirms the high efficiency of the fractal-shaped object as turbulence generator. This is, however, strongly reduced for large distances from the nozzle exit section, so that the introduction of the *FG2* becomes disadvantageous for $x/D > 8$. The evaluation of the velocity fluctuations along the centreline points out the peculiar feature of the square-fractal grids in producing a turbulence peak at a streamwise location which only depends on the largest bars' size ($\propto L_0^2/t_0$). On the other hand, it points out that no such a peak is present for the *SG1*, differently to what reported in previous works on free-shear flows. Indeed, the instantaneous z -vorticity contour maps show that the wakes generated past the bars do not reach the jet centreline also because of the interaction with the external shear layer. Finally, the application of the Proper Orthogonal Decomposition to a small region of the flow field, past the 1st iteration bars, shows that the addition of the secondary iterations to the *SG1* causes the disappearance of the vortex shedding generated by the largest bars.

CONCLUSIONS AND FUTURE PERSPECTIVES

In Chapter 5, the effects of either the introduction of the *FG2* or of the *SG1* at the exit section of a synthetic jet device are investigated for three different dimensionless stroke lengths \mathcal{L}_0/D equal to 50.0, 19.2 and 7.1, respectively. The obtained results show that, for the tested \mathcal{L}_0/D values, the grids (above all the fractal one) not only do not prevent the generation of a synthetic jet but are also responsible for additional vortical structures downstream the 1st iteration bars which interact with the one generated at the nozzle edges causing its azimuthal deformation and forcing its breakdown. This streamwise vorticity production suggests a significant increase in terms of mixing and heat transfer rate due to the grid-generated turbulence. Moreover, the phase-averaged *tke* maps show that, as found for conventional steady jets, the fractal grids are extremely efficient turbulators only at short distances from the nozzle.

The time-averaged flow field statistics, evaluated along the centreline, show that the turbulent jet developed past the *FG2* is less influenced by the actuation frequency than both the *SG1* and the *JWT*. Indeed, a stable peak in the mean axial velocity profile is found at $x/D = 0.9$ despite the stroke length. Similarly, a local maximum of the axial velocity fluctuations is located at $x/D = 1.6$ (as found for the continuous jets) for each of the tested actuation frequencies. In this respect, it is worth to notice that not such a maximum is visible for the analysed *SG1* configurations, confirming the results reported in Chapter 4 (that are carried out at the same global Reynolds number).

In Chapter 6, the effect of the grid geometry on the convective heat transfer rate distribution and uniformity is assessed by means of IR Thermography measurements. Two different aspects are considered: the introduction of the secondary iterations and the grid thickness ratio.

The former parameter, which is assessed by comparing the reference fractal grid *FG2* with respect to two-single square grids, the *SG1* and the *SG2* (which only differ for the holding bars), under the same power input, highlights that significant differences are visible, especially at short nozzle-to-plate distances in terms of convective heat transfer rate; an increase in the Nusselt number stagnation point of even 40% for plates located one diameter far from the nozzle is observed. This is a clear identification of the role played by the secondary grid iterations onto the convective heat transfer rate distribution which comes directly from their relevance in terms of turbulence production. However, the introduction of the secondary iterations causes less uniform Nusselt number maps thus suggesting of using square-fractal grids only if localised high heat transfer rates are needed.

The latter parameter is, instead, assessed by comparing four 3-iterations square-fractal grids characterised by the same blockage ratio and bars' length. The results

show that, at short nozzle-to-plate distances, the convective heat transfer rate increments accordingly to the location of the peak in turbulence intensity level along the centreline. On the other hand, an increase in t_r results in less uniform Nusselt number distributions.

In Chapter 7, the effects of the bars' thickness on the turbulent round jet equipped with the fractal inserts, at a fixed Reynolds number $Re \approx 16,000$, are investigated. All the grids analysed in Chapter 6 together with a regular grid having the same blockage ratio of the fractal ones are investigated. The axial velocity fluctuations profiles evaluated along the centreline show, for fixed N , σ and L_0 , a local maximum due to the fractal-generated turbulence and an absolute maximum which is due to the penetration of the external shear layer. The grid-generated turbulence peak increases and moves upward as the thickness ratio increases, thus justifying the largest stagnation point Nusselt number Nu_0 shown in Chapter 6 at the largest thickness ratio. On the other hand, the turbulence peak addressed to the external shear layer development increases and moves downward as the thickness ratio decreases. Moreover, differently to the results reported for the lowest Reynolds number, both the *r.m.s.* of the axial and radial velocity fluctuations referred to the two single square grids show a local peak addressable to the wakes developed past the grids' bars, which is located downward with respect to the *FG2* according to the smaller number of iterations. This result points out the importance of the global Reynolds number on the wakes developed past the bars and of their interaction with the jet shear layer.

The large-scale isotropy, at short distances from the grid, is significantly increased by the introduction of the secondary iterations to the single square grids, above all for small thickness ratios. This result agrees with the higher homogeneity of the Nusselt number distributions found for the grid characterised by the smallest thickness ratio. The spatial-averaged velocity power spectra, evaluated along the streamwise direction, point out that the square-fractal grids develop higher energy values over the entire range of analysed spatial scales than both the single square grids and the regular grid. The obtained spectra also confirm that the introduction of the secondary iterations reduces the vortex shedding energy related to the largest bars (as the peaks corresponding to the vortex-shedding generated by those bars can only be observed for *SGs* configurations).

Although the extensive study on the effects of the secondary iterations bars on the flow field of turbulent jets equipped with square-fractal grids carried out in this thesis, some questions are still open.

First, it would be interesting to perform three-dimensional flow field measurements on the synthetic jet equipped with the fractal insert in order to deeply analyse the interaction between the vortex ring developed at the nozzle edges and the

CONCLUSIONS AND FUTURE PERSPECTIVES

coherent vortical structures developed because of the bars. These measurements could be useful to identify the main factors which are responsible for the more rapid breakdown of the vortex ring in this quasi-stationary flow field. Furthermore, because of the possibility to force the ring at a fixed position, they could be also useful for better understanding the effects of the fractal-generated turbulence on the toroidal vortices developed in the shear layer of continuous jets because of the Kelvin-Helmholtz instabilities. Heat transfer measurements on synthetic jet devices equipped with the fractal grids are also needed to assess their efficacy as cooling systems.

The evaluation of the velocity fluctuations along the centreline in single square grids also leave some open questions, so that only parametrical studies in terms of both the global Reynolds number and the bars' dimensions could give a clear explanation of the interaction between the shear layer and the bars' wakes.

NOMENCLATURE

Greek symbols

α, β	Constants
α_r	Absorptivity coefficient
$\alpha_{r\lambda}$	Spectral absorptivity coefficient
β'	Added mass coefficient
ΔP_0	Pressure-drop across the grids, (Pa)
Δpix	Pixel size, (<i>pixels</i>)
$\Delta \theta$	Phase of the synthetic jet device impedance signal, ($^\circ$)
Δx_{sp}	Maximum streamwise excursion of the saddle point, (m)
Δt	Time delay between subsequent laser pulses, (s)
$\Delta x, \Delta y$	Planar displacement components in the image plane, (<i>pixels</i>)
Δz_0	Laser sheet thickness, (m)
δ_z	Depth of field, (m)
ε	Turbulent kinetic energy dissipation rate per unit mass,
ε_{iso}	Turbulent kinetic energy dissipation rate per unit mass in isotropic turbulence, (m^2/s^3)
ε_{λ_c}	Spectral hemispherical emissivity coefficient
ε_t	Total hemispherical emissivity coefficient
ζ	Azimuthal coordinate
λ	POD eigenvalue
λ_c	Electromagnetic wavelength, (m)
λ_l	Laser wavelength, (m)
$\lambda_{c,max}$	Wavelength of maximum spectral emissive power, (m)
λ_u	Longitudinal Taylor microscale, (m)
μ	Dynamic viscosity, ($Pa \cdot s$)
ν	Kinematic viscosity, (m^2/s)

NOMENCLATURE

ξ	Radial coordinate
ρ	Density, (Kg^3/m)
ρ_p	Tracer particle's density, (Kg^3/m)
ρ_r	Reflectivity coefficient
$\rho_r \lambda_c$	Spectral reflectivity coefficient
σ	Grid's blockage ratio
$\bar{\sigma}$	Stefan-Boltzmann constant, (W/m^2K^4)
σ_{Nu}	Area-averaged Nusselt number
θ_v	Phase of the voltage signal, ($^\circ$)
θ_j	Phase of the current intensity signal, ($^\circ$)
τ	Synthetic jet phenomenon period, (s)
τ_r	Transmissivity coefficient
τ_s	Tracer particle relaxation time, (s)
ν	Frequency of the electromagnetic wave, (1/s)
Φ	Synthetic jet phase, ($^\circ$)
φ	Chevron angle, ($^\circ$)
ω	Normalised PIV interrogation window
ω_z	Vorticity component along the z-axis, (1/s)

Roman symbols

a	Air speed of sound, (m/s)
A	Area covered by the grid, (m^2)
A_m	Measured amplitude of the signal detected by the IR camera
A_n	Nozzle section area, (m^2)
A_r	Real amplitude of the signal detected by the IR camera
$A(x)$	Approximately constant generic function
B	IR camera calibration constant
$B(x)$	Generic steep power law
b	Regular grid bars' thickness, (m)

δ	Grid thickness, (m)
b_j	Jet half-width, (m)
$Bi = hs/k_{foil}$	Biot Number
c	Speed of light, (m/s)
c_0	Speed of light in vacuum, (m/s)
C_1	First radiation constant, ($W m^2$)
C_2	Second radiation constant, (Km)
C_ε	Dissipation coefficient
$C_{\varepsilon_{iso}}$	Dissipation coefficient in isotropic turbulence
C_D	Drag coefficient
C_V	Wake volume coefficient
D	Nozzle diameter, (m)
D_f	Fractal dimension
D_L	Nominal loudspeaker diameter, (m)
d	Turbine shaft centre to mean tip distance, (m)
d_{diff}	Diffraction-limited particle diameter, (m)
d_{geom}	Geometric image particle diameter, (m)
d_p	Physical particle diameter, (m)
d_τ	Particle diameter, (m)
E	Total hemispherical emissive power, (W/m^2)
E_{λ_c}	Real body spectral hemispherical emissive power, ($W/m^2 \mu m$)
$E_{b\lambda_c}$	Black body spectral hemispherical emissive power in vacuum, ($W/m^2 \mu m$)
$E_{b,a}$	Radiation emitted by the environment, (W/m^2)
$E_{b,atm}$	Radiation emitted by the atmosphere, (W/m^2)
E_b	Radiation flux emitted by the black body, (W/m^2)
E_{IR_c}	Radiation flux collected by the IR camera, (W/m^2)
E_{obj}	Radiation flux emitted by the viewed object, (W/m^2)

NOMENCLATURE

$E_u(k)$	1D-power spectrum of the axial velocity fluctuations, (mm^3/s^2)
$E_v(k)$	1D-power spectrum of the radial velocity fluctuations, (mm^3/s^2)
F	IR camera calibration constant
f	Loudspeaker actuation frequency, (Hz)
f_H	Cavity Helmholtz resonance frequency, (Hz)
f_l	Laser acquisition frequency, (Hz)
f_L	Loudspeaker resonance frequency, (Hz)
f_1	1 st synthetic jet device resonance frequency, (Hz)
f_2	2 nd synthetic jet device resonance frequency, (Hz)
$f_{\#}$	Numerical aperture of the camera
h	Convective heat transfer coefficient, (W/m^2K)
J	Current intensity, (A)
k	Wavenumber, ($1/m$)
k_f	Fluid thermal conductivity, ($W/m K$)
k_{foil}	Foil thermal conductivity, ($W/m K$)
k_{sh}	Wavenumber related to the vortex shedding behind the bars of thickness t_0
L_0	Length of the 1 st iteration bars, (m)
L_{sj}	Synthetic jet device nozzle length, (m)
L'_{sj}	Synthetic jet device equivalent nozzle length, (m)
L_u	Longitudinal integral length-scale, (m)
L_j	Length of the 1 st iteration bars, (m)
\mathcal{L}_0	Stroke-length
l	Generic flow characteristic length, (m)
M	Regular grid meshlength, (m)
M_0	Magnification factor
M_{eff}	Grid's effective meshlength, (m)
\dot{m}	Mass flow rate, (g/s)

N	Number of fractal iterations
N_s	Source density
$Nu = hl/k_f$	Nusselt number
Nu_0	Stagnation point Nusselt number
\overline{Nu}	Area-averaged Nusselt number
n	POD mode number
\mathfrak{m}	Turbine rotational frequency, (1/s)
n	Dimensionless index of refraction of the medium
O	IR camera generic output, (W/m^2)
P	Fractal perimeter of the grid, (m)
$\langle P \rangle$	Active power developed by the synthetic jet device, (W)
Q	Second invariant of the velocity gradient tensor, ($1/s^2$)
q_c	Convective heat flux, (W/m^2K)
q_j	Joule effect heat flux, (W/m^2K)
q_{nc}	Natural convection heat flux, (W/m^2K)
q_r	Radiative heat flux, (W/m^2K)
q_{tc}	Tangential convection heat flux, (W/m^2K)
R	IR camera calibration constant
r	Radius, (m)
R_L	Ratio between the length of subsequent bars
R_t	Ratio between the thickness of subsequent bars
$Re = U_b D/\nu$	Continuous jets Reynolds number
$Re_{L_u} = U_\infty L_u/\nu$	Global Reynolds number defined with respect to L_u
$Re_M = U_\infty M/\nu$	Global Reynolds number defined with respect to the bar side-length for regular grids
$Re_{sj} = U_0 D/\nu$	Synthetic jet Reynolds number
$Re_{t_0} = U_\infty t_0/\nu$	Global Reynolds number evaluated with respect to t_0
$Re_{\lambda_u} = u' \lambda_u/\nu$	Longitudinal local Reynolds number

NOMENCLATURE

$Re_n = \pi d^2 / \nu$	Global Reynolds number referred to the turbine rotational frequency n and mean diameter d
$Re_0 = U_\infty l / \nu$	Inlet Reynolds number based on an inlet characteristic length scale l
$S = db_j / dx$	Jet spreading rate
s	Sensor thickness, (m)
$St = fD / U_0$	Synthetic jet Strouhal number
$St_{t_0} = k_{sh} t_0 / 2\pi$	Strouhal number referred to the vortex shedding behind the bars of thickness t_0
T	Absolute body temperature, (K)
T_a	Environment temperature, (K)
T_{atm}	Atmosphere temperature, (K)
T_{aw}	Adiabatic wall temperature, (K)
\widetilde{T}_b	Measured black body temperature, (K)
T_{obj}	Object temperature, (K)
T_r	Reference temperature, (K)
T_t	Tunnel's square cross-section, (m^2)
T_w	Wall temperature, (K)
t_j	Thickness of the j^{th} iteration bars, (m)
t_0	Thickness of the 1 st iteration bars, (m)
t	Time, (s)
t_r	Bars' thickness ratio between the largest and the smallest bars
tke	In plane turbulent kinetic energy, (m^2/s^2)
$\langle tke \rangle$	In plane phase-averaged turbulent kinetic energy, (m^2/s^2)
U, V	Instantaneous axial and radial velocity components, (m/s)
\bar{U}, \bar{V}	Axial and radial time-averaged velocity components, (m/s)
$\langle U \rangle, \langle V \rangle$	Axial and radial phase averaged velocity components, (m/s)
U_0	Synthetic jet characteristic velocity, (m/s)
U_A	Centreline velocity at the orifice exit plane, (m/s)
U_b	Bulk velocity, (m/s)

U_∞	Inlet velocity, (m/s)
u', v'	<i>r.m.s.</i> of u and v , (m/s)
u, v	Instantaneous axial and radial velocity fluctuations components (m/s)
\tilde{u}, \tilde{v}	Phase-correlated organized contribution to the axial and radial velocity components, (m/s)
\mathcal{V}	Voltage, (V)
V_c	Volume of the synthetic jet device cavity, (m^3)
x, y, z	Spatial coordinates
x_e	Separation point between the $C_{\varepsilon_{iso}} \sim Re_{Lu}^{-1}$ and the $C_{\varepsilon_{iso}} \approx const$ regime
x_{peak}	Centreline streamwise location of the maximum turbulence intensity, (m)
x_0	Virtual origin
x_*	Wake interaction length scale for the largest bars, (m)
Z	Synthetic jet device impedance, (Ω)
Z_0	Lens-to-target plane distance, (m)
z_0	Lens-to-image plane distance, (m)

Acronyms

$2C$	2-components
$2D$	2-dimensional
$3C$	3-components
$3D$	3-dimensional
CCD	Charge Coupled Device
$CMOS$	Complementary Metal-Oxide Semiconductor
CJ/A	Continuous Jet experiment described in Chapter 4
CJ/B	Continuous Jet experiment described in Chapter 7
CVS	Coherent Vortical Structure
FG	Fractal Grid

NOMENCLATURE

<i>IFOV</i>	Instantaneous Field Of View
<i>IR</i>	InfraRed
<i>IW</i>	Interrogation Window
<i>JWT</i>	Jet Without Turbulators
<i>LFV</i>	Large Field of View camera
<i>LWIR</i>	Long Wavelength Infrared
<i>MTF</i>	Modulation Transfer Function
<i>MWIR</i>	Medium Wavelength Infrared
<i>NETD</i>	Noise Equivalent Temperature Difference
<i>PIV</i>	Particle Image Velocimetry
<i>POD</i>	Proper Orthogonal Decomposition
<i>ppp</i>	particle per pixel
<i>RG</i>	Regular Grid
<i>rms</i>	root mean square
<i>SG</i>	single Square Grid
<i>SFV</i>	Small Field of View camera
<i>sCMOS</i>	scientific Complementary Metal-Oxide Semiconductor
<i>ZNMF</i>	Zero-Net Mass Flux

REFERENCES

- [1] G. Cafiero, S. Discetti and T. Astarita, "Heat transfer enhancement of impinging jets with fractal-generated turbulence," *International Journal of Heat and Mass Transfer*, vol. 75, pp. 173-183, 2014.
- [2] G. Cafiero, S. Discetti and T. Astarita, "Flow field topology of submerged jets with fractal generated turbulence," *Physics of Fluids*, vol. 27, no. 11, p. 115103, 2015.
- [3] G. Cafiero, C. S. Greco, T. Astarita and S. Discetti, "Flow field features of fractal impinging jets at short nozzle to plate distances," *Experimental Thermal and Fluid Science*, vol. 78, pp. 334-344, 2016.
- [4] G. Cafiero, G. Castrillo, C. S. Greco and T. Astarita, "Effect of the grid geometry on the convective heat transfer of impinging jets," *International Journal of Heat and Mass Transfer*, vol. 104, pp. 39-50, 2017.
- [5] W. Sierpinski, "Sur une courbe cantorienne qui contient une image biunivoque et continue de toute courbe donnée," *Comptes rendus hebdomadaires des séances de l'Académie des sciences*, no. 162, pp. 629-632, 1916.
- [6] B. B. Mandelbrot, "Fractal aspects of the iteration of $z \rightarrow \Lambda z (1-z)$ for complex Λ and z ," *Annals of the New York Academy of Sciences*, vol. 357, no. 1, pp. 249-259, 1980.
- [7] D. Freeman, "Characterizing irregularity," *Science*, vol. 200, no. 4342, pp. 677-678, 1978.
- [8] M. Rieu and G. Sposito, "Fractal fragmentation, soil porosity, and soil water properties: I. Theory," *Soil Science Society of America Journal*, vol. 55, no. 5, pp. 1231-1238, 1991.
- [9] M. Rieu, and G. Sposito, "Fractal fragmentation, soil porosity, and soil water properties: II. Applications," *Soil Science Society of America Journal*, vol. 55, no. 5, pp. 1239-1244, 1991.
- [10] L. Telesca, V. Lapenna and M. Macchiato, "Mono-and multi-fractal investigation of scaling properties in temporal patterns of seismic sequences," *Chaos, Solitons & Fractals*, vol. 19, no. 1, pp. 1-15, 2004.

REFERENCES

- [11] A. Majumdar and B. Bhushan, "Role of fractal geometry in roughness characterization and contact mechanics of surfaces," *ASME J. Tribol.*, vol. 112, no. 2, pp. 205-216, 1990.
- [12] Y. Fisher, *Fractal image compression: theory and application*, Springer Science & Business Media, 2012.
- [13] J. Anguera, C. Puente, C. Borja and J. Soler, "Fractal shaped antennas: A review," *Encyclopedia of RF and microwave engineering*, 2005.
- [14] A. Hunt, R. Ewing and B. Ghanbarian, *Percolation theory for flow in porous media*, vol. 880, Springer, 2014.
- [15] G. L. North and D. A. Santavicca, "The fractal nature of premixed turbulent flames," *Combustion Science and Technology*, vol. 72, no. 4-6, pp. 215-232, 1990.
- [16] Y. W. Chin, R. D. Matthews, S. P. Nichols and T. M. Kiehne, "Use of fractal geometry to model turbulent combustion in SI engines," *Combustion science and Technology*, vol. 86, no. 1-6, pp. 1-30, 1992.
- [17] A. R. Kerstein, "Fractal dimension of turbulent premixed flames," *Combustion science and technology*, vol. 60, no. 4-6, pp. 441-445, 1988.
- [18] L. Richardson, "Atmospheric diffusion shown on a distance-neighbour graph," *Proceedings of the Royal Society of London. Series A, Containing Papers of a Mathematical and Physical Character*, vol. 110, no. 756, pp. 709-737, 1926.
- [19] A. N. Kolmogorov, "Dissipation of energy in locally isotropic turbulence," *Dokl. Akad. Nauk SSSR*, vol. 32, no. 1, pp. 16-18, 1941.
- [20] A. N. Kolmogorov, "On the degeneration of isotropic turbulence in an incompressible viscous fluid," *Dokl. Akad. Nauk SSSR*, vol. 31, pp. 319-323, 1941.
- [21] D. Queiros- Conde and J. C. Vassilicos, "Turbulent wakes of 3D fractal grids," *In Intermittency in Turbulent Flows and Other Dynamical Systems*, pp. 136-167, 2001.
- [22] A. Staicu, B. Mazzi, J. C. Vassilicos and W. van de Water, "Turbulent wakes of fractal objects," *Physical Review Let E*, vol. 67, no. 6, p. 066306, 2003.

- [23] D. Hurst and J. C. Vassilicos, "Scaling and decay of fractal-generated turbulence," *Physics of Fluids*, vol. 19, no. 3, 2007.
- [24] G. Comte-Bellot and S. Corrsin, "The use of a contraction to improve the isotropy of grid-generated turbulence," *Journal of Fluid Mechanics*, vol. 25, no. 4, pp. 657-682, 1966.
- [25] H. Makita, "Realization of a large-scale turbulence field in a small wind tunnel," *Fluid Dynamics Research*, vol. 8, no. 1-4, pp. 53-64, 1991.
- [26] R. E. Seoud and J. C. Vassilicos, "Dissipation and decay of fractal-generated turbulence," *Physics of Fluids*, vol. 19, no. 10, p. 105108, 2007.
- [27] N. Mazellier and J. C. Vassilicos, "Turbulence without Richardson-Kolmogorov cascade," *Physics of fluids*, vol. 22, no. 7, p. 075101, 2010.
- [28] R. Gomes-Fernandes, B. Ganapathisubramani and J. C. Vassilicos, "Particle image velocimetry study of fractal-generated turbulence," *Journal of Fluid Mechanics*, vol. 711, pp. 306-336, 2012.
- [29] S. Laizet and J. C. Vassilicos, "DNS of Fractal-Generated Turbulence," *Flow Turbulence Combust*, vol. 87, pp. 673-305, 2011.
- [30] W. K. George and H. Wang, "The exponential decay of homogeneous turbulence," *Physics of Fluids*, vol. 21, no. 2, p. 025108, 2009.
- [31] P. C. Valente and J. C. Vassilicos, "The non-equilibrium region of grid-generated decaying turbulence," *Journal of Fluid Mechanics*, vol. 744, pp. 5-37, 2014.
- [32] P. C. Valente and J. C. Vassilicos, "The decay of turbulence generated by a class of multiscale grids," *Journal of Fluid Mechanics*, vol. 687, pp. 300-340, 2011.
- [33] S. Discetti, I. B. Ziskin, T. Astarita, R. J. Adrian and K. Prestridge, "PIV measurements of anisotropy and inhomogeneity in decaying fractal generated turbulence," *Fluid Dynamics Research*, vol. 45, no. 6, p. 22, 2013.
- [34] P. C. Valente and J. C. Vassilicos, "Universal dissipation scaling for nonequilibrium turbulence," *Physical Review Letters*, vol. 108, p. 214503, 2012.

REFERENCES

- [35] S. Laizet, J. Nédic and J. C. Vassilicos, “The spatial origin of $-5/3$ spectra in grid-generated turbulence,” *Physics of Fluids*, vol. 27, no. 6, p. 065115, 2015.
- [36] Y. Zhou, K. Nagata, Y. Sakai, H. Suzuki, Y. Ito, O. Terashima and T. Hayase, “Development of turbulence behind the single square grid,” *Physics of Fluids*, vol. 26, no. 4, p. 045102, 2014.
- [37] Y. Zhou, K. Nagata, Y. Sakai, H. Suzuki, Y. Ito, O. Terashima and T. Hayase, “Relevance of turbulence behind the single square grid to turbulence generated by regular-and multiscale-grids,” *Physics of Fluids*, vol. 26, no. 7, p. 075105, 2014.
- [38] Y. Zhou, K. Nagata, Y. Sakai, Y. Ito and T. Hayase, “Spatial evolution of the helical behavior and the $2/3$ power-law in single-square-grid-generated turbulence,” *Fluid Dynamics Research*, vol. 48, no. 2, p. 021404, 2016.
- [39] K. Nagata, T. Saiki, Y. Sakai, Y. Ito and K. Iwano, “Effects of grid geometry on non-equilibrium dissipation in grid turbulence,” *Physics of Fluids*, vol. 29, no. 1, p. 015102, 2017.
- [40] G. Melina, P. J. K. Bruce and J. C. Vassilicos, “Vortex shedding effects in grid-generated turbulence,” *Physical Review Fluids*, vol. 1, no. 4, p. 044402, 2016.
- [41] N. Mazellier, L. Danaila and B. Renou, “Multi-scale energy injection: a new tool to generate intense homogeneous and isotropic turbulence for premixed combustion,” *Journal of Turbulence*, vol. 11, no. 43, p. 1–30, 2010.
- [42] P. Geipel, K. H. H. Goh and R. P. Lindstedt, “Fractal-generated turbulence in opposed jet flows,” *Flow, turbulence and combustion*, vol. 85, no. 3, pp. 397-419, 2010.
- [43] k. H. H. Goh, P. Geipel, F. Hampp and R. R. Lindstedt, “Flames in fractal grid generated turbulence,” *Fluid Dynamics Research*, vol. 45, no. 6, p. 061403, 2013.
- [44] N. Soulopoulos, J. Kerl, F. Beyrau, Y. Hardalupas, A. M. K. P. Taylor and J. C. Vassilicos, “A turbulent premixed flame on fractal-grid generated turbulence,” *Fluid Dyn. Res.*, vol. 45, p. 06140418, 2013.

- [45] K. Steiros, P. J. K. Bruce, O. R. H. Buxton and J. C. Vassilicos, "Power consumption and form drag of regular and fractal-shaped turbines in a stirred tank," *AIChE Journal*, vol. 63, no. 2, pp. 843-854, 2017.
- [46] T. Sponfeldner, N. Soulopoulos, F. Beyrau, Y. Hardalupas, A. M. K. P. Taylor and J. C. Vassilicos, "The structure of turbulent flames in fractal- and regular-grid-generated turbulence," *Combustion and Flame*, vol. 162, no. 9, pp. 3379-3393, 2015.
- [47] J. Nedić and J. C. Vassilicos, "Vortex shedding and aerodynamic performance of airfoil with multiscale trailing-edge modifications," *AIAA Journal*, vol. 53, no. 11, pp. 3240-3250, 2015.
- [48] J. Nedić, B. Ganapathisubramani, J. C. Vassilicos, J. Borée, L. E. Brizzi and A. Spohn, "Aeroacoustic performance of fractal spoilers," *AIAA J*, vol. 50, no. 12, pp. 2695-2710, 2012.
- [49] J. Nedić, O. Supponen, B. Ganapathisubramani and J. C. Vassilicos, "Geometrical influence on the vortex shedding in turbulent axisymmetric wakes," *Physics of Fluids*, vol. 25, no. 3, p. 035103, 2015.
- [50] J. Nedić, B. Ganapathisubramani and J. C. Vassilicos, "Drag and near wake characteristics of flat plates normal to the flow with fractal edge geometries," *Fluid Dynamics Research*, vol. 45, no. 6, p. 061406, 2013.
- [51] S. Başbuğ, G. Papadakis and J. C. Vassilicos, "DNS investigation of the dynamical behaviour of trailing vortices in unbaflled stirred vessels at transitional Reynolds numbers," *Physics of Fluids*, vol. 29, no. 6, p. 064101, 2017.
- [52] S. Basbug, G. Papadakis and J. C. Vassilicos, "Reduced energy consumption in stirred vessels by means of fractal impellers," *arXiv preprint arXiv:1707.01730*, 2017.
- [53] M. Raffel, C. E. Willert, S. Wereley and J. Kompenh, Particle image velocimetry: a practical guide, Springer, 2013.
- [54] R. J. Adrian and J. Westerweel, Particle Image Velocimetry, Cambridge University Press, 2011.
- [55] T. Astarita and G. M. Carlomagno, Infrared thermography for thermo-fluid-dynamics, Springer Science & Business Media, 2012.

REFERENCES

- [56] C. Willert, "Stereoscopic digital particle image velocimetry for application in wind tunnel flows," *Meas. Sci. Technol.*, vol. 8, no. 12, p. 1465, 1997.
- [57] F. Scarano, "Tomographic PIV: principles and practice," *Meas. Sci. Technol.*, vol. 24, no. 1, p. 012001, 2013.
- [58] G. E. Elsinga, F. Scarano, B. Wieneke and B. W. van Oudheusden, "Tomographic particle image velocimetry," *Experiments in fluids*, vol. 41, no. 6, pp. 933-947, 2006.
- [59] C. E. Willert and M. Gharib, "Digital particle image velocimetry," *Experiments in fluids*, vol. 10, no. 4, pp. 181-193, 1991.
- [60] T. Schiwietz and R. Westermann, "GPU-PIV," *VMV*, pp. 151-158, 2004.
- [61] T. Astarita, "Analysis of weighting windows for image deformation methods in PIV," *Experiments in fluids*, vol. 43, no. 6, pp. 859-872, 2007.
- [62] T. Astarita, "Analysis of velocity interpolation schemes for image deformation methods in PIV," *Experiments in fluids*, vol. 45, no. 2, pp. 257-266, 2008.
- [63] J. Westerweel, "Fundamentals of digital particle image velocimetry," *Measurement science and technology*, vol. 8, no. 12, p. 1379, 1997.
- [64] R. J. Adrian, "Particle-imaging techniques for experimental fluid mechanics," *Annual review of fluid mechanics*, vol. 23, no. 1, pp. 261-304, 1991.
- [65] B. Levesque, P. Brémond, J. L. Lasserre, A. Paupert and D. L. Balageas, "Performance of FPA IR cameras and their improvement by time, space and frequency data processing: Part I-Intrinsic characterization of the thermographic system," *Quantitative InfraRed Thermography Journal*, vol. 2, no. 1, pp. 97-112., 2005.
- [66] E. J. List, "Turbulent jets and plumes," *Annual review of fluid mechanics*, vol. 14, no. 1, pp. 189-212, 1982.
- [67] R. Viskanta, "Heat transfer to impinging isothermal gas and flame jets," *Experimental thermal and fluid science*, vol. 6, no. 2, pp. 111-134, 1993.
- [68] C. G. Ball, H. Fellouah and A. Pollard, "The flow field in turbulent round free jets," *Progress in Aerospace Sciences*, vol. 50, pp. 1-26, 2012.

- [69] G. G. Carlomagno and A. Ianiro, "Thermo-fluid-dynamics of submerged jets impinging at short nozzle-to-plate distance: a review," *Experimental thermal and fluid science*, vol. 58, pp. 15-35, 2014.
- [70] T. L. Labus and E. P. Symons, "Experimental investigation of an axisymmetric free jet with an initially uniform velocity profile.," *Nasa Technical Note*, Vols. D-6783, 1972.
- [71] G. N. Abramovich, T. A. Girshovich, S. I. Krasheninnikov, A. N. Sekundov and I. P. Smirnova, *The theory of turbulent jets*, Moscow Izdatel Nauka, 1984.
- [72] A. A. Townsend, *The structure of turbulent shear flow*, Cambridge University Press, 1980.
- [73] S. B. Pope, *Turbulent flows*, Cambridge University Press, 2001.
- [74] A. J. Yule, "Large-scale structure in the mixing layer of a round jet," *Journal of Fluid Mechanics*, vol. 89, no. 3, pp. 413-432, 1978.
- [75] G. B. Brown, "On vortex motion in gaseous jets and the origin of their sensitivity to sound," *Proceedings of the Physical Society*, vol. 47, no. 4, pp. 703-732, 1935.
- [76] H. E. Fiedler, "Coherent structures in turbulent flows," *Progress in Aerospace Sciences*, vol. 25, no. 3, pp. 231-269, 1988.
- [77] D. Liepmann and M. Gharib, "The role of streamwise vorticity in the near-field entrainment of round jets," *Journal of Fluid Mechanics*, vol. 245, pp. 643-668, 1992.
- [78] T. Astarita, "Analysis of interpolation schemes for image deformation methods in PIV: effect of noise on the accuracy and spatial resolution," *Experiments in fluids*, vol. 40, no. 6, pp. 977-987, 2006.
- [79] T. Astarita, "Adaptive space resolution for PIV," *Experiments in fluids*, vol. 46, no. 6, p. 1115, 2009.
- [80] R. J. Moffat, "Describing the uncertainties in experimental results," *Experimental thermal and fluid science*, vol. 1, no. 1, pp. 3-17, 1988.
- [81] R. Holman, Y. Utturkar, R. Mittal, B. L. Smith and L. Cattafesta, "Formation criterion for synthetic jets," *AIAA journal*, vol. 43, no. 10, pp. 2110-2116, 2005.

REFERENCES

- [82] B. L. Smith and A. Glezer, "The formation and evolution of synthetic jets," *Physics of fluids*, vol. 10, no. 9, pp. 2281-2297, 1998.
- [83] J. M. Shuster and D. R. Smith, "Experimental study of the formation and scaling of a round synthetic jet," *Physics of fluids*, vol. 19, no. 4, p. 045109, 2007.
- [84] A. Glezer, "The formation of vortex rings," *The Physics of fluids*, vol. 31, no. 12, pp. 3532-3542, 1988.
- [85] A. McGuinn, R. Farrelly, T. Persoons and D. B. Murray, "Flow regime characterisation of an impinging axisymmetric synthetic jet," *Experimental Thermal and Fluid Science*, vol. 47, pp. 241-251, 2013.
- [86] M. Gharib, E. Rambod and K. Shariff, "A universal time scale for vortex ring formation," *Journal of Fluid Mechanics*, vol. 360, pp. 121-140, 1998.
- [87] T. Persoons, "General reduced-order model to design and operate synthetic jet actuators," *AIAA Journal*, vol. 50, no. 4, pp. 916-927, 2012.
- [88] L. L. Beranek, *Acoustics*, New York: Acoustical Society of America, 1993 (Original work published by McGraw-Hill, New York, pp. 47-77 1954).
- [89] L. de Luca, M. Girfoglio and G. Coppola, "Modeling and Experimental Validation of the Frequency Response of Synthetic Jet Actuators," *AIAA Journal*, vol. 52, no. 8, pp. 1733-1748, 2014.
- [90] B. L. Smith and G. W. Swift, "A comparison between synthetic jets and continuous jets," *Experiments in fluids*, vol. 34, no. 4, pp. 467-472, 2003.
- [91] W. R. Quinn and M. Azad, "Mean flow and turbulence measurements in a turbulent free cruciform jet," *Flow, turbulence and combustion*, vol. 91, no. 4, pp. 773-804, 2013.
- [92] S. Ma, C. W. Kang, T. B. A. Lim, C. H. Wu and O. Tutty, "Wake of two side-by-side square cylinders at low Reynolds numbers," *Physics of Fluids*, vol. 29, no. 3, p. 033604, 2017.
- [93] L. Sirovich, "Turbulence and the dynamics of coherent structures. I. Coherent structures," *Quarterly of applied mathematics*, vol. 45, no. 3, pp. 561-571, 1987.

- [94] K. E. Meyer, J. M. Pedersen and O. Özcan , “A turbulent jet in crossflow analysed with proper orthogonal decomposition,” *Journal of Fluid Mechanics*, vol. 583, pp. 199-227, 2007.
- [95] L. H. Feng and J. J. Wang, “Circular cylinder vortex-synchronization control with a synthetic jet positioned at the rear stagnation point,” *Journal of Fluid Mechanics*, vol. 662, pp. 232-259, 2010.
- [96] M. Raiola, S. Discetti and A. Ianiro, “On PIV random error minimization with optimal POD-based low-order reconstruction,” *Experiments in Fluids*, vol. 56, no. 4, pp. 1-15, 2015.
- [97] H. F. Wang, H. L. Cao and Y. Zhou, “POD analysis of a finite-length cylinder near wake,” *Experiments in fluids*, vol. 55, no. 8, p. 1790, 2014.
- [98] p. Baj, P. J. Bruce and O. R. Buxton, “The triple decomposition of a fluctuating velocity field in a multiscale flow,” *Physics of Fluids*, vol. 27, no. 7, p. 075104, 2015.
- [99] V. Kitsios, L. Cordier, J. P. Bonnet, A. Ooi and J. Soria, “Development of a nonlinear eddy-viscosity closure for the triple-decomposition stability analysis of a turbulent channel,” *Journal of Fluid Mechanics*, vol. 664, pp. 74-107, 2010.
- [100] G. M. Di Cicca and G. Iuso, “On the near field of an axisymmetric synthetic jet,” *Fluid dynamics research*, vol. 39, no. 9, pp. 673-693, 2007.
- [101] S. R. Fugal, B. L. Smith and R. E. Spall, “Displacement amplitude scaling of a two-dimensional synthetic jet,” *Physics of Fluids*, vol. 17, no. 4, p. 045103, 2005.
- [102] M. Chaudhari, G. Verma, B. Puranik and A. Agrawal, “Frequency response of a synthetic jet cavity,” *Experimental thermal and fluid science*, vol. 33, no. 3, pp. 439-448, 2009.
- [103] M. Chaudhari, B. Puranik and A. Agrawal, “Effect of orifice shape in synthetic jet based impingement cooling,” *Experimental Thermal and Fluid Science*, vol. 34, no. 2, pp. 246-256, 2010.
- [104] L. Oren, E. Gutmark, S. Muragappan and S. Khosla, “Flow characteristics of non circular synthetic jets,” in *47th AIAA Aerospace Sciences Meeting*, Orlando, Florida, 2009, January.

REFERENCES

- [105] K. Nishibe, Y. Fujita, K. Sato, K. Yokota and T. Koso, “Experimental and numerical study on the flow characteristics of synthetic jets,” *Journal of fluid science and technology*, vol. 6, no. 4, pp. 425-436, 2011.
- [106] C. M. Crispo, C. S. Greco, F. Avallone and G. Cardone, “On the flow organization of a chevron synthetic jet,” *Experimental Thermal and Fluid Science*, vol. 82, pp. 136-146, 2017.
- [107] F. F. Grinstein, “Vortex dynamics and entrainment in rectangular free jets,” *Journal of Fluid Mechanics*, vol. 437, pp. 69-101, 2001.
- [108] C. S. Greco, G. Castrillo, C. M. Crispo, T. Astarita and G. Cardone, “Investigation of impinging single and twin circular synthetic jets flow field,” *Experimental Thermal and Fluid Science*, vol. 74, pp. 354-367, 2016.
- [109] A. Ianiro and G. Cardone, “Heat transfer rate and uniformity in multichannel swirling impinging jets,” *Applied Thermal Engineering*, vol. 49, pp. 89-98, 2012.
- [110] S. Laizet, J. C. Vassilicos and C. Cambon, “Interscale energy transfer in decaying turbulence and vorticity–strain-rate dynamics in grid-generated turbulence,” *Fluid Dynamics Research*, vol. 45, no. 6, p. 20, 2013.
- [111] R. Gomes-Fernandes, B. Ganapathisubramani and J. C. Vaassilicos, “The energy cascade in near-field non-homogeneous non-isotropic turbulence,” *Journal of Fluid Mechanics*, vol. 771, pp. 676-705, 2015.

LIST OF PUBLICATIONS

JOURNAL PAPERS

- Greco, C. S., Castrillo, G., Crispo, C. M., Astarita, T., & Cardone, G. (2016). Investigation of impinging single and twin circular synthetic jets flow field. *Experimental Thermal and Fluid Science*, 74, 354-367.
- Castrillo, G., Cafiero, G., Discetti, S., & Astarita, T. (2016). Blob-enhanced reconstruction technique. *Measurement Science and Technology*, 27(9), 94011-94022.
- Cafiero, G., Castrillo, G., Greco, C. S., & Astarita, T. (2017). Effect of the grid geometry on the convective heat transfer of impinging jets. *International Journal of Heat and Mass Transfer*, 104, 39-50.

CONFERENCE PAPERS

- Castrillo G., Greco C.S., Crispo C.M., Astarita T. & Cardone G., (2015); Impinging single and twin circular synthetic jets flow field. In *PIV15; 11th Int. Symp. on Particle Image Velocimetry*. 14-16 September, Santa Barbara (California, USA).
- Castrillo G., Discetti S. & Astarita T., (2015). Blob-enhanced tomographic PIV. In *PIV15; 11th Int. Symp. on Particle Image Velocimetry*. 14-16 September, Santa Barbara (California, USA).
- Astarita T., Castrillo G. & Cafiero G., (2015). On the effect of fractal geometric parameters on the heat transfer features of circular impinging jets. In *APS Division of Fluid Dynamics Meeting Abstracts*.
- Cardone G., Greco C.S., Castrillo G. & Astarita T., (2015). Experimental Analysis of Impinging Single and Twin Circular Synthetic Jets. In *APS Division of Fluid Dynamics Meeting Abstracts*.
- Castrillo G., Paolillo G., Contino M., Cafiero G. & Astarita T., (2016). Flow field features of fractal jets. In *18th International Symposium on the Application of Laser and Imaging Techniques to Fluid Mechanics*. 4-7 July, Lisbon, (Portugal)
- Castrillo G., Cafiero G. & Astarita T., (2016). Flow field characterization of a synthetic jet device equipped with a square fractal grid. *Workshop "Conceptually new, multi-scale solutions to industrial flow problems"*, 28-30 September, London (UK)

LIST OF PUBLICATIONS

- Castrillo G., Cafiero G., Greco C.S. & Astarita T., (2017). On the effects of a square fractal grid on a synthetic jet actuator flow field. In PIV17; *12th Int. Symp. on Particle Image Velocimetry*. 18-22 June, Busan (South Korea)
- Castrillo G., Cafiero G. & Astarita T., (2017). The effects of the secondary iterations' bars of square fractal grids. In PIV17; *12th Int. Symp. on Particle Image Velocimetry*. 18-22 June, Busan (South Korea)

ACKNOWLEDGEMENTS

So, that's it... it's time to sum up the last three years! One of the longest and amazing trips of my life is approaching its end. Who really knows me, behind my big toothy smile, also knows that sometimes it has been really hard for me.

If I am here, writing these few notes, it's because of my well-known perseverance and because of some of you who were always there, on my side, for helping me and pushing me beyond my limits and fears. So, I can't really move on without thanking you!

- IT'S GOING TO BE HEARTBREAKING: IF YOU ARE WEAK OF HEART I WOULD SUGGEST NOT TO GO ON READING! -

Thank you *Prof. Tommaso Astarita*. You have been a teacher, a model, a friend, a source of inspiration... I'm here, now, writing and I can't stop laughing while thinking back to all the nonsense conversations we had (don't worry, dear reader: we also had a lot of "full-of-sense" conversations!), streams of consciousness comparable to Joyce's ones! I will never thank you enough for having shared with me part of your wide knowledge and experience and for having guided me through these years, with enormous patience and dedication. It has been an honour to be your PhD student! As it has been an honour to be the first Ph.D. student supervised by *Dr. Gioacchino Cafiero*. Jack, you guided me through my first experiments, from the setup towards the data analysis. During these years, you have found a break in your busy life every time I needed your help; you have never refused a Skype-call even now that you are in the UK. Thank you, again and again! I must also thank *Prof. Stefano Discetti*: you have been a kind of "unofficial tutor". Thank you for your precious comments on my work and for your suggestions about life and future.

Thank you, *Prof. Carlo Salvatore Greco*: in these last years you spent so much time trying to help all of us in the Lab. Maybe you don't know but you have been for me a reference point, a person to which I could always explain my doubts and point of views about both research and Lab-life.

I am so much thankful to *Prof. Giovanni Maria Carlomagno*. If I became interested in fluid dynamics and I undertook this career, it's because of your lectures. Thanks a lot also for giving me the privilege to be seated at your desk while listening anecdotes about your amazing life. I feel like those will be the kind of stories I'll narrate to my sons as "Once my dear *Prof. Carlomagno* told me...".

ACKNOWLEDGEMENTS

I must thank *Prof. Gennaro Cardone* for his help and suggestions, above all for solving technical issues always present in our lab (probably in all labs!) when setting up the experiments.

Thank you, *Prof. Andy Woods* for hosting me and supervising me in Cambridge for seven months: it has been for me such a great opportunity of both personal and professional growth! Finally, thank you *Prof. J. Christos Vassilicos* and *Prof. Andrea Sciacchitano* for having carefully reviewed this thesis and for the suggestions and the nice comments about it.

Thank you to all the “Lab-mates”! *Cuono Massimo*, you have been my office mate; we started this journey together, supporting each other day by day! Thanks for the nice time we spent together and also for tolerating me when I was not so nice! *Mattia*, we met eight years ago, when we started our university studies. We both know ours it’s not just a working relationship: it’s a Friendship! I hope you will be the guy I’ll call for a chat still for a long long time! Thanks *Gerardo*, you were always ready to share your knowledge with me and help me in setting up the experiments (and also always ready to talk about other people ☺!). Thanks to *Simone* for the nice talks we had during these years, even outside the lab. Thank you to all the *old-guys* of this Lab: *Dr. Giuseppe Ceglia* (I’ll never forget our trip in Seoul as I think you’ll never forget how much I can be a pain in the neck when I am in my “traveller-version”), *Prof. Francesco Avallone* and *Prof. Andrea Ianiro*. Finally, thanks to *Giuseppe*, ‘cause there’s no Lab without *Peppe Sicardi!!!* Guys, I wish you all the best for your future!

Thank you, *Dr. Mario Ostieri*. I am sure your smartness and your determination will get you far! Thank you to the next doctor, *Francesco*, because no matter where you are or where I am -Turin, Naples, Rome, UK or US- you are always the one who checks if love, life and job are all right!

Thank you to my dear housemates: my darling *Kata*, *Alireza* and *Sam* (yes, you were a housemate as you probably spent more time at home than us!) thank you so much for having been for me a kind of family! And again, *Denise*, *Teresa*, *Fabiana*, *Pasquale* and *Raffaele* (aka *Lello*). I hope to have given you at least one-tenth of how much you have given me!

Thank you, *Floriana*, as even if we did not undertake this adventure together in Naples, I always found in you someone to lean on, as a sister!

I must thank my family, my darling cousins, brothers, aunts, uncles, my lovely grandma and, above all, *my mum* and *my dad*: I would have never reached this goal without your support.

Dino, THANK YOU FOR HAVING WAITED ME! During these long three years (or better, these long eight years) you never said a word every time I put my Ph.D. at

ACKNOWLEDGEMENTS

the first place because you knew how much it was important to me. But now, this is “our time”! So, good luck to us for our life together as, remember, wherever you are or wherever I am, it’s where WE are!

Giusy Castrillo